Removal of Uranium(VI) in Contaminated Water Using Iron Based Nanoparticles and Simultaneous Adsorption of Uranium(VI) and 2-Chlorophenol by Activated Carbon Fiber supported Titanate Nanotubes

by

Jun Duan

A dissertation submitted to the Graduate Faculty of
Auburn University
in partial fulfillment of the
requirements for the Degree of
Doctor of Philosophy

Auburn, Alabama
Dec 14, 2019

Keywords: Uranium, Iron sulfide, Zero valent iron, Titanate nanotubes, Reductive immobilization, Water treatment

Approved by

Dongye Zhao, Chair, Professor of Environmental Engineering
Mark O. Barnett, Professor of Environmental Engineering
Joel S. Hayworth, Associate Professor of Environmental Engineering
Audrey Gamble, Assistant Professor of Crop, Soil and Environmental Sciences

Abstract

Uranium is one of the most detected radionuclides in aquatic systems. Reductive immobilization and adsorption have been commonly practiced to remove uranium from water. In this study, CMC-stabilized iron sulfide (FeS) nanoparticles and FeS- modified zero-valent iron ($FeS@Fe^0$) nanoparticles were synthesized to remove U(VI) from water through concurrent reduction and adsorption. Both types of nanoparticles exhibited high reduction reactivity towards U(VI). A retarded first-order kinetic model was able to interpret the kinetic data. The materials were able to perform well under simulated groundwater chemistry conditions. Spectroscopic and extraction studies revealed that the main removal mechanism of U(VI) was due to concurrent reductive conversion of U(VI) into U(IV) and adsorption of uranyl cations onto the nanoparticles. The immobilized uranium remained stable over prolonged periods of time under simulated groundwater conditions.

Activated carbon fiber supported titanate nanotubes (TNTs@ACF) was prepared based on commercial activated carbon fiber and TiO_2. TNTs@ACF combines the merits of TNTs and ACF, and was able to simultaneously remove U(VI) cations and 2-chlorophenol (2-CP). TNTs@ACF exhibited synergistic adsorption towards U(VI) and 2-CP when both contaminants were co-present. The synergistic effect is attributed to concurrent surface complexation and π-cation interactions of U(VI) and 2-CP on the material surface.

CMC-FeS, $FeS@Fe^0$, and TNTs@ACF hold the potential to facilitate reductive removal of U(VI) and simultaneous removal of metals/radionuclides and organic pollutants in contaminated water and soil.

Acknowledgments

I would like to express my sincere appreciation to my advisor, Dr. Dongye Zhao, for his guidance and support for my academic improvement and parent-like care for my life and my family in Auburn. The working experience with Dr. Zhao in the past five years becomes one of my sweetest memories in my life.

I want to thank my committee members, Dr. Mark O. Barnett, Dr. Joel S. Hayworth, and Dr. Audrey Gamble and my dissertation outside reader Dr. Yi Wang for my Ph.D. study and valuable suggestions in finishing my dissertation. Their knowledgeable teaching and revising make my study a fruitful process. I would like to thank Jinling Zhuang for his daily management of the lab to enable the lab operating properly. I also want to thank Dr. Wen Liu, Dr. Xiao Zhao, Dr. Zhengqing Cai, Dr. Haodong Ji, and my fellow students in the Environmental Program for their supportive discussion and family-like friendship.

Lastly, I would like to sincerely appreciate my wife Jie Pu for her love, accompany and support for my life. She encourages me all the time when I feel upset and lack of confidence. I also want to thank my parents for their understanding and support.

War Eagle!

Table of Contents

List of Tables

List of Figures

Chapter 1. Background and Introduction

1.1. Uranium contamination in water and soil

Uranium, as a primary radionuclide, occurring both naturally and anthropogenically. The major sources of anthropogenic radionuclides are uranium mining and refining, nuclear energy power plants, nuclear weapon production and testing, radioactive wastes disposal, and nuclear accidents (Hu et al., 2010). A survey of 18 Department of Energy (DOE) facilities reported that uranium concentration in groundwater can reach up to $1.7*10^6$ (Riley and Zachara, 1992), while uranium concentration in soil varies from 0.3 to 11.7 mg/kg based on an effects of atomic radiation study conducted by United Nations Scientific Committee(UNSC) (UNSC, 1993). The maximum contamination level (MCL) for drinking water of uranium was regulated to be 30 µg/L by the United States Environmental Protection Agency (USEPA) in 2000 (Gallegos et al., 2013).

1.2. Reductive immobilization of U(VI)

Toxicity and mobility of uranium are closely associated with its valent state. Hexavalent uranium is mobile and more toxic in the environment, while tetravalent uranium is less toxic due to the sparing solubility and formation of precipitate, for example, uraninite (Bi et al., 2013). Thus, the redox conditions of subsurface environment has great impact on the uranium transport and fate and reductive immobilization of U(VI) to sparsely soluble U(IV) is widely considered as a promising and effective uranium remediation technology in groundwater (Liu et al., 2018; Shao et al., 2015; Veeramani et al., 2013). Zero valent iron (ZVI) nanoparticle is proven to be one of the most effective reductants for uranium clean-up due to its large specific surface area, strong reducing power, low cost and easy magnetic separation (Li et al., 2015; Zhao et al., 2016). However, ZVI tends to aggregate into larger-scale particles due to the inter-particle van der Waals forces and magnetic dipolar interactions (Zhao et al., 2016); in addition, ZVI is not thermodynamically stable in water and easily oxidized by water and dissolved oxygen (Henderson and Demond, 2013, Fan et al., 2016). The aggregation and rapid loss of ZVI lower its reactivity and selectivity for uranium reduction. Iron sulfide (FeS) is another effective nanoparticle for the uranium remediation through sorption and reduction in the past decade (Hua and Deng, 2008; Hyun et al., 2012; Shao et al., 2016).

Compare to ZVI, FeS does not necessarily undergo anoxic corrosion in water and can provide redox buffer capacity for reduced uranium (Carpenter and Hayes, 2015; Henderson and Demond, 2013). It has higher electronegativity (5.02 eV) (Xu and Schoonen, 2000) than that of Fe^0 (4.04 eV) (Pearson, 2008) and good electron conductivity resulting from low bandgap (E_g = 0.1 eV) (Du et al., 2016). FeS is also reported to have a lower pH of point of zero charge (pH_{PZC}) (as low as 2.9) (Widler and Seward, 2002) than that of Fe^0 (7.5) (Su et al., 2015), which can facilitate the metal cationic sorption through electrostatic attraction forces.

Recently, sulfidation of nZVI (S-nZVI), which inherits the merits of both Fe^0 and FeS, is reported to be a promising technique for Fe^0 improvement with higher reactivity, selectivity towards contaminants over water and less Fe^0 aggregation; meanwhile, S-nZVI possibly retains the magnetic property of Fe^0 and provide oxidation buffer capacity (Fan et al., 2014; Fan et al., 2017; Gong et al., 2017; Li et al., 2017). The synthesis methods of S-nZVI can be divided into two categories: one-step and two-step methods, while the main sulfur source is sulfide or dithionite (Li et al., 2017). In the common two-step method, before the second sulfidation step, synthesized Fe^0 was first collected after washed with water and then freeze-dried or vacuum-dried. This process would probably waste a considerable portion of reducing power of Fe^0, and is also not practical for field-scale application due to the complexity of the synthesis process. Moreover, the subsequent sulfidation process depends on the corrosion of Fe^0 by water to produce Fe^{2+} and then react with S^{2-} to form FeS precipitation, which is a slow process and also not practical. Therefore, it is imperative to establish a new class of synthesis method that can facile synthesize the core-shell structured S-nZVI particles without wasting the reducing power and the complexity of the method.

Nanoparticle aggregation limits its reactivity, mobility, and deliverability into the target contaminant zone (Fan et al., 2016; Zhao et al., 2016). The nanoparticle aggregation can be greatly improved with the application of stabilizer. For example, polysaccharides, such as starch and carboxymethyl cellulose (CMC) were found highly effective in stabilizing zero-valent iron (ZVI) and offer both greater reactivity and soil deliverability (He and Zhao 2007; He et al., 2007). However, the application of stabilized iron sulfide for U(VI) removal is yet to be studied.

1.3. Adsorption of U(VI) by titanate nanomaterials

Among the studied remediation technologies for uranium removal from water, adsorption is often preferred for its easy operation and lower cost, and adsorbents of rapid kinetics and high capacity have been consistently sought (Liu et al., 2016). Titanate nanotubes (TNTs) is intensively studied for heavy metal remediation due to the unique adsorption properties, such as high adsorption capacity, pH tolerance, easy separation, and regeneration. Liu et al. (2016a) studied the adsorption of U(VI) by TNTs and found the adsorption capacity can reach to 333 mg/g.

In some contamination sites, radionuclides coexist with other chemical pollutants. Riley and Zachara (1992) studied the chemical contaminations on DOE lands and found that chlorinated hydrocarbons are one of the most coexisted pollutants with radionuclides. Thus, technologies for simultaneous removal of radionuclides and chlorinated hydrocarbons are highly needed. Recently, Liu et al (2016b) modified the TNTs with activated charcoal (AC), which is composed of an activated charcoal core and a shell of carbon-coated titanate nanotubes, and showed excellent adsorption capacity and photo regeneration for phenanthrene (model petroleum hydrocarbons). Therefore, it is promising that activated carbon modified TNTs could achieve simultaneous removal of U(VI) and chlorinated hydrocarbons from wastewater.

1.4 Factors affecting uranium removal

Geochemical constituents, pH, dissolved oxygen (DO), complex substances, and iron content can control the mobility of uranium (Nolan and Weber, 2015).

1.4.1. pH

Solution pH is a simple but of great importance property that masters several aspects related to uranium immobilization and mobilization process. First, pH controls the speciation and solubility of uranium. **Fig. 1-1** depicts the uranium speciation as a function of pH. At different pH, U(VI) exists as different species and uranyl ions carry different charges when the pH increases from acid to basic, which would affect the affinity of U(VI) to particles surface (Liu et al., 2016). Meanwhile, pH also controls the solubility of uranium as depicted in **Fig. 1-2** (data obtained from MINTEQ 3.0). Uranium has relative higher solubility at acidic and basic pH, while the lowest solubility occurs around neutral pH.

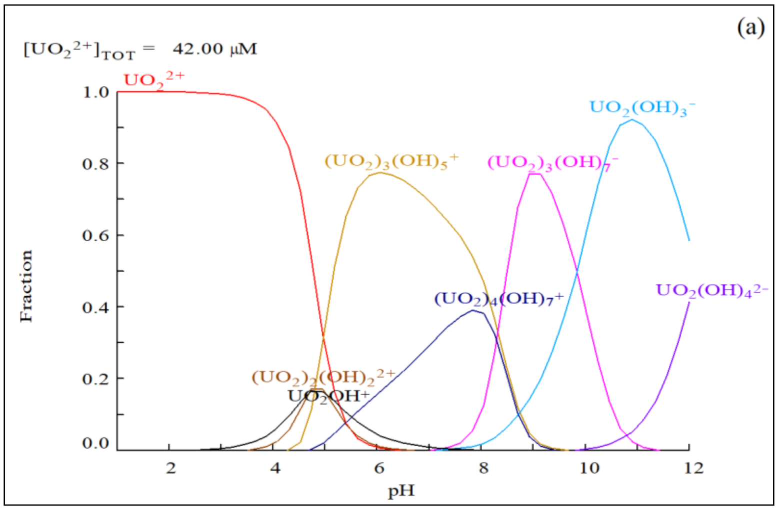

Fig 1-1. Distribution of U(VI) species as a function of pH in the absence of carbonate. (Initial U(VI) concentration = 10 mg/L, Temperature =25 °C).

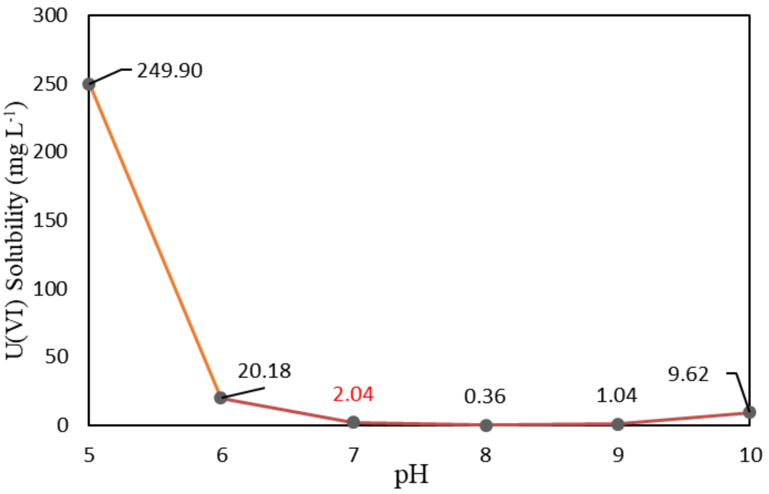

Fig 1-2. Solubility of U(VI) species as a function of pH.

Second, soil minerals and organic matter always carry a surface charge and the charge is also pH-dependent. The pH at which surface positive and negative charge canceled out is called the point of zero charge (pH_{pzc}). When pH below pH_{pzc}, minerals or SOM would be positively charged; when pH above $pH_{pzc,}$ the surface charge would become negative. The different surface charge will ultimately affect the interaction between uranium ion and soil, either attraction or repulsion (Mamindy-Pajany et al., 2009)

Third, redox reactions are always accomplished with H^+/OH^- production or consumption, and change pH will favor or inhibit the reaction. For example, **Eq.** (**1-1**) represents the U(VI) reduction to U(IV) and higher pH will favor the formation of sparsely soluble U(IV) and immobilize uranyl ions.

$$UO_2^{2+} + 2e^- + 4H^+ \leftrightarrow U^{4+} + 2H_2O \qquad (\mathbf{1\text{-}1})$$

Last, microbial activities, especially under anaerobic conditions, are an important pathway to naturally reduce U(VI) to U(IV). While the growth of microorganisms requires an appropriate pH range, an extreme pH will affect the uranium immobilization process via inhibiting the microbial activities. He et al. (2008) studied the effect of pH on the electricity generation from a microbial fuel cell (MFC) and found the MFC works best between pH 8 and 10, and lower or higher pH would inhibit the rate of the reaction. Thus, a proper pH needs to be maintained to maximize the biotic reduction/immobilization of uranium.

1.4.2. Redox reaction

As mentioned above, uranium mainly exists as IV and VI valent state, while U(VI) is more mobile and toxic and U(IV) readily precipitates as sparingly soluble minerals, such as UO_2. Therefore, the redox reactions that govern the valent state of uranium could directly affect the immobilization/mobilization process. Here, the redox reactions from biotic and abiotic sources are separately discussed.

1.4.2.1 Biotic

Under anaerobic conditions, U(VI) can be reduced by microorganisms, such as sulfate-reducing bacteria, to form $UO_2 \cdot xH_2O$ (Abdelouas et al., 2002). In another situation, bacterial will not directly reduce U(VI); instead, Fe(III) and $SO4^{2-}$ would be reduced first and finally form iron sulfide according to **Eqs.** (**1-2) – (1-4**). It is reported that U(VI) could be reductively immobilized by iron sulfide and the excess iron sulfide can serve as a redox buffer to control the uranium remobilization process (Abdelouas et al., 1999; Abdelouas et al., 2000; Zhao et al., 2013). However, the subsurface conditions keep changing and anaerobic conditions could not be kept all the time, so under oxic conditions biotic reduction is limited and reduced form uranium are exposed to reoxidation and remobilization.

$$Fe^{3+} + e^{-} \leftrightarrow Fe^{2+} \qquad (\mathbf{1\text{-}2})$$

$$SO_4^{2-} + 8e^{-} + 8\ H^{+} \leftrightarrow S^{2-} + 4H_2O \qquad (\mathbf{1\text{-}3})$$

$$Fe^{2+} + S^{2-} \leftrightarrow FeS \qquad (\mathbf{1\text{-}4})$$

1.4.2.1 Abiotic

In abiotic redox reactions, O_2 is one of the most important subsurface components that remarkably affects the uranium immobilization/remobilization. A study about the effect of dissolved oxygen (DO) on the long-term in situ oxidation of uraninite (UO_2) indicated that near-complete oxidation of uraninite occurred at DO > 0.6 mg/L, followed by the dissolution of uranium as uranium complexes. However, at low DO concentration, no measurable uranium was detected in the solution, which means the reduced uranium could be very stable if DO access is limited (Lezama et al., 2015).

Another abiotic factor in the subsurface is Mn redox cycling. As depicted in **Fig. 1-3**, Mn (II) is oxidized to MnO_2 by O_2, then product MnO_2 is capable of rapid oxidizing U(IV) to U(VI) (Plathe et al., 2013). Mn(III) is reported as an important redox-active intermediate in Mn biogeochemical cycling and can lead to faster U(IV) dissolution than the comparable concentration of DO (Wang et al., 2013).

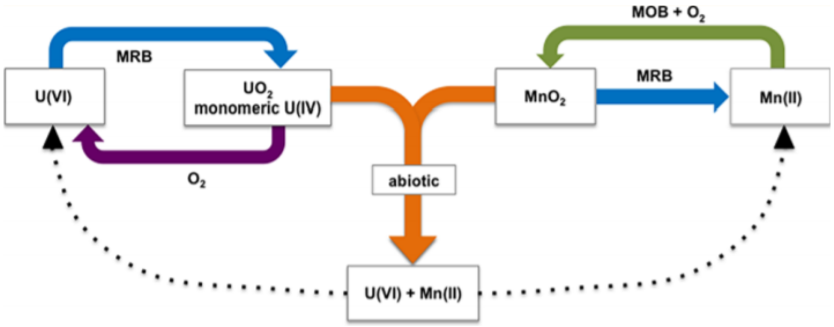

Fig. 1-3. U and Mn subsurface redox cycling (Plathe et al., 2013).

The above two factors are the naturally occurred process that controls the subsurface uranium fate. In recent decades, *in situ* remediations of uranium contamination by injecting zerovalent metal, especially zerovalent iron (ZVI) into contaminated soil becomes a new trend to control the uranium immobilization process (Liu et al., 2015). ZVI with high reduction potential could rapidly reduce U(VI) to U(IV), and provide a local reducing environment for an extended period of time (Xu and Zhao, 2007). Fan et al. (2014) stated that ZVI transformed by sulfide could even provide a longer protective effect towards oxidation, owing to the redox buffer capacity of iron sulfide formation.

1.4.3. Complex agents

Uranium can form complex with several complex agents, such as carbonates, natural organic matter, phosphate, and acetate. While in the complex agents, carbonates and organic matter play an important role in affecting the uranium immobilization/mobilization.

1.4.3.1. Carbonates

In presence of carbonates, U(VI) speciation is dominated by a series of strong anionic carbonate complexes at near-neutral and basic higher pH, which significantly enhance the mobilization of uranium by two means: 1) higher solubility of uranium-carbonates complexes; 2) negatively charged ion decrease the sorption between uranium ion and mineral surface, which is usually negatively charged (Krupka and Serne, 2002). **Fig. 1-4** illustrated the speciation of U(VI) as a function of pH in the presence of carbonate, and it could clearly tell that U(VI) carbonates complexes will be negative when pH > 6 (Liu et al., 2016). Zhou and Gu (2005) studied the effects of carbonate concentration on the oxidation of reduced form uranium from contaminated soil, and suggested that the presence of small quantities of carbonate/bicarbonate could result in a rapid and greatly increased leaching and the mobilization of U(VI) from the contaminated soil.

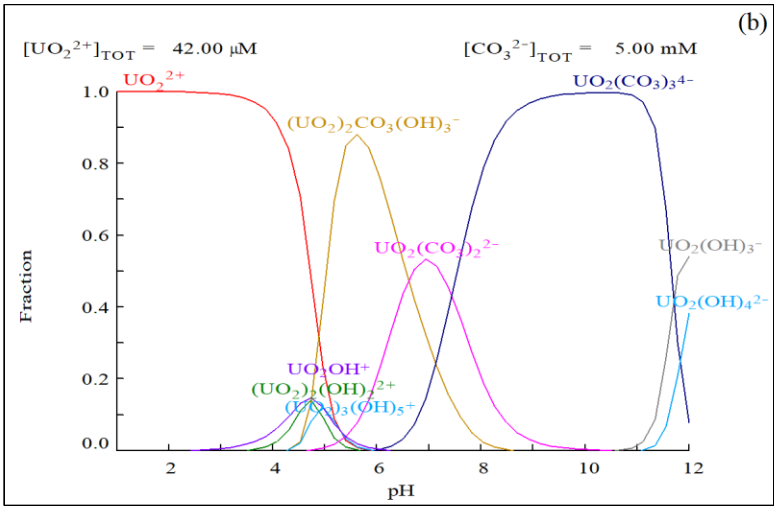

Fig. 1-4. Distribution of U(VI) species as a function of pH in the presence of 5 mM CO_3^{2-}. (Initial U(VI) concentration = 10 mg L^{-1}, Temperature =25 °C).

1.4.3.2. Natural organic matter

Uranium could also form relatively strong complexes with natural organic matter (NOM) in the subsurface. It was reported that even at low concentrations, soluble NOM can prevent U sorption and lead to increased mobility attributed to the formation of large complexes molecule (Cumberland et al., 2016). Long-term studies proved that natural organic matter could potentially influence the long-term stability of reduced U(IV) by slowly dissolving U-bearing minerals even under strongly reducing environment (Luo and Gu 2008; Luo and Gu, 2011).

1.5. Objectives

The key objectives were to 1) prepare iron-based nanoparticles (CMC-FeS, FeS@Fe^0) for reductively immobilizing U(VI) from water; 2) synthesize a new type of activated carbon fiber supported titanate nanotubes and test its application for the simultaneous adsorption of U(VI) and 2-CP from water; 3) elucidate the underlining mechanism of U(VI) removal by various nanomaterials. The specific objectives were to:

- Determine the optimal CMC-to-FeS molar ratio that facilitates both nanoparticle stability and U(VI) removal efficiency;
- Investigate the optimal synthesis conditions for FeS@Fe^0 particles so as to achieve better reactivity and reoxidation resistance;
- Develop a new class of activated carbon fibers supported titanate nanotubes (TNTs@ACFs) and the application for simultaneous removal of U(VI) and 2-CP;
- Examine the effects of water chemistry on the U(VI) removal by CMC-FeS and FeS@Fe^0;

- Explore the underlying mechanisms of U(VI) reductively immobilization by CMC-FeS and FeS@Fe^0, and synergistic effect of U(VI) and 2-CP co-adsorption.

1.6 Organizations

The dissertation includes five chapters, each chapter is formatted as a standalone paper in the style of *Water Research* except for Chapter 1 (Background and Introduction) and Chapter 5 (Conclusions and Suggestions for Future Research). **Chapter 1** introduces the background uranium contamination in water and soil, the prevailing technologies for uranium removal and the critical environmental factors affecting transport and fate of uranium. **Chapter 2** studies the factors affecting the reductive immobilization of U(VI) by CMC stabilized FeS and discusses the mechanism of U(VI) removal by CMC-FeS and long-term stability of U(VI) of immobilized U(VI) by CMC-FeS nanoparticles under oxic and anoxic conditions. **Chapter 3** prepares and optimizes a new-type of FeS coated Fe^0 in one-pot and tests its performance for U(VI) removal under various water chemistry conditions, and investigates the mechanism of enhanced U(VI) removal by FeS@Fe^0 than FeS and Fe^0. **Chapter 4** synthesizes a new class of activated carbon fiber supported titanate nanotubes for the simultaneous removal of U(VI) and 2-CP in complex wastewater, and explores the mechanism for synergistic enhancement of U(VI) and 2-CP adsorption in the binary system. **Chapter 5** summarizes the major conclusions of all researches and suggests the potential area for future works.

Chapter 2. Immobilization of U(VI) by Stabilized Iron Sulfide Nanoparticles: Water Chemistry Effects, Mechanisms, and Long-Term Stability

2.1. Introduction

Uranium (U) is one of the most detected radionuclides in groundwater and soil due to its widespread uses in nuclear weapon manufacturing and testing and nuclear energy production, and uranium mining and processing (Bi et al., 2013; Ma et al., 2018). Because of the serious public health risk associated with U exposure, EPA revised the radionuclides rule in 2000 and set the maximum contaminant level (MCL) to 30 µg/L in drinking water (Gallegos et al., 2013).

The mobility of uranium is highly related to the oxidation states. Under oxidizing conditions, hexavalent uranium in the form of UO_2^{2+} is the most predominant species, which is soluble and mobile in soil and groundwater, while under reducing conditions, tetravalent uranium, such as uraninite (UO_2) (log $K_{sp\ =}$ -54.6), is the favorable species, which is sparingly soluble and immobile (Bi and Hayes, 2014; Spycher et al., 2011). Thus, the reductive conversion of mobile U(VI) to immobile U(IV) has been considered one of the most promising approaches for curing uranium exposure (Duan et al., 2019; Shao et al., 2015).

In uranium-contaminated aquifers, iron sulfides are known to play an important role in reductive immobilization of U(VI) (Spycher et al., 2011; Veeramani et al., 2013). Sulfate-reducing bacteria (SRB) can use sulfate as the electron acceptor and produce sulfide, which reacts with Fe(II) and/or Fe(III) to form iron sulfides (Bi and Hayes, 2014). Mackinawite (FeS) is typically the first ferrous sulfide solid formed under sulfate-reducing conditions, which is the precursor of other iron sulfide minerals, such as greigite (Fe_3S_4) and pyrite (Hyun et al., 2012). Besides natural mackinawite mineral, synthetic mackinawite was also reported to be able to reduce U(VI) into uraninite, a desirable end-point that is more stable and resistant to oxidation compared to non-uraninite species (Bi et al., 2013; Carpenter et al., 2015; Gallegos et al., 2013; Hyun et al., 2012).

Compared to bulk FeS, nanoscale FeS particles provide a larger specific surface area and potentially greater reactivity and soil deliverability. Researchers have demonstrated that synthetic FeS nanoparticles are effective in treating various contaminants in soil and groundwater, including heavy metals, oxyanions, radionuclides, chlorinated organic compounds, nitroaromatic compounds, and polychlorinated biphenyls (Gong et al., 2016).

To facilitate soil delivery and enhance reactivity, stabilized FeS nanoparticles have been developed and tested. Among stabilizers tested, carboxymethyl cellulose (CMC) has shown to be most effective in preparing highly dispersible and transportable FeS nanoparticles (mean size = 34.3 nm) for soil remediation (Gong et al., 2014). Moreover, CMC stabilized FeS (CMC-FeS) nanoparticles have been found effective for the removal of U(VI) in water (Shao et al., 2016). However, effects various water chemistry parameters, such as pH, coexisting ions and natural organic matter (NOM), on the removal efficacy have not been examined, and the underlying reaction mechanisms remain unclear. Moreover, the long-term stability of immobilized U under oxic or anoxic conditions has not been investigated.

Solution pH is a key parameter that not only affects the reactivity of CMC-FeS but also governs the speciation and solubility of U(VI) (Descostes et al., 2010; Hua and Deng, 2008). In groundwater, various coexisting cations may also impede the reaction by competing for the reactive sites. Uranium can form stable complexes with bicarbonate and natural organic matter (NOM), which can alter the particle stability and reactivity towards U(VI) (Crane et al., 2015; Liu et al., 2016). While UO_2 is the desired product, it is thermodynamically unstable in the presence of oxygen and may be re-oxidized and re-solubilized (Bi et al., 2013; Bi and Hayes, 2014). Therefore, there is a need to investigate the long-term stability or re-oxidization rate of U(IV) under oxic and anoxic conditions.

The overall goal of this study was to investigate the effectiveness of CMC-FeS for U(VI) removal under various water chemistry conditions and to determine the re-oxidation potential of reduced U. The specific objectives were to: (1) determine the optimal CMC-to-FeS molar ratio that facilitates both nanoparticle stability and U(VI) removal efficiency; (2) explore the effects of solution pH, coexisting cations (Na^+ and Ca^{2+}), bicarbonate, humic acid and the combination thereof on U(VI) removal by CMC-FeS; (3) elucidate the underlying U(VI) removal mechanisms under various conditions by means of FTIR, XRD, and XPS analyses; and (4) examine the long-term stability of immobilized U(VI) by CMC-FeS nanoparticles under oxic and anoxic conditions.

2.2. Materials and methods

2.2.1. Materials

All chemicals were of analytical grade or higher. The chemicals included ferrous sulfate heptahydrate ($FeSO_4$•$7H_2O$) and sodium sulfide nonahydrate (Na_2S•$9H_2O$) from Alfa Aesar (MA, USA); CMC in sodium form, sodium hydroxide (NaOH), uranyl acetate dihydrate ($UO_2(CH_3COO)_2\cdot 2H_2O$ with ^{238}U) from International Bio-Analytical Industrial Inc. (FL, USA); hydrochloric acid (HCl) and sodium bicarbonate ($NaHCO_3$) from Fisher

Scientific (NJ, USA); calcium chloride dihydrate ($CaCl_2$•$2H_2O$) and humic acid (HA, Leonardite Humic Acid Standard, 64% of total organic carbon (TOC) from Sigma Aldrich (MO, USA); Tris (hydroxymethyl) aminomethane (Tris buffer) from Acros Organics (NJ, USA); and 2-Morpholinoethanesulfonic acid (MES buffer) from TCI America (OR, USA).

2.2.2. Preparation of CMC-FeS nanoparticles

CMC-FeS nanoparticles were prepared following the method by Gong et al. (2014). Briefly, 5 mL of a 1% (w/w) CMC stock solution was added into 75 mL Millipore DI water (18.2 MΩ cm) in a 150-mL flask, and purged with high purity N_2 for 30 min to remove dissolved oxygen (DO). Then, solutions of 0.057M $FeSO_4$ (40 mL) and 0.057M Na_2S (40 mL) were prepared with N_2 pre-purged DI water. Under N_2 purging, the $FeSO_4$ solution (10 mL) was added into the CMC solution and purged for another 10 min to assure the complete formation of CMC-Fe^{2+} complex. Then, the Na_2S solution (10 mL) was introduced into the mixture solution dropwise under continuous shaking at 170 rpm and vacuum in 10 min. The resulting 100 mL suspension contained 500 mg/L of FeS and 0.05 wt.% CMC (i.e. CMC-to-FeS molar ratio of 0.0010). For comparison, bare FeS particles were also prepared following the same procedure but without CMC. The suspensions were sealed and aged for 24 h before use.

2.2.3. Characterizations

The hydrodynamic diameter and zeta potential (ζ) of CMC-FeS were measured by the use of a Malvern Zetasizer Nano ZS (Malvern Instrument, Worcestershire, UK). The crystal phase of the nanoparticle samples was acquired using a Dmax/2400 X-ray diffractometer (XRD, Rigaku, Japan) using the Cu Kα radiation (λ = 1.5418 Å) and at a scanning rate (2θ) of 4°/min. The XRD patterns were processed using the MDI Jade 5.0 with the ICDD database (Materials Data Inc., Livermore, CA, USA). Fourier transform infrared (FTIR) spectroscopy analysis was conducted on a Tensor 27 FTIR spectrometer (Bruker, Germany) through the KBr pellet method to obtain the functional groups binding information. Element compositions and oxidation states were analyzed on an AXIS-Ultra X-ray photoelectron spectroscopy (XPS, Kratos, England) using the Al $K\alpha$ X-ray at 15 kV and 15 mA. The C 1s peak (binding energy, $E_b = 284.80$ eV) was used to eliminate the static charge effects, and the results were analyzed using the software package Casa-XPS 2.3. The solid samples were obtained by filtering a particle suspension through a 50 nm cellulose acetate membrane under N_2 protection and dried under gentle nitrogen blowing, and then stored in a nitrogen-filled glovebox before the characterizations. For U-laden samples, the nanoparticles were first reacted with U(VI) for 24 h following the procedure as described in Section 2.4 before the filtration.

2.2.4. Effect of CMC concentration on U(VI) removal by CMC-FeS

To test the effect of CMC concentration on U(VI) removal, CMC-FeS suspensions were prepared at various CMC-to-FeS molar ratio (0.0006, 0.0010, 0.0016, and 0.0025) with a fixed FeS concentration of 500 mg/L following the method in Section 2.2. Then, 100 mL of a CMC-FeS suspension was mixed with 400 mL of a deoxygenated U(VI) solution (U(VI) = 12.5 mg/L) in a 500 mL polycarbonate bottle under anoxic conditions. The resultant solution contains 100 mg/L of CMC-FeS and 10 mg/L of U(VI), and the pH was kept at 7.0 ± 0.2 using the Tris buffer (10 mM). The bottles were tightly sealed and placed on a shaker operated at 170 rpm. After 24 h of equilibration, 10 mL of the suspension was sampled, filtered *via* the 50 nm cellulose acetate membrane under N_2

protection, and then the filtrate was analyzed to determine the U(VI) concentration in the solution.

2.2.5. Batch experiments

Batch experiments were carried out to test the effect of water chemistry conditions on U(VI) removal by CMC-FeS, including solution pH, coexisting ions (Na^+, Ca^{2+}, and HCO_3^-), HA, and synthetic groundwater. Typically, 100 mL of the CMC-FeS suspension (500 mg/L as FeS, CMC-to-FeS ratio of 0.0010) was added into 400 mL of a deoxygenated U(VI) solution (U(VI) = 12.5 mg/L) in 500 mL polycarbonate bottles under anoxic conditions and various water chemistry conditions. The pH was controlled at 7.0 ± 0.2 the Tris buffer (10 mM). Then, the mixture was transferred into 50 mL polycarbonate vials with zero headspace and placed on an end-to-end rotator at 40 rpm at room temperature (22 ± 1°C). At predetermined times, duplicate vials were sacrificially sampled in the same manner described in Section 2.4.

To test the pH effect, the batch kinetic tests were carried out in the pH range from 6.0 to 9.0, where the MES buffer (10 mM) and Tris buffer (10 mM) were used to keep pH at the desired values. To test the effects of coexisting ions, the tests were conducted in the presence of 1 mM of Na^+ or Ca^{2+}or a range of HCO_3^- (1 to 5 mM), with pH kept at 7.0 using the Tris buffer (10 mM). Similarly, the effect of HA was tested with the HA concentration varied from 1 to 10 mg/L as TOC. To examine the combined effects, the U(VI) tests were further tested using synthetic groundwater (SGW). The SGW was prepared following a modified recipe from a previous study (Yan et al., 2010), with the following components: HA = 3 mg/L as TOC, $Ca(NO_3)_2$ = 0.286 mM, $CaCl_2$ = 0.312 mM,

$MgSO_4$ = 0.529 mM, Na_2SO_4 = 0.451 mM, Na_2CO_3 = 0.0111 mM, $NaHCO_3$ = 0.604 mM, $KHCO_3$ = 0.43 mM, and pH = 7.0 ±0.2 .

Extractable U(VI) on the nanoparticles was determined per an anoxic bicarbonate/carbonate (CARB) extraction method (Hyun et al., 2012; Duan et al., 2019). Briefly, 25 mL of a suspension after the reaction was transferred to a 50 mL polycarbonate bottle pre-loaded with 25 mL of a CARB solution consisting of sodium carbonate (28.8 mM) and sodium bicarbonate (5.6 mM) under N_2 purging. The mixture was vortexed for 1 min and then allowed to react for 1h on an end-over-end rotator. Upon filtration through a 50 nm cellulose acetate membrane, U(VI) in the filtrate was measured. Then, U(VI) extracted from the particles was calculated by the difference in soluble U(VI) before and after the extraction. Consequently, U(IV), which is not CARB-extractable, was quantified per mass balance calculations.

2.2.6. Remobilization test: effects of anoxic and oxic conditions

Remobilization tests were carried out under anoxic and oxic conditions to investigate the long-term stability of reductively immobilized uranium. Immobilized U was prepared following the same procedure described in Section 2.4 under the following conditions: FeS = 500 mg/L, CMC = 0.05%, and pH = 7.0 ± 0.2. Following the reaction equilibrium, the suspensions of immobilized U were transferred in 50 mL polycarbonate vials and aged for 180 days under oxic (open to air) or anoxic (sealed in a N_2-filled glove box) conditions. After predetermined time intervals, duplicate vials were sacrificially sampled and analyzed for soluble U in the aqueous phase.

2.2.7. Analytical methods

Aqueous uranium and iron concentrations were analyzed on a 710-ES inductively coupled plasma-optical emission spectroscopy (ICP-OES, Varian, CA, USA). The detection limits of uranium and iron were 0.07 mg/L and 0.05 mg/L, respectively. TOC was determined using a Tekmar Dohrmann Pheonix 8000 UV-Persulfate TOC analyzer (Mason, OH, USA) with a detection limit of 0.1 mg/L.

2.3. Results and discussion

2.3.1. Effect of CMC-to-FeS molar ratio

Previous work indicated that fully stabilize FeS nanoparticles can be obtained at a CMC-to-FeS molar ratio of 0.0006 (Gong et al., 2014), and the stabilized nanoparticles hold the potential to be directly delivered in the soil to facilitate *in situ* soil remediation of target contaminants (Gong et al., 2012). Depending on the physico-chemical properties of the contaminants, the CMC coatings on FeS may alter (enhance or inhibit) the reactivity of FeS particles. Therefore, it is necessary to investigate the effects of CMC on U(VI) removal by the fully stabilized FeS nanoparticles, namely, CMC-FeS prepared at or above the minimum stabilizing CMC-to-FeS molar ratio of 0.0006. **Fig. 2-1** shows the equilibrium removal of U(VI) by FeS particles prepared at various CMC concentrations. In the absence of the stabilizer, 99.2% of initial U(VI) was removed. The removal remained about the same for bare FeS and CMC-FeS prepared at the CMC-to-FeS molar ratios of 0.0006 and 0.0010. Further increasing the ratio to 0.0016 and 0.0025 decreased the removal to 92.6% and 75.0%, respectively.

Modifying FeS particles with CMC could have several competing effects on the reactivity towards U(VI). First, CMC could inhibit the agglomeration of FeS nanoparticles *via* electrostatic repulsion and steric hindrance (He and Zhao, 2007). The hydrodynamic diameter of CMC-FeS was decreased from 1632 nm for bare FeS particles to 253, 223, and 166 nm, respectively, for CMC-FeS prepared at CMC-to-FeS ratios of 0.0006, 0.0010, and 0.0025 (Gong et al., 2014). The smaller particle size results in larger surface area and more reaction sites, and thus enhanced adsorption capacity and reductive reactivity (He and Zhao, 2008). Second, the CMC coating can provide additional adsorption capacity by coordination between U(VI) and the carboxyl groups of CMC and form $UO_2(CMC\text{-}COO^-)_2$ complex (Popescu et al., 2013), which, however, is subject to competition from the same complexation effect by the soluble CMC in the solution phase. Third, the CMC coating renders a more negative surface potential, which favors adsorption of the uranyl oxycations. Fourth, from a kinetic viewpoint, the CMC coating can partially passivate the particles by forming a semi-permeable barrier on the particle surface, which can inhibit the mass transfer of U(VI) or render some sites inaccessible (He and Zhao, 2007; Tratnyek et al., 2011). The overall effects would depend on the competition of the promotive and inhibitive effects and the specific operating conditions. In this work, the effects of CMC leveled off at when the CMC-to-FeS molar ratio was ≤ 0.0010, but CMC became increasingly inhibitive when the ratio was ≥ 0.0016, which is attributed to the increased blockage of the surface reactive sites due to elevated density of CMC on the surface.

After 6 months of aging, the hydrodynamic diameter of the nanoparticles grew to 1779, 359, 246, and 234 nm, respectively, for particles prepared at CMC-to-FeS molar ratios of 0, 0.0006, 0.0010, and 0.0025. The results indicate that FeS nanoparticles prepared at

CMC-to-FeS molar ratios of 0.0010 or higher could remain stable over prolonged periods of time. Taken together the capability for U(VI), long-term physical stability and soil deliverability, and CMC need, the optimal CMC-to-FeS molar ratio was determined to be 0.0010, and thus, the corresponding CMC-FeS was further tested in detail.

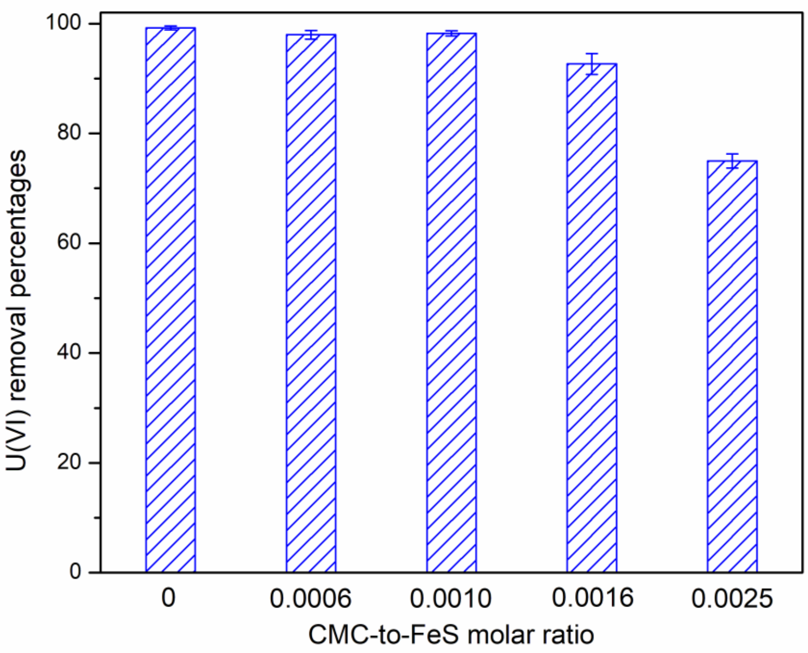

Fig. 2-1. Equilibrium U(VI) removal percentiles by FeS nanoparticles prepared at various CMC-to-FeS molar ratios. Experimental conditions: initial U(VI) = 10 mg/L, FeS = 100 mg/L, Tris buffer = 10 mM, pH = 7.0 ± 0.2, reaction time = 24 h, and temperature = 22 ± 1°C.

2.3.2. U(VI) removal kinetics and the effect of pH

Fig. 2-2 presents the U(VI) removal rates at four constant pH levels (6.0, 7.0, 8.0, and 9.0). In all cases, U(VI) was rapidly removed from the aqueous phase, with over 90% of removal within the first one hour except for pH 6.0 where 87% removal was achieved.

After 24 h reaction, the total U(VI) removal efficiency was ~98% at pH 7-9, and 95.1% at pH 6.0. The conventional pseudo-first-order model was first tested to fit the kinetic data, but the model failed to catch the data after the initial 5 min, which is likely due to the decreasing reaction rates as reactions proceed (Lin et al., 2009). Consequently, a retarded first-order model with a "sliding" factor α incorporated in the reaction rate constant was employed to accommodate the gradual deviation of the retarded reaction rates (Lin et al., 2009):

$$-\frac{dC_t}{dt} = \frac{k_{\text{init}}}{1+\alpha t} C_t \text{ or } C_t = C_0(1+\alpha t)^{-k_{\text{init}}/\alpha} \qquad \textbf{(2-1)}$$

where C_0 and C_t are U(VI) concentrations (mg/L) at time 0 (initial) and time t (min), respectively, and k_{init} is the initial rate constant (min^{-1}), which is analogous to a pseudo-first-order rate constant. **Fig. 2-2** shows that the model was able to adequately fit the entire kinetic data in all cases with the correlation coefficient (R^2) being > 0.97 (**Table 2-1**). According to **Eq.** (**2-1**), the initial half-life $t_{1/2,\text{ init}}$ can be calculated as:

$$t_{1/2,init} = \frac{2^{\alpha/k_{\text{init}}-1}}{\alpha} \qquad \textbf{(2-2)}$$

Table 2-1 gives the best-fitted values of k_{init} and α, and the corresponding $t_{1/2,\text{ init}}$. The fastest U(VI) removal was observed at pH 7.0, with a peak k_{init} value of 29.89 h^{-1} and a $t_{1/2,\text{ init}}$ of 0.035 h. Lowering the solution pH to 6.0 decreased k_{init} to 15.55 h^{-1}. Conversely, increasing the pH to 8.0 and 9.0 decreased k_{init} to 16.66 and 14.71 h^{-1}, respectively.

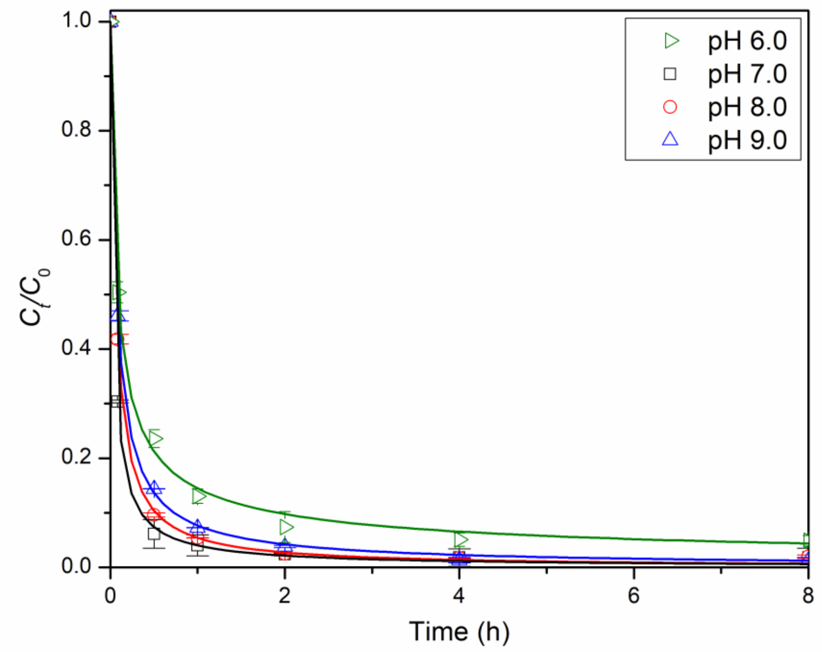

Fig. 2-2. Effect of pH on removal kinetics of U(VI) by CMC-FeS. Experimental conditions: initial U(VI) = 10 mg/L, FeS = 100 mg/L, CMC-to-FeS molar ratio = 0.0010, MeS buffer = 10 mM, Tris buffer = 10 mM, and temperature = 22 ± 1°C. Symbols: experimental data; Lines: retarded first-order model fittings.

Solution pH can affect the stability, surface potential and reactivity of CMC-FeS and affect the speciation of U(VI) (Duan et al., 2019; Lyu et al., 2017). First, the lower reaction rate at pH 6.0 could be owing to partial dissolution of the nanoparticles, and thus partial loss of the reaction sites (Gong et al., 2014). **Fig. 2-3** shows that the particle dissolution was negligible at pH ⩾ 7.0, while 24.1% of Fe was dissolved at pH 6.0. Despite the lower total U(VI) removal efficiency at pH 6.0 (95.1%), a similar U(VI) reduction percentage was reached (87.2%) when compared to pH 7 (**Fig. 2-4**). Second, at the alkaline pH, the dominant U(VI) species shifted from positively charged $(UO_2)_3(OH)_5^+$ and $(UO_2)_4(OH)_7^+$

to negatively charged $(UO_2)_3(OH)_7^-$, $UO_2(OH)_3^-$, and $UO_2(OH)_4^{2-}$ (**Fig. 2-5a**). Meanwhile, increasing the solution pH from 6.0 to 9.0 turned the zeta potential of CMC-FeS more negative from -27.5 to -38.9 mV (**Fig. 2-6**). Thus, adsorption or reduction of U(VI) by CMC-FeS became increasingly unfavorable due to escalated electrostatic repulsion between anionic U(VI) species and an increasingly more negative nanoparticle surface. Third, at alkaline pH, more iron (hydr)oxides can form, which precipitate on the surface of CMC-FeS, blocking the adsorption/reaction sites and hindering the electron transfer process (Li et al., 2017). After 24 h reaction, the total U(VI) removal remained at ~98% at pH 6.0-9.0, however, the portion of U(VI) removed through reductive conversion of U(VI) into U(IV) was decreased from 86.6% at pH 7 to 80.2% for pH 8.0 and 63.3% for pH 9.0, suggesting increasing site blockage with increasing pH. The findings are consistent with those reported when amorphous iron sulfide and hydrogen sulfide were used for U(VI) removal (Hua et al., 2006; Hua and Deng, 2008).

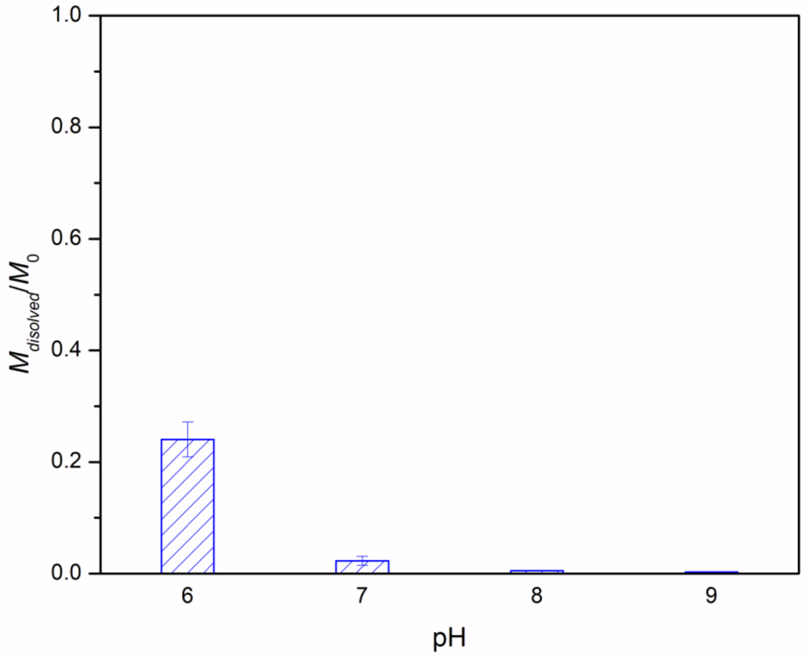

Fig. 2-3. Dissolution of CMC-FeS measured as soluble Fe as a function of pH. Experimental conditions: FeS dosage = 100 mg/L as FeS, MES buffer = 10 mM, Tris buffer = 10 mM, and temperature = 22 ± 1 °C. $M_{disolved}$ is the mass of Fe in the aqueous phase, and M_0 is the total mass of Fe.

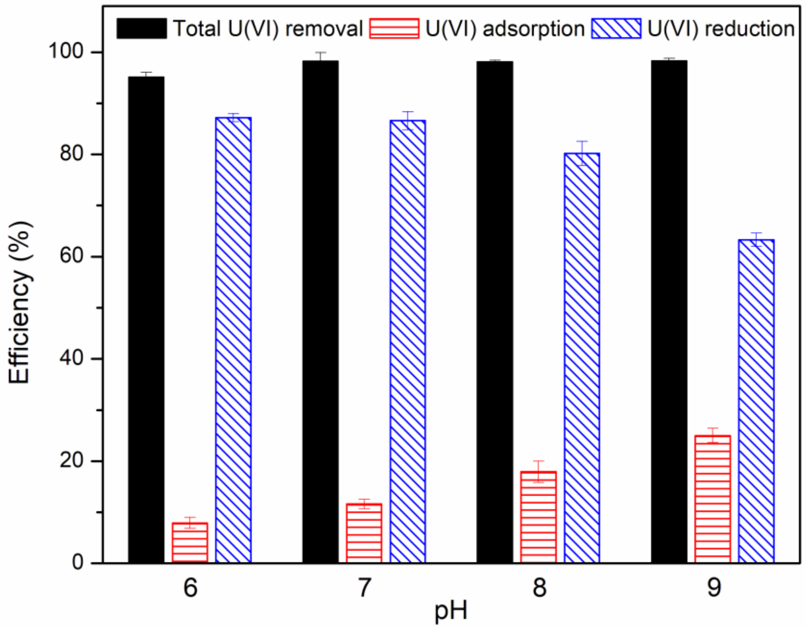

Fig. 2-4. Effect of pH on equilibrium U(VI) adsorption and reduction by CMC-FeS. Experimental conditions: initial U(VI) = 10 mg/L, FeS = 100 mg/L, CMC-to-FeS molar ratio = 0.0010, MeS buffer = 10 mM, Tris buffer = 10 mM, reaction time = 24 h, and temperature = 22 ± 1°C.

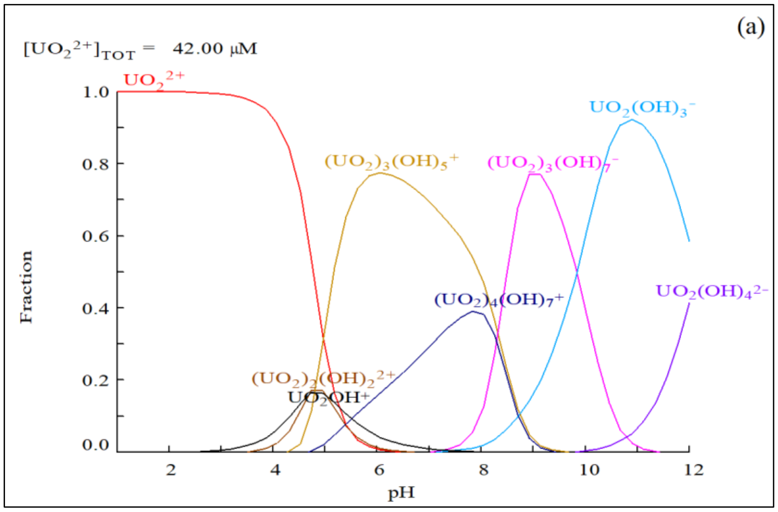

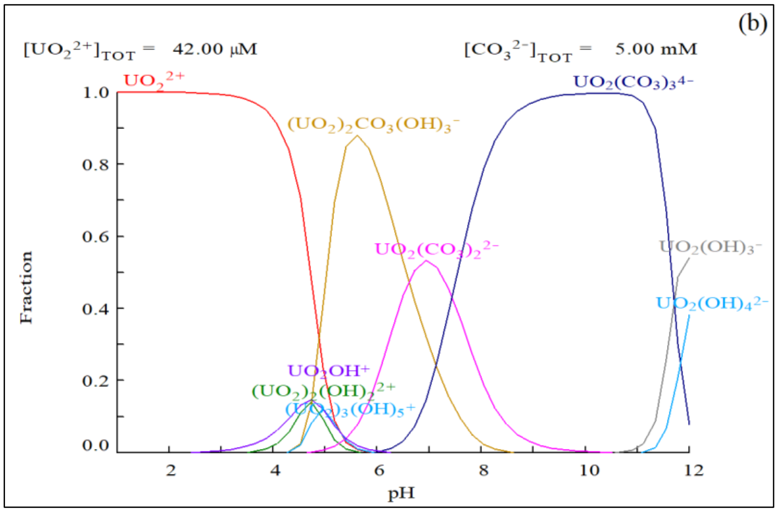

Fig. 2-5. U(VI) speciation as a function of solution pH calculated using the software MEDUSA: **(a)** in the absence of carbonate, and **(b)** in the presence of 5 mM CO_3^{2-}. Initial U(VI) = 10 mg/L (42 µM), Temperature = 25 °C.

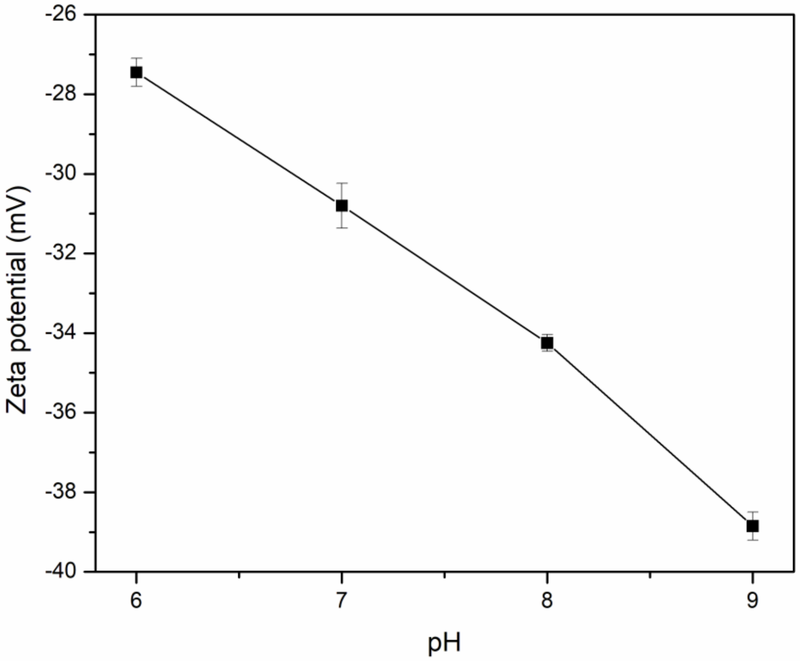

Fig. 2-6. Zeta potential of CMC-FeS as a function of solution pH.

Table 2-1. Best-fitted parameters of the retarded first-order model and estimated initial half-life under various experimental conditions.

Experimental conditions	**Retarded first-order model**			**$t_{1/2,\ \mathrm{init}}$ (h)**
	k_{init} (h^{-1})	**α (h^{-1})**	**R^2**	
pH 6.0	15.55	26.72	0.99	0.086
pH 7.0	29.89	32.72	0.99	0.035
pH 8.0	16.66	16.26	0.99	0.059
pH 9.0	14.71	16.37	1.00	0.071
pH 7.0, 1 mM Na^+	26.19	35.81	0.99	0.044
pH 7.0, 1 mM Ca^{2+}	18.51	46.71	0.99	0.10
pH 7.0, 1 mM HCO_3^-	3.14	4.45	0.99	0.38
pH 7.0, 5 mM HCO_3^-	0.17	0.12	0.97	5.18
pH 7.0, 1 mg/L HA as TOC	55.78	65.36	1.00	0.019
pH 7.0, 5 mg/L HA as TOC	23.13	59.20	0.99	0.083
pH 7.0, 10 mg/L HA as TOC	8.32	24.66	0.99	0.28
pH 7.0, Synthetic groundwater[a]	0.35	0.058	0.99	2.10

[a] Synthetic groundwater recipe: 0.286 mM $Ca(NO_3)_2$, 0.312 mM $CaCl_2$, 0.529 mM $MgSO_4$, 0.451 mM Na_2SO_4, 0.0111 mM Na_2CO_3, 0.604 mM $NaHCO_3$, 0.43 mM $KHCO_3$ and 3 mg/L HA as TOC.

2.3.3. Effect of Na^+ and Ca^{2+}

Fig. 2-7a shows the effects of coexisting Na^+ and Ca^{2+} on U(VI) removal by CMC-FeS. The presence of 1 mM Na^+ only slightly degreased the k_{init} value from 29.89 h^{-1} to 26.19 h^{-1}, while the addition of 1 mM Ca^{2+} lowered the k_{init} by a factor of 1.62 (to 18.51 h^{-1}), and diminished the U removal efficiency from 98.2% to 89.8%. The presence of cations in the solution can partially suppress the negative surface potential, thereby reducing the electrostatic repulsion and weakening the stability of the nanoparticles. In this case, the surface potential of the CMC-FeS nanoparticles was suppressed from -30.8 mV without the addition of Na^+ or Ca^{2+} to -25.8 and -17.4 mV with the addition of 1 mM Na^+ or 1 mM

Ca^{2+}; and accordingly, the hydrodynamic diameter of the nanoparticles increased from 253 to 331 and 642 nm, respectively. The partial aggregation of the nanoparticles resulted in lowered site accessibility and reactivity for U(VI) removal. In addition, cations, especially multivalent cations, can compete with the uranyl oxycations for the adsorption sites through competitive electrostatic ion pairing (Duan et al., 2019). Moreover, in the presence of carbonate ions, Ca^{2+} is known to complex with UO^{2+} to form negatively charged or electro-neutral uranyl carbonate complexes through **Eqs.** (**2-3**) and (**2-4**) (Liu et al., 2016), which are hardly adsorbable to the negative nanoparticle surface.

$$UO_2^{2+} + Ca^{2+} + 3CO_3^{2-} = CaUO_2(CO_3)_3^{2-} \quad \textbf{(2-3)}$$

$$UO_2^{2+} + 2Ca^{2+} + 3CO_3^{2-} = CaUO_2(CO_3)_3\ (aq) \quad \textbf{(2-4)}$$

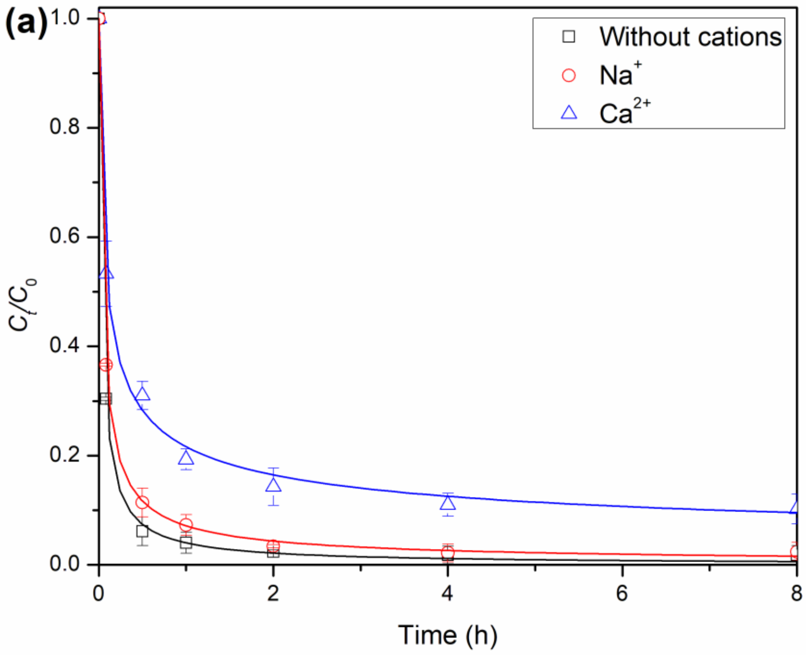

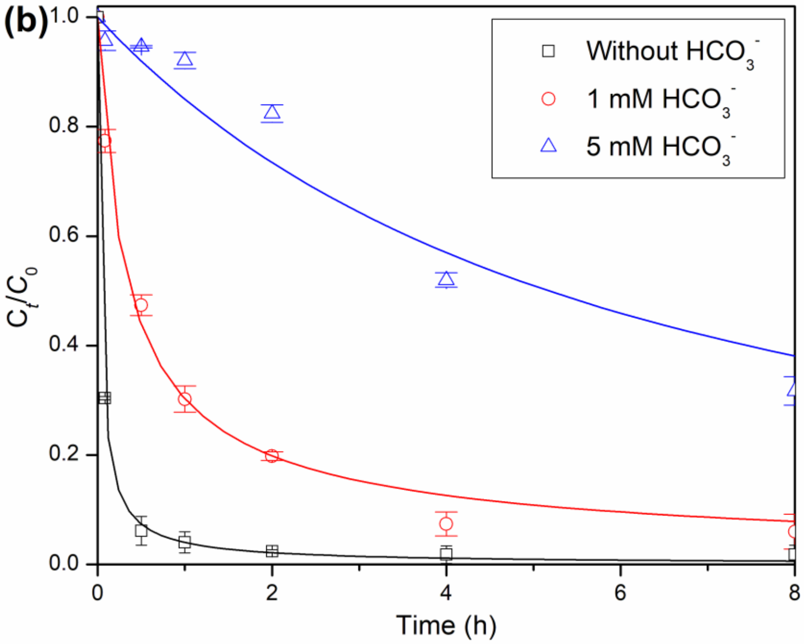
(b)
C_t/C_0
Time (h)
Without HCO_3^-
1 mM HCO_3^-
5 mM HCO_3^-
0.0
0.2
0.4
0.6
0.8
1.0
0
2
4
6
8

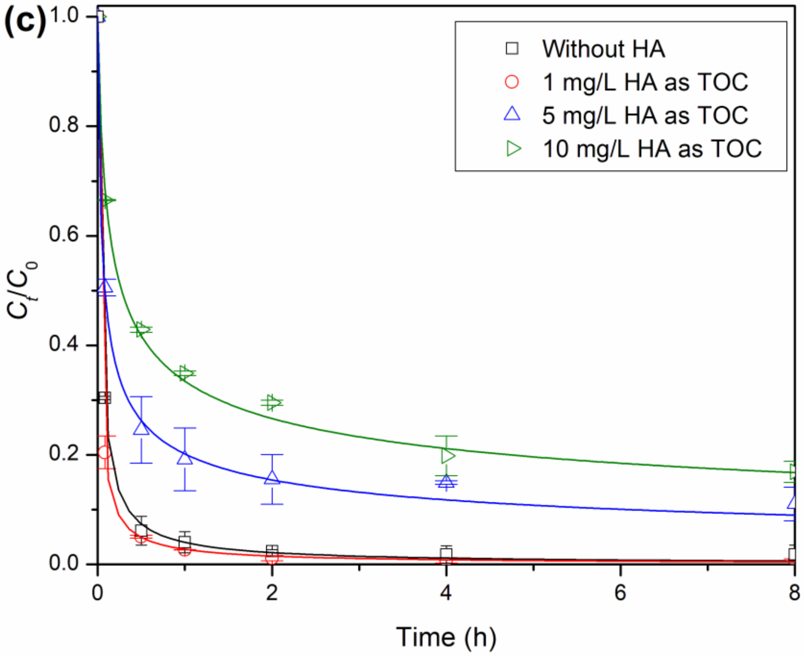
(c)
C_t/C_0
Time (h)
Without HA
1 mg/L HA as TOC
5 mg/L HA as TOC
10 mg/L HA as TOC
0.0
0.2
0.4
0.6
0.8
1.0
0
2
4
6
8

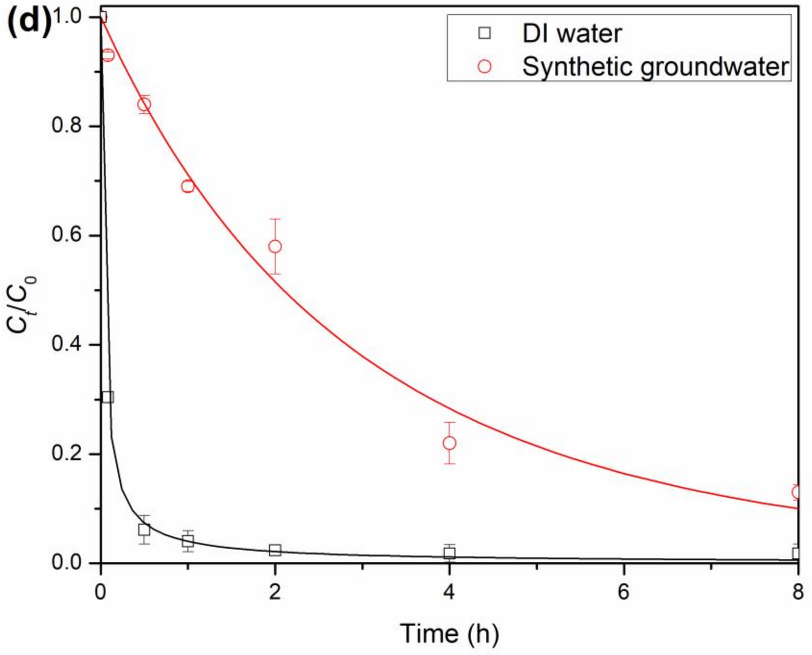

Fig. 2-7. Effects of (a) Na^+ and Ca^{2+} (1 mM), (b) bicarbonate (1-5 mM), (c) humic acid (1-10 mM as TOC), and (d) matrix of synthetic groundwater on removal kinetics of U(VI) by CMC-FeS. Experimental conditions: initial U(VI) = 10 mg/L, FeS = 100 mg/L, CMC-to-FeS molar ratio = 0.0010, Tris buffer = 10 mM, pH = 7.0 ± 0.2, , and temperature = 22 ± 1°C. Synthetic groundwater : 0.286 mM $Ca(NO_3)_2$, 0.312 mM $CaCl_2$, 0.529 mM $MgSO_4$, 0.451 mM Na_2SO_4, 0.0111 mM Na_2CO_3, 0.604 mM $NaHCO_3$, 0.43 mM $KHCO_3$, and 3 mg/L humic acid as TOC. Symbols: experimental data; Lines: retarded first-order model fittings.

2.3.4. Effect of bicarbonate

Bicarbonate is the key alkalinity component in natural waters and is ubiquitous in groundwater. Bicarbonate is prone to complexing with uranium under neutral-basic conditions (Li et al., 2015). Up to 1 mM of bicarbonate has been reported in groundwater at some U-contaminated sites (Hua et al., 2006; Nguyen et al., 2012). **Fig. 2-7b** shows that the presence of 1 mM of bicarbonate notably hindered the U removal rate and decreased the k_{init} from 29.89 h^{-1} to 3.138 h^{-1}, though the removal efficiency remained at 92.6%. To further gauge the limit, the tests were carried out at an unusually high bicarbonate concentration (5 mM). **Fig. 2-7b** shows that the high concentration of bicarbonate decreased U(VI) removal from 98.2% to 68.6% after 8 h of reaction, and diminished the k_{init} to 0.172 h^{-1}. The inhibitive effect is mainly due to the formation of stable uranyl-carbonate complexes. **Fig. 2-5b** presents the speciation of U(VI) in the presence of bicarbonate. At neutral pH, $(UO_2)_2CO_3(OH)_3^-$, $UO_2(CO_3)_2^{2-}$, and $UO_2(CO_3)_3^{4-}$ are the prevalent species, which are subject to electrostatic repulsion by the negative surface of CMC-FeS (**Fig. 2-6**). In addition to hindered adsorption, uranium-carbonate complexes are less efficient electron acceptors, and it was reported that only uranium-hydroxyl species was reduced by hydrogen sulfide in a carbonate-containing system (Hua et al., 2006).

2.3.5. Effect of humic acid

Humic acid is another common groundwater constituent that complexes with U(VI) in the forms of binary $UO_2HA(II)$ and the ternary $UO_2(OH)HA(I)$ complexes at pH > 3 (Křepelová et al., 2006). However, unlike bicarbonate, HA showed some contrasting effects on the U(VI) removal, depending on the HA concentration. With the addition of 1 mg/L HA as TOC, the k_{init} was almost doubled (from 29.89 h^{-1} to 55.78 h^{-1}) and the half-time was shortened by 1.84 times (from 0.019 to 0.035) compared to the HA-free system **Fig. 5c** and **Table 1)**. The enhanced U(VI) uptake is attributed to the adsorption of HA on CMC-FeS, which provided additional binding sites for U(VI) coming from the adsorbed HA macromolecules. The competitive adsorption of HA by FeS was evidenced by the DLS measurements. The mean hydrodynamic size of CMC-FeS decreased from 253 nm (without HA) to 220, 154, and 149 nm in the presence of 1, 5 and 10 mg/L of HA as TOC, respectively. The molecular weight (number-average) of the Leonardite HA was reported to be 3730 (Backett et al., 1987), which is 24 times smaller than that of CMC (90,000). Because the DLS-based size reflects both the core of the FeS particles and sorbed macromolecules (Gong et al., 2014), the decreased DLS size indicates that a notable fraction of sorbed CMC molecules were replaced by the smaller HA molecules. Moreover, the adsorbed HA contains 4.76 and 1.47 μmol/g of carboxyl and phenolic groups, respectively (Fujii et al., 2014), and these soft basic sites provide a higher affinity for binding with the soft uranyl cations. In addition to the enhanced adsorption, the sorbed HA may potentially facilitate the U(VI) reduction by serving as an electron-transfer mediator (Tratnyek et al., 2011). Then prove or disprove this statement. A similar phenomenon was also observed in a study on the effect of HA on U(VI) adsorption by attapulgite (Tan et al., 2017).

However, when the HA concentration was elevated to 5 and 10 mg/L, the k_{init} was reduced to 23.13 and 8.32 h^{-1}, and the U(VI) removal efficiency was decreased to 89.0% and 83.1%, respectively. At high concentrations of HA, the sorbed HA molecules became denser on the surface, which may block and diminish the accessibility of surface sites towards U(VI) (Gong et al., 2014; Ho and Miller, 1985). In addition, excessive replacement of CMC molecules from the surface may compromise the particle stability because HA is a less effective stabilizer than CMC, resulting in some aggregation of the particles. Moreover, at elevated concentrations, the dissolved HA molecules tend to keep more uranium in the solution phase through competitive complexation (Ho and Miller, 1985; Tan et al., 2017).

2.3.6. U(VI) removal in simulated groundwater

To gauge the potential effects of groundwater matrix, the U(VI) removal was tested with simulated groundwater containing various potential inhibitors. **Fig. 2-7d** shows that the k_{init} value was dropped from 29.89 h^{-1} in the DI water system to 0.35 h^{-1} in the groundwater system, with $t_{1/2,\ \mathrm{init}}$ prolonged from 0.035 h to 2.10 h. The rate constant was also lower than those in the systems containing individual inhibitors (1 mM sodium, calcium or bicarbonate, or 5 mg/L HA) (**Figs. 2-7a–2-7c**), indicating the combined effects of the groundwater matrix. Because these co-solutes may not compete for electrons with U(VI), the inhibitive effects are attributed to competitive adsorption, the formation of less absorbable or less reducible U-species, and less favorable surface conditions. For instance, both Ca^{2+} and Mg^{2+} can complex with U(VI) to form $MUO_2(CO_3)_3^{2-}$ and $M_2UO_2(CO_3)_3^0$ (M = Ca^{2+} or Mg^{2+}) (Dong and C, 2008), which are less absorbable or reducible at neutral pH. Likewise, the formation of mixed-ligand complex (UO_2CO_3)HA also inhibits the adsorption, mass transfer, and reduction of U(VI) (Glaus et al., 1995). Despite the retarded reaction rate, ~87% of U(VI) removal was still reached at 8 h.

2.3.7. Mechanism of U(VI) removal by CMC-FeS

To elucidate the underlying reaction mechanism for U(VI), FTIR, XRD, and XPS analyses were carried out to characterize CMC-FeS before and after reaction with U(VI) at pH 7. **Fig. 2-8** presents the FTIR spectra of neat CMC powder, CMC-FeS, and U-laden CMC-FeS. For neat CMC, five peaks were observed at 3459, 2924, 1616, 1419, and 1053 cm^{-1}, respectively, corresponding to the –OH stretching, asymmetric –CH stretching of –

CH_2 groups, asymmetric and symmetric vibrations of COO^- groups and C–O stretching of RCH_2OH (Dong et al., 2016; Gong et al., 2014). When coated on FeS, the –OH stretching shifted from 3459 cm^{-1} to 3387 cm^{-1}, indicating enhanced intermolecular hydrogen bonding between CMC and FeS (He et al., 2007). Similarly, the asymmetric and symmetric vibrations of COO^- groups and the C–O bond stretching showed a blue shift from 1616, 1419, and 1053 cm^{-1} for neat CMC to 1603, 1384, and 1021 cm^{-1} for CMC-FeS, respectively, confirming the important roles of COO^- and C–O in binding CMC on FeS (Lyu et al., 2017). The broad new peak at 470 cm^{-1} can be attributed to the sulfide groups (Chiriţă et al., 2008; Du et al., 2016). After reaction with U(VI), all peaks for CMC-FeS remained, except that the –OH band shifted from 3387 cm^{-1} for CMC-FeS to 3419 cm^{-1} for U-laden CMC-FeS, and the IR frequency was remarkably enhanced, which can be due to the uptake of uranyl hydroxide complexes (**Fig. 2-5a**) (Du et al., 2016). The peak for sulfide decreased after reaction with U(VI), suggesting the consumption of sulfide during the reaction with U(VI). In addition, four new peaks at 1114, 901, 790, and 612 cm^{-1} appeared on the U-laden CMC-FeS spectra. The first two peaks were assigned to S=O vibrations of sulfate and the O=U=O stretching vibration of uranyl (UO_2^{2+}), respectively, while the peaks at 790 and 612 cm^{1} could be due to the Fe–O and Fe–O–H stretching vibrations from FeOOH (Du et al., 2016; Ma et al., 2018; Mesquita et al., 2016). Based on the FTIR results, the direct adsorption of uranyl (UO_2^{2+}) may occur *via* **Eqs.** (**2-5**) – (**2-8**) (Descostes et al., 2010; Duan et al., 2019),

$$\equiv Fe^{+} + H_2O \leftrightarrow \equiv Fe\text{–}OH + H^{+} \quad \textbf{(2-5)}$$

$$UO_2^{2+} + 2(\equiv Fe\text{–}OH) \leftrightarrow (\equiv Fe\text{–}O)_2UO_2 + 2H^{+} \quad \textbf{(2-6)}$$

$$\equiv S^{-} + H_2O \leftrightarrow \equiv S{-}H + OH^{-} \quad \textbf{(2-7)}$$

$$UO_2^{2+} + 2\equiv S{-}H \leftrightarrow (\equiv S)_2UO_2 + 2H^{+} \quad \textbf{(2-8)}$$

where $\equiv Fe^{+}$ and $\equiv S^{-}$ are surface exposed functional groups, whose charges are governed by solution pH. Both $\equiv Fe{-}OH$ and $\equiv S{-}H$ are possible sites for UO_2^{2+} adsorption. Based on the hard-soft acid-base (HSAB) theory, the soft basic sites $\equiv S^{-}$ should have a relatively higher affinity for soft UO_2^{2+} ions (Ma et al., 2018). The predominance of reaction (6) over (4) was indicated by the observation that pH was increased in the first 20 minutes of U(VI) removal by CMC-FeS without a pH buffer (**Fig. 2-9**) (Descostes et al., 2010). In terms of abundance, the XPS survey spectra of neat CMC-FeS (**Fig. 2-11a**) revealed that the nanoparticle surface contained 17.7% of S but only 7.7% of Fe.

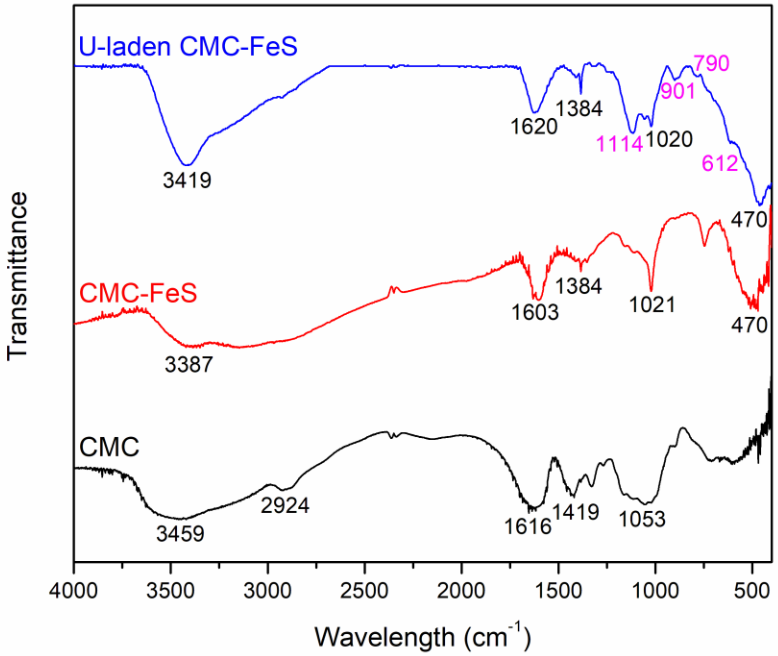

Fig. 2-8. FTIR spectra of neat CMC powder, CMC-FeS nanoparticles, and U-laden CMC-FeS.

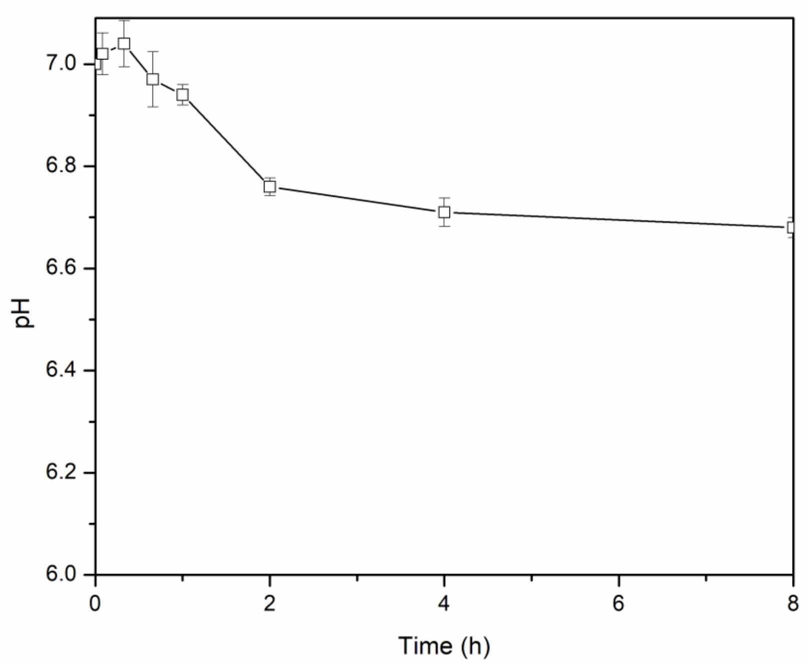

Fig. 2-9. The pH history during U(VI) removal by CMC-FeS in the absence of a pH buffer.

Fig. 2-10 compares the XRD patterns of CMC-FeS before and after reaction with U(VI). For neat CMC-FeS, the diffractions at 18.2°, 30.0°, 39.7°, 49.1°, and 60.4° are assigned to the (001), (101), (111), (200), and (103) planes of mackinawite (FeS) (JCPDS No. 15-0037) (Chen et al., 2015). Besides, six peaks at 14.2°, 23.0°, 26.9°, 36.6°, 46.8°, and 52.4° were also observed. The peak at 23.0° is attributed to elemental sulfur (S^0) (JCPDS No. 42-1278) (B. Li et al., 2015), while the other five peaks are indexed to the (020), (120), (031), (200), and (151) planes of lepidocrocite (γ-FeOOH) (JCPDS 08-0098) (Xing et al., 2016). The presence of elemental sulfur and lepidocrocite indicate the sample was partially oxidized during the unavoidable exposure to air during the characterization process according to **Eq.** (**2-9**) (Bi et al., 2013; Veeramani et al., 2013):

$$\mathrm{FeS(s)} + \frac{3}{4}\mathrm{O_2} + \frac{1}{2}\mathrm{H_2O} = \frac{1}{8}\mathrm{S_8{}^0(s)} + \mathrm{FeOOH(s)} \qquad \textbf{(2-9)}$$

Compared to neat CMC-FeS, all the characteristic peaks of FeS remained for the U-laden CMC-FeS, and in addition, five new peaks were identified at 25.9, 27.4, 31.7, 45.5, 68.8°. Except for the first peak at 25.9° that was attributed to elemental sulfur (JCPDS No. 42-1278) (B. Li et al., 2015), the rest four peaks belong to the (111), (200), (220), and (400) planes of uraninite (UO_2) (JCPDS No. 65-0288) (Frazier et al., 2005). Meanwhile, the mackinawite peaks decreased while the lepidocrocite peaks increased after reaction with U(VI) (**Fig. 2-10**). The XRD results provide direct evidence of reductive conversion soluble U(VI) into UO_2 precipitates, with the oxidation of FeS to FeOOH and S^0, namely, with both Fe^{2+} and S^{2-} serving as the electron donors.

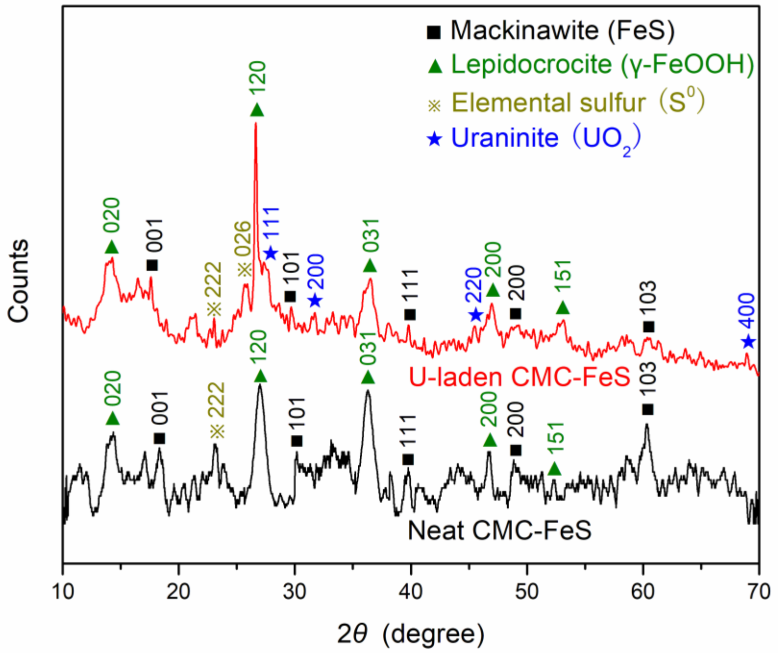

Fig. 2-10. X-ray diffraction patterns of neat CMC-FeS nanoparticles and U-laden CMC-FeS.

XPS analysis (**Fig. 2-11**) was further conducted to examine the surface elemental compositions and oxidation states before and after the reaction with U(VI). The survey spectra (**Fig. 2-11a**) indicate that neat CMC-FeS contained C (38.1%), O (36.5%), S (17.7%), and Fe (7.7%), which were changed to C (27.1%), O (58.1%), S (6.8%), Fe (7.4%) and U (0.6%) after the reaction. The remarkable decrease of the S content signifies the important role of S^{2-} in the reduction of U(VI), and the great increase of O is owing to the uptake of uranyl hydroxide complexes at pH 7 (**Fig. 2-5a**) and partial oxidation of FeS. For neat CMC-FeS, deconvolution of the high-resolution spectra of Fe 2p 3/2 (**Fig. 2-11b**) reveals three peaks at 707.6, 709.5, and 711.7 eV, which are attributed to Fe(II)-S, Fe(II)-O/Fe(III)-S, and Fe(III)-O, respectively (Han and Gao, 2008; Mullet et al., 2002). Likewise, the S 2p spectra (**Fig. 2-11c**) reveal four distinct peaks, namely, S^{2-} at 161.2 eV, S_2^{2-} at 162.2 eV, S_n^{2-} at 163.12 eV and SO_4^{2-} at 168.4 eV (Descostes et al., 2010; Duan et al., 2019). Note that elemental S^0 was not detected by XPS, which may have sublimated under vacuum conditions (Descostes et al., 2010). The existence of Fe(III) and higher valence sulfur species in the virgin FeS sample indicates partial oxidation of the material during characterization, which is in agreement with the XRD results (**Fig. 2-10**).

Upon reaction with U(VI), the Fe 2p 3/2 peaks slightly shifted to 708.2, 709.1 and 710.1 eV. Meanwhile, the percentiles of Fe(II)-S and Fe(II)-O/Fe(III)-S decreased from 20.5% and 45.9% for neat CMC-FeS to 8.8% and 28.5% for U-laden CMC-FeS, respectively, while Fe(III)-O increased from 33.6% to 62.7% (**Fig. 2-11b**). This observation indicates the important role of Fe(II) as an electron donor in the reduction of U(VI). Accordingly, from the S 2p spectra (**Fig. 2-11c**), S^{2-}, S_2^{2-} and S_n^{2-} decreased from 30.7%, 35.0% and 23.8% to 6.4%, 18.8%, and 0%, respectively, while SO_3^{2-}/SO_4^{2-} increased from 10.5% to 74.8% after reaction with U(VI), indicating that the low valence sulfur species (S^{2-}, S_2^{2-} and S_n^{2-}) also served as electron donors in the U(VI) reduction. The results are in agreement with a prior report that the reduction of U(VI) by pyrite was coupled with the oxidation of S to form elementary S and subsequently sulphoxyanions (Descostes et al., 2010). Based on the XRD and XPS results and studies by others (Descostes et al., 2010; Duan et al., 2019; Gallegos et al., 2013; Hua and Deng, 2008; Hyun et al., 2012), the reductive conversion of sorbed U(VI) into U(IV) is described as follows:

$$\equiv UO_2^{2+} + 2Fe^{2+}_{\text{Sorbed or Structural}} + 4H_2O \rightarrow UO_2(s) + 2FeOOH + 6H^+ \qquad \textbf{(2-10)}$$

$$\equiv UO_2^{2+} + \equiv HS^- \rightarrow UO_2(s) + S^0 + H^+ \qquad \textbf{(2-11)}$$

$$3{\equiv}UO_2^{2+} + {\equiv}HS^- + 3H_2O \rightarrow 3UO_2(s) + SO_3^{2-} + 7H^+ \qquad \textbf{(2-12)}$$

$$4{\equiv}UO_2^{2+} + {\equiv}HS^- + 4H_2O \rightarrow 4UO_2(s) + SO_4^{2-} + 9H^+ \qquad \textbf{(2-13)}$$

$$ {\equiv}UO_2^{2+} + {\equiv}S_2^{2-} \rightarrow UO_2(s) + 2S^0 \qquad \textbf{(2-14)}$$

$$5{\equiv}UO_2^{2+} + {\equiv}S_2^{2-} + 6H_2O \rightarrow 5UO_2(s) + 2SO_3^{2-} + 12H^+ \qquad \textbf{(2-15)}$$

$$7{\equiv}UO_2^{2+} + {\equiv}S_2^{2-} + 8H_2O \rightarrow 7UO_2(s) + 2SO_4^{2-} + 16H^+ \qquad \textbf{(2-16)}$$

Regarding the relative contributions of the two electron donors (Fe^{2+} and S^{2-}), the literature has been inconsistent. While the results can vary with different reaction conditions, the general notion has been that both reductants are likely involved in iron sulfide systems as is the case of this study (Hua and Deng (2008). Some researchers claimed that sorbed and structural Fe^{2+} played a primary role in reducing U(VI) using montmorillonite, magnetite or vivianite (Ehrhardt et al., 2010; Veeramani et al., 2011), while others asserted that Fe(II) was inert toward U(VI) reduction in a biogenic mackinawite system (Veeramani et al., 2013). From the thermodynamic aspect, S^{2-} is the more favored reductant than Fe^{2+} based on the standard reduction potential (+0.771 V for Fe^{3+}/Fe^{2+}, +0.144 V for $S(s)/S^{2-}$, -0.659 V for $SO_3^{2-}/S(s)$, and -0.751 V for $SO_4^{2-}/S(s)$. In terms of e-donor capacity, S^{2-} is also a more efficient donor with 8 electrons donated from S^{2-} to SO_4^{2-} compared to only 1 electron from Fe^{2+} to Fe^{3+}. This is supported by the XPS data that upon reaction with U(VI), the SO_3^{2-}/SO_4^{2-} percentile increased by 64.3%, while Fe(III)-O increased by only 29.1%. Fe^{2+} may contribute much less when the FeS dosage is high or when S^{2-} is abundant. For instance, the work by Veeramani et al. (2013) used a dosage of 4390 mg/L of FeS to treat 23.8 mg/L of U(VI) (mass ratio = 184.5:1), while only 100 mg/L of FeS was used in this study to treat 10 mg/L U(VI) (mass ratio of 10:1). As a result, the role of Fe^{2+} was nearly negligible in the former case. Thus, it is plausible that in the FeS system, S^{2-} was the predominant reductant, whereas Fe^{2+} played a supplementary role. Yet, further study is needed to quantify the relative contributions of the two reductants in various forms of iron sulfide.

Deconvolution of the U 4f 7/2 spectra (**Fig. 2-11d**) resulted in two peaks at 379.9 and 382.6 eV, which were assigned to U(IV) (90.1%) and U(VI) (9.9%) (Duan et al., 2019; Shao et al., 2016). This result is in line with the extraction data at pH 7.0 (**Fig. 2-4**), confirming that the reductive immobilization was the predominant mechanism.

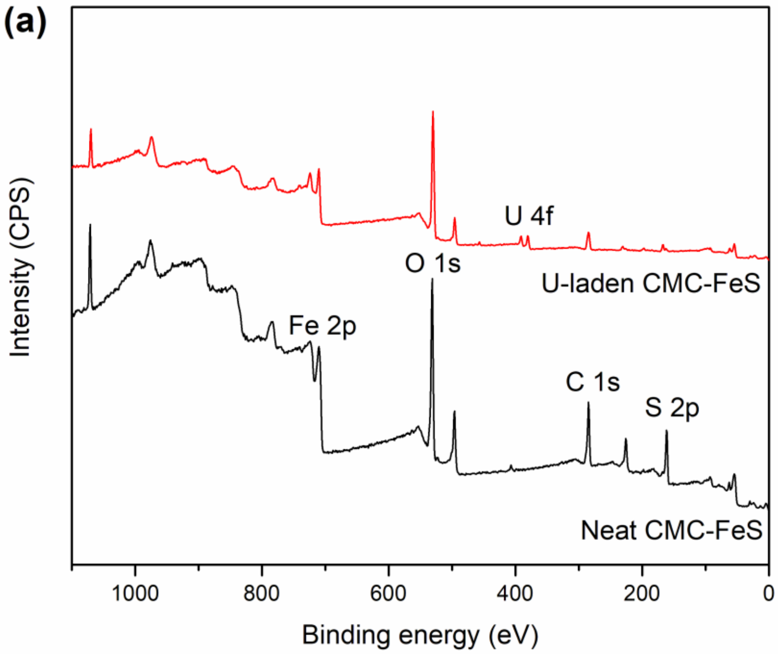

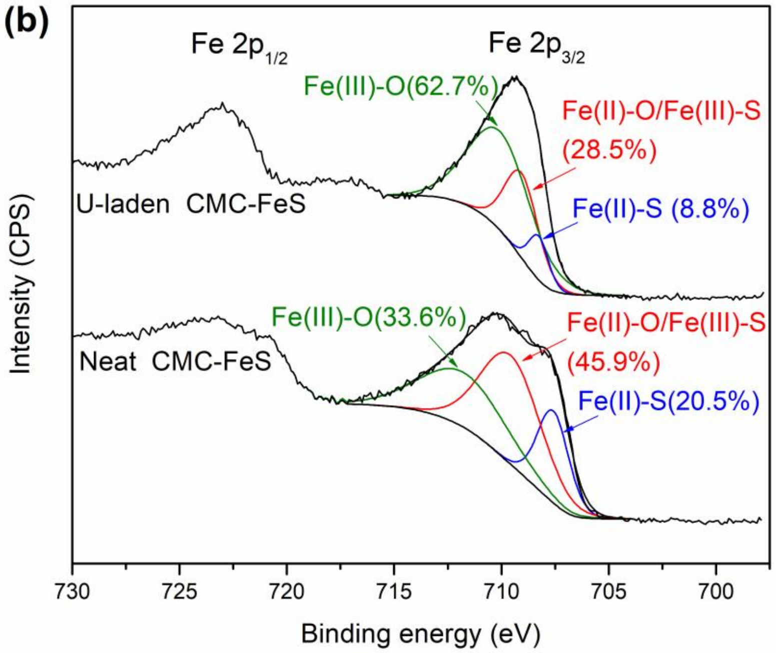
(b)
Fe 2p1/2
Fe 2p3/2
Fe(III)-O(62.7%)
Fe(II)-O/Fe(III)-S
(28.5%)
Fe(II)-S (8.8%)
U-laden CMC-FeS
Fe(III)-O(33.6%)
Fe(II)-O/Fe(III)-S
(45.9%)
Fe(II)-S(20.5%)
Neat CMC-FeS
Intensity (CPS)
730
725
720
715
710
705
700
Binding energy (eV)

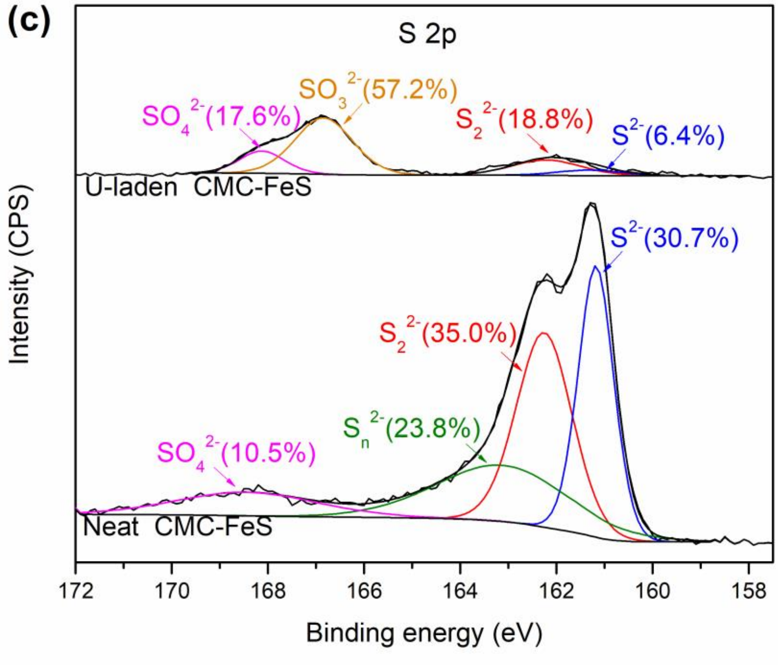
(c)
S 2p
SO4 2-(17.6%)
SO3 2-(57.2%)
S2 2-(18.8%)
S2-(6.4%)
U-laden CMC-FeS
S2-(30.7%)
S2 2-(35.0%)
Sn 2-(23.8%)
SO4 2-(10.5%)
Neat CMC-FeS
Intensity (CPS)
172
170
168
166
164
162
160
158
Binding energy (eV)

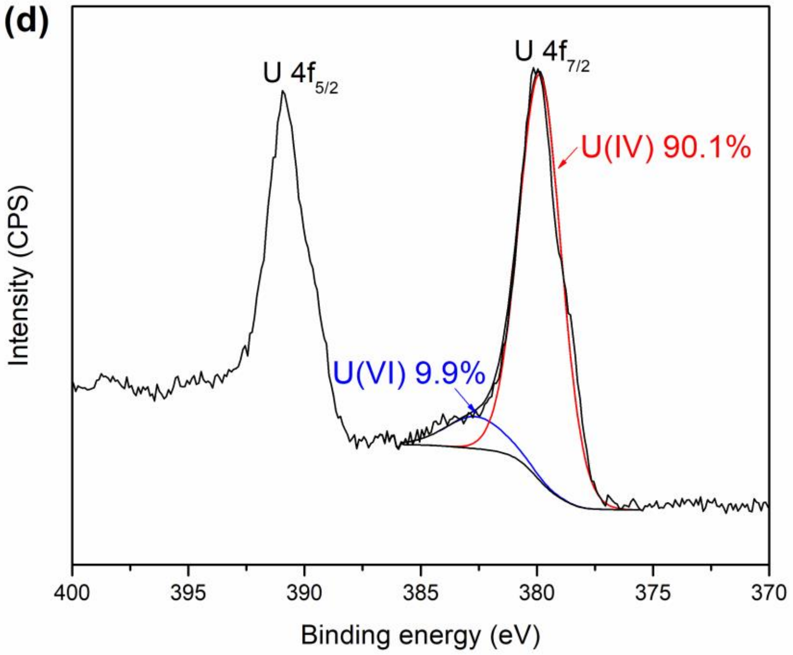

Fig. 2-11. XPS spectra of CMC-FeS before and after reaction with U(VI): (a) survey XPS, (b) high resolution of Fe 2p, (c) high resolution of S 2p, and (d) high resolution of U 4f. U-laden FeS samples were prepared under the following conditions: CMC-FeS dosage = 100 mg/L, initial U(VI) = 10 mg/L, solution volume = 500 mL, pH = 7.0 ± 0.2.

Based on the foregoing analyses, **Fig. 2-12** presents a schematic depiction of the U(VI) removal mechanism by CMC-FeS under various influencing factors. U(VI) removal involves several concurrent processes: 1) rapid adsorption onto the surface of the nanoparticles *via* electrostatic attraction and/or surface complexation between uranyl cations and the surface ≡FeO- and ≡S^- groups, 2) irreversible reduction of sorbed U(VI) predominantly by S^{2-}, Fe(II), and S_2^{2-}, resulting in stable UO_2(s), and 3) oxidation of FeS to γ-FeOOH, S^0, SO_3^{2-}, and SO_4^{2-}. In the presence of Ca^{2+} and/or CO_3^{2-}, binary or ternary soluble anionic or electroneutral complexes including U(VI)-CO_3^{2-} and Ca^{2+}-U(VI)-CO_3^{2-}

are formed, hindering both adsorption and reduction of U(VI). Adsorption of HA on FeS may facilitate U(VI) adsorption and enhance the electron transfer for U(VI) reduction, while high concentrations of HA inhibit the U(VI) removal due to blockage of the reactive sites and/or formation of soluble U(VI)-HA complexes.

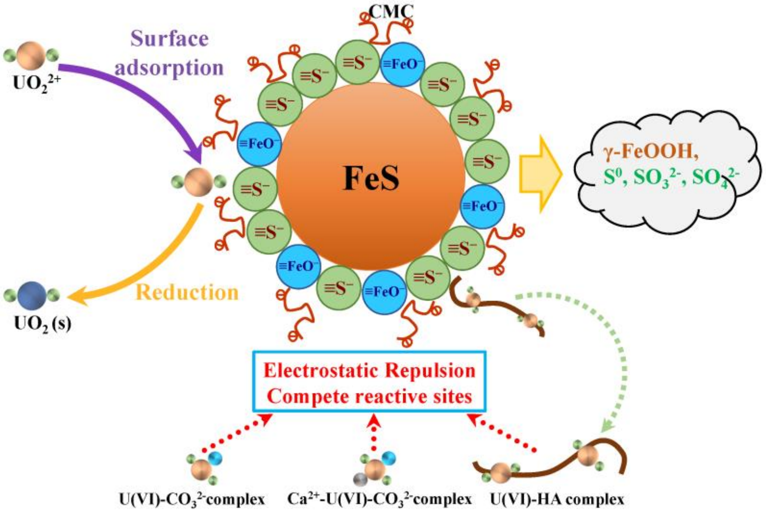

Fig. 2-12. Schematic representation of the reaction mechanism of U(VI) removal by CMC-FeS under various influencing factors.

2.3.8. Stability of immobilized uranium

From the remediation standpoint, it is critical to keep immobilized U in the solid phase without remobilizing into the aqueous phase, i.e., desorption of adsorbed U(VI) or oxidative dissolution of UO_2(s). **Fig. 2-13** shows the concentration histories of U in the aqueous phase under anoxic and oxic conditions following the reductive immobilization treatment, which immobilized ~98% of U in the system. Under the anoxic condition, the soluble U remained at ~2% after aging for 180 days, indicating that the immobilized U remained highly stable. The CARB extraction of the samples aged for 180 days proved that 85.1% of the uranium still existed in the tetravalent state, which was about the same as at

Day 1 (86.6%). The results also indicate the strong physical-chemical integrity of the FeS nanoparticles in the anoxic environment and support the assertion that FeS does not necessarily undergo anoxic corrosion in water (Henderson and Demond, 2013). However, further study is still needed to elucidate the evolution of the FeS and retention mechanism of U(VI). When exposed to air, no U(VI) dissolution was observed in the first 5 days, but gradually increased thereafter, with the aqueous U(VI) concentration reached 12.8% after 30 days and finally 25.8% after the 6-month aging. The CARB extraction showed that nearly all U(IV) was re-oxidized back to U(VI) after the 180 days of exposure, of which ~74% remained associated with the FeS oxidation products. The initial lag stage could be attributed to scavenging of DO by FeS, which preferentially reacted with oxygen and thus shielded U(IV) from being oxidized (Bi et al., 2013; Bi and Hayes, 2014). In addition, the formation of uraninite upon reacting with CMC-FeS (**Fig. 2-10**) may also inhibit the remobilization of U, as uraninite has been known to be more stable and resistant to oxidation compared to non-uraninite species (Bi et al., 2016; Carpenter et al., 2015). In an oxidizing environment, the oxidation of uraninite is considered thermodynamically favorable. Yet, the extent to which uraninite oxidizes depends on the structure and chemistry Namely, namely thermodynamic stability and the oxidation rate will depend on the ability of the structure to accommodate additional oxygen and on its chemical compositions including the intermingled oxidation products of FeS. In addition to the oxidative dissolution, the ingress of atmospheric CO_2 may also remobilize U(VI) via the formation of soluble uranyl-carbonate complexes (Crane et al., 2015). However, under ambient conditions, soluble U(VI)-carbonate complexes tend to be adsorbed by iron oxyhydroxides (i.e., lepidocrocite, **Fig. 2-10**) formed from FeS oxidation (Bi et al., 2013).

As a result, the majority (~74%) of U remained in the solid phase upon the long-term atmospheric exposure.

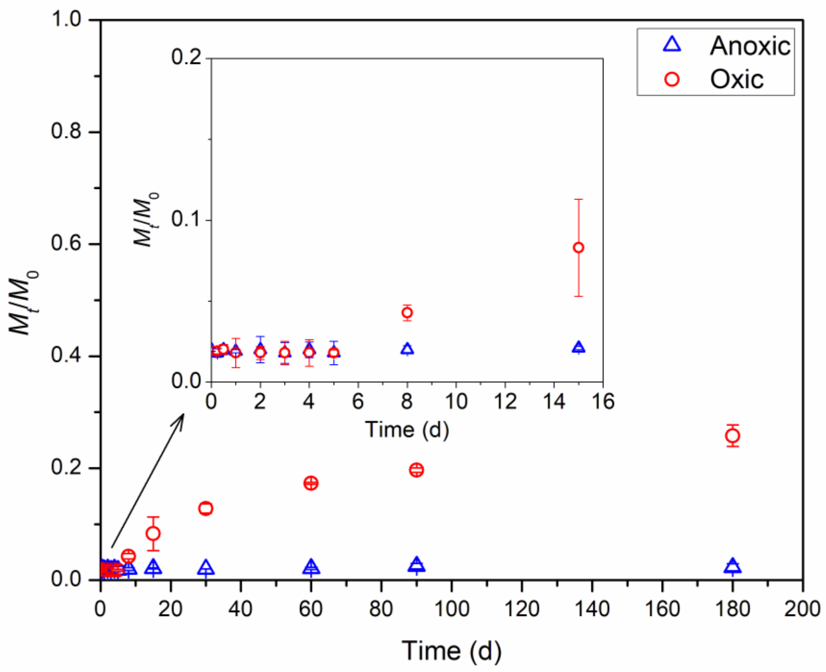

Fig. 2-13. Evolution of immobilized U during the remobilization test under anoxic and oxic conditions. Experimental conditions: initial U(VI) = 10 mg/L, FeS = 100 mg/L as FeS, CMC-to-FeS molar ratio = 0.0010, Tris buffer = 10 mM, pH = 7.0 ± 0.2, and temperature = 22 ± 1°C. M_t is the mass of U in the aqueous phase at time t, and M_0 is the total mass of U in the system.

2.4. Conclusions

This study systematically investigated the effects of various water chemistry parameters on the adsorptive and reductive removal of U(VI) in water using CMC-FeS, the stability of the immobilized U, and the underlying removal mechanism. The key findings are recapped as follows:

1) The optimal CMC-to-FeS molar ratio was determined to be 0.0010, where CMC-FeS exhibited both high physical stability and high reactivity towards U(VI).

2) The retarded first-order kinetic model not only adequately fits the kinetic data of U(VI) removal, but represents a mechanistically sounder model for heterogeneous reactants with decaying reactivity.

3) CMC-FeS was able to achieve rapid removal of U(VI) over the broad pH range of 6.0-9.0 through primary reduction of U(VI) into U(IV), with the fastest removal rates observed at pH 7.0 and 8.0. More U(VI) reduction occurred at lower pH, for instance, 87.2% U(VI) removal at pH 6.0 was due to reduction, compared to 63.3% at pH 9.0.

4) Na^+ ions at normal groundwater concentrations (~1 mM) may not affect the performance of CMC-FeS, while co-existing cations Ca^{2+}(1 mM) may inhibit the removal due to competitive ion exchange and complexation with uranyl oxycations. Bicarbonate at 1 mM didn’t cause significant inhibitive effect, bicarbonate at 5 mM decreased to U(VI) removal from 98.2 to 68.3%.

5) The presence of low concentrations of HA (e.g., 1 mM as TOC) enhanced the U(VI) removal rate from 29.89 h^{-1} to 55.78 h^{-1}, while higher concentrations of HA (5-10 mg/L as TOC) impeded the reaction. CMC-FeS was able to perform well under synthetic groundwater conditions.

6) Both adsorption and reductive conversion of UO_2^{2+} to $UO_{2(s)}$ were responsible for U(VI) removal by CMC-FeS, though reductive immobilization played a primary role (accounting for >90% of U(VI) removed). While S^{2-} and S_2^{2-} were the primary electron donors, sorbed Fe(II) and structural Fe(II) acted as supplementary electron donors for U(VI) reduction.

7) The immobilized U remained highly stable under anoxic condition after 180 days of aging, while ~26% immobilized U was remobilized when exposed to air for 180 days. The long-term stability is attributed to the reductive protecting potential of CMC-FeS, the formation of uraninite and the associated structural resistance to oxidation, and the high affinity of the FeS oxidation products toward U(VI).

Chapter 3. Enhanced immobilization of U(VI) using a new type of FeS-modified Fe^0 core-shell particles

3.1. Introduction

Uranium (U) is a common radionuclide in soil and groundwater. Uranium contamination often results from uranium mining and processing, nuclear energy power plants, nuclear weapon tests and nuclear accidents (Hu et al. 2010). Due to its toxicity, bioaccumulation and very long half-life (4.5×10^9 years for ^{238}U) (Cai et al. 2017), uranium contamination of soil and groundwater has been a major environmental concern over the last half-century (Domingo 2001). To mitigate human exposure, EPA revised the radionuclides regulation in 2000 and set a maximum contaminant level of 30 μg/L in drinking water (Liu et al. 2017). Typically, U exists in the aquatic systems primarily in two oxidation states, i.e., U(VI) and U(IV), with the chemical forms UO_2^{2+} and UO_2. Hexavalent uranium (uranyl) is water-soluble, mobile and more of toxic concern in the environment, while tetravalent uranium is only sparingly soluble ($K_{sp} = 2.5\times10^{-53}$) and immobile (Bi et al. 2013). Adsorption of U(VI) and other radionuclides by various adsorbents has been investigated, including carbon-based materials (Cai et al. 2017, Linghu et al. 2017, Chang et al. 2017, Li et al. 2018, Zhu et al. 2018), metal oxides (Song et al. 2019, Yin et al. 2018, Huang et al. 2018), and metal-organic frameworks (MOFs) (Liu et al. 2017, Chen et al. 2017, Zheng et al. 2017, Wang et al. 2015, Sheng et al. 2017, Zhu et al. 2017). Yet, reductive immobilization of U(VI) to U(IV) has been widely considered as a promising and effective strategy to immobilize U(VI) in water (Liu et al. 2018, Shao et al. 2015).

Zero valent iron (ZVI) has been one of the most widely studied reductants for U(VI) reduction due to effective reducing power, low cost and non-toxic characteristics (Li et al. 2015, Zhao et al. 2016). Fiedor et al. (Fiedor et al. 1998) reported that ZVI can effectively reduce U(VI) and both U(VI) and U(IV) were observed on the surface of spent ZVI, indicating that both reductive precipitation and adsorption of U(VI) were taking place. Under anoxic conditions, U(VI) is reduced by ZVI via:

$$1/2Fe^{2+} + e^{-} \leftrightarrow 1/2Fe^{0} \qquad E_0 = -0.44\ V \tag{3-1}$$

$$Fe^{3+} + e^{-} \leftrightarrow Fe^{2+} \qquad E_0 = 0.77\ V \tag{3-2}$$

$$1/2UO_2^{2+} + 2H^{+} + e^{-} \leftrightarrow 1/2U^{4+} + H_2O \qquad E_0 = 0.327\ V \qquad \log K = 9.02 \tag{3-3}$$

$$U^{4+} + 2H_2O \leftrightarrow UO_2 + 4H^{+} \qquad \log K_{sp} = -4.67 \tag{3-4}$$

Under conditions of environmental interest, the overall reductive precipitation process for either Fe^0 or Fe^{2+} (in acidic condition) as the reducing agent is thermodynamically favorable.

However, ZVI is not thermodynamically stable in water and is prone to oxidation by water and dissolved oxygen (DO) (Fan et al. 2016, Henderson and Demond 2013). The corrosion reactions compete for the electrons with the target contaminants, resulting in diminished reactive life and less effective use of the electrons (or loss of selectivity). In addition, due to the quick loss in ZVI's reducing power, the material also loses its ability to prevent the reduced U(IV) from being re-oxidized.

Reduction and speciation of U(VI) by ZVI depends on a number of factors, including reactivity and specific surface area of ZVI particles, presence of carbonate, ionic strength, dissolved organic matter (DOM), and structure, composition, and reactivity of iron corrosion products (Noubactep et al. 2003).

Over the last decade or so, iron sulfide (FeS) particles have been found effective for uranium sorption and reduction (Hua and Deng 2008, Hyun et al. 2012). Compared to ZVI, FeS offers weaker but longer-lasting reducing power, which is governed by the following reactions:

$$FeS \leftrightarrow Fe^{2+} + S^{2-} \qquad \log K_{sp} = -17.3 \qquad \textbf{(3-5)}$$

$$S^0(s) + 2e^- \leftrightarrow S^{2-} \qquad E_0 = -0.41 \qquad \textbf{(3-6)}$$

$$S^0(s) + H^+ + 2e^- \leftrightarrow HS^- \qquad E_0 = -0.06 \qquad \textbf{(3-7)}$$

$$S^0(s) + 2H^+ + 2e^- \leftrightarrow H_2S(g) \qquad E_0 = 0.14 \qquad \textbf{(3-8)}$$

$$H_2SO_3 + 4H^+ + 4e^- \leftrightarrow S + 3H_2O \qquad E_0 = -0.94 \qquad \textbf{(3-9)}$$

$$SO_4^{2-} + H_2O + 2e^- \leftrightarrow SO_3^- + 2OH^- \qquad E_0 = 0.45 \qquad \textbf{(3-10)}$$

Moreover, FeS does not undergo anoxic corrosion in water and can provide redox buffering capacity to prevent reduced uranium from being re-oxidized (Henderson and Demond 2013, Carpenter et al. 2015). FeS has a higher absolute electronegativity (5.02 eV) (Xu and Schoonen 2000) than that of Fe^0 (4.04 eV) (Pearson 1988), and it is a semiconductor with good electron conductivity resulting from its low band gap (E_g = 0.1 eV) (Du et al. 2016). FeS is also reported to has a lower pH of point of zero charge (pH_{PZC})

(2.9) (Widler and Seward 2002) than that of Fe^0 (7.5) (Su et al. 2015), which can facilitate sorption of cations through electrostatic attraction forces.

Researchers have tested various ways to suppress the water corrosion rate. For instance, researchers have developed so-called sulfidated ZVI (S-ZVI), which inherited the merits of both Fe^0 and FeS, with improved reactivity and selectivity towards target contaminants; in addition, S-ZVI retained the magnetic property of Fe^0 and displayed prolonged oxidation buffering capacity (Fan et al. 2014, Fan et al. 2017, Gong et al. 2017, Li et al. 2017). Typically, S-ZVI is prepared using sulfide or dithionite as the sulfur source (Li et al. 2017). Kim et al. (Kim et al. 2011) prepared S-ZVI by directly reducing Fe^{3+} with a mixture of borohydride and dithionite solution, where sulfide is supplied by decomposition of dithionite. In this case, the resulting S-ZVI particles are essentially a mixture of randomly distributed FeS and Fe^0 phases. Because of the complex reactions involved, it is difficult to control the formation and structure of S-ZVI (e.g., phase distribution and S:Fe^0 ratio). To preserve the reactivity of ZVI, the core-shell structure appears more rational as the sulfidated shell can shield the core Fe^0 from being corroded by water or other side reactions. To this end, a two-step process has been reported. First, ZVI was prepared through the conventional borohydride reduction approach with or without a stabilizer; then Na_2S or $Na_2S_2O_4$ was added as the sulfide source to allow FeS shell to grow on the surface of the mature Fe^0 (Fan et al. 2016). In this case, however, the source of Fe^{2+} was from the corrosion of the pre-synthesized Fe^0, i.e., the formation of the FeS shell is at the expense of Fe^0 core, which would cause the loss of the reducing power of the core ZVI. In addition, as the shell builds up, longer reaction time is needed. Therefore, it is desirable to modify these methods to minimize the reactivity loss of ZVI during the preparation and to maximize the reactive longevity.

To demonstrate the advantages of S-ZVI, researchers have tested the performances in reductive dechlorination of chlorinated solvents (e.g., trichloroethylene) (Kim et al. 2011, Dong et al. 2018, Han and Yan 2016), and reductive sequestration of heavy metals or radionuclides (e.g., Cr and Tc) (Du et al. 2016, Gong et al. 2017, Fan et al. 2013). However, to our knowledge, there has been no report on the application of sulfidated ZVI for reductive immobilization of uranium.

The overall goal of this study was to prepare a new type of FeS-modified ZVI (FeS@Fe^0), and test the material for immobilization of U(VI) in water. The specific objectives were to: 1) prepare FeS@Fe^0 through a facile one-pot, two-step reaction process, and optimize the synthesis conditions; 2) test the material for enhanced reactivity, selectivity, and reactive longevity when used for reductive immobilization of U(VI); 3) examine the effects of water chemistry on the performance of FeS@Fe^0, and 4) elucidate the underlying reaction mechanisms.

3.2. Materials and methods

3.2.1. Chemicals

The following chemicals (analytical grade or higher) were used in this study: ferrous chloride tetrahydrate ($FeCl_2·4H_2O$, Alfa Aesar, Ward Hill, MA, USA), sodium borohydride ($NaBH_4$, TCI America, Portland, OR, USA), sodium sulfide nonahydrate ($Na_2S·9H_2O$, Alfa Aesar, Ward Hill, MA, USA), uranyl acetate dihydrate ($UO_2(CH_3COO)_2·2H_2O$, U in the form of ^{238}U, International Bio-Analytical Industrial Inc., FL, USA), 2-

Morpholinoethanesulfonic acid (MES buffer, TCI America, Portland, OR, USA), Tris (hydroxymethyl) aminomethane (Tris buffer, Acros Organics, Morris Plains, NJ, USA), sodium bicarbonate ($NaHCO_3$, Fisher Scientific, Fair Lawn, NJ, USA), humic acid (HA, Leonardite Humic Acid Standard, 64% of total organic carbon (TOC), St. Paul, MN, USA), sodium chloride (NaCl), calcium chloride ($CaCl_2$) and copper (II) chloride ($CuCl_2$) (Sigma-Aldrich, St. Louis, MO, USA).

3.2.2. Preparation of FeS@Fe^0, Fe^0, and FeS

FeS@Fe^0 particles were prepared *via* a facile two-step reaction process in one pot. First, each 10 mL of a $FeCl_2·4H_2O$ solution (2 g/L as Fe) was added into each 70 mL of Millipore deionized water (18.2 MΩ cm) in three 250-mL flasks, which was pre-purged with high purity nitrogen for 30 min. The mixtures were mixed for 10 min. Then, 10 mL of a $NaBH_4$ solution (0.9, 1.35 and 1.8 g/L as $NaBH_4$) was injected into the three Fe^{2+} solutions under vacuum and shaking (200 rpm) to reduce, respectively, 1/3, 1/2 and 2/3 of the total Fe^{2+} into Fe^0 according to **Eq.** (**3-11**). The flasks were shaken for 10 min to achieve full growth of the Fe^0 core. Subsequently, 10 mL of a $Na_2S·9H_2O$ solution (5.71, 4.29 and 2.86 g/L as $Na_2S·9H_2O$) was dropwise added to the three Fe^0 suspensions, which would precipitate the remaining 2/3, 1/2 and 1/3 of Fe^{2+}, respectively, according to **Eq.** (**3-12**). The FeS precipitates are expected to *in situ* coat the Fe^0 core, resulting in the desired Fe^0-core and FeS-shell structure. The resulting particles are denoted as FeS@Fe^0-2/1, FeS@Fe^0-1/1, and FeS@Fe^0-1/2, with the numbers indicating the theoretical FeS/Fe^0 molar ratios. The total Fe was kept at 0.2 g/L as Fe in all cases.

$$Fe^{2+} + 2BH_4^- + 6H_2O = Fe^0(s) + 2B(OH)_3 + 7H_2 \quad \textbf{(3-11)}$$

$$Fe^{2+} + S^{2+} = FeS(s) \quad \textbf{(3-12)}$$

For comparison, plain ZVI or FeS particles were also prepared at the same concentration (0.2 g/L as Fe) through complete borohydride reduction or FeS precipitation following the stoichiometry of **Eqs.** (**3-11**) and (**3-12**). All prepared particle suspensions were purged with nitrogen and tested freshly.

3.2.3. Characterizations

The particles were characterized with aspects to various physical-chemical properties. The zeta potential (ζ) was determined by the use of a Malvern Zetasizer Nano ZS (Malvern Instrument, Worcestershire, UK). The morphology of particles was analyzed using a Zeiss EM10 transmission electron microscope (TEM, Zeiss, Thornwood, NJ, USA) operated at 60 kV. High angle annular dark-field (HAADF) images were collected using a spherical aberration corrected scanning transmission electron microscopy (CS-STEM, Hitachi HD-2700, Japan) with a cold field emission gun operated at 200 kV. X-ray energy dispersive spectroscopy (XEDS) analysis was conducted on a Bruker Quantax 400 with an XFlash 6T|60 silicon drift detector (SDD) to map the surface elements. For TEM and STEM imaging, samples were prepared by placing a drop of a dilute nanoparticle suspension on a 200-mesh holey carbon-coated copper grid (Electron Microscopy Sciences, Hatfield, PA, USA) in a nitrogen-filled glovebox and then dried under nitrogen protection. The crystal structure of the particles was analyzed on Bruker D2 PHASER X-ray diffractometer (XRD, Bruker AXS, Germany) using Cu $K\alpha$ radiation ($\lambda = 1.5418$ Å) and at a scanning rate (2θ) of 3°/min. The magnetic properties of the particles were measured by a Physical Property Measurement System (PPMS DynaCool-VSM, Quantum Design, USA). Fourier transform infrared spectroscopy (FTIR) analysis was carried out on a Nicolet iS50 FTIR spectrometer (Thermal Fisher Scientific, Madison, WI, USA) to obtain the functional groups with a scanning range of 4000−400 cm^{-1}. The surface elemental compositions and oxidation states before and after reaction with U(VI) were analyzed obtained by an AXIS-Ultra X-ray photoelectron spectroscopy (XPS, Kratos, England) using Al *K*α X-ray at 15 kV and 15 mA. The standard C 1s peak (binding energy, $E_b = 284.80$ eV) was used to calibrate all the peaks and eliminate the static charge effects, and the results were analyzed using the CasaXPS 2.3 software. To get powder samples of the particles, the neat particles were prepared as suspension (0.2 g/L as Fe) and then collected by centrifuging (8000 rpm). The particles were rinsed three times with nitrogen purged DI water, dried under nitrogen blowing, and stored in a nitrogen-filled glovebox before the characterizations. For U-laden samples, the particles were first allowed to react with U(VI) for 24 h following the procedure as described in Section 2.5 before the centrifugation.

3.2.4. Resistance to oxidation

To test the anti-oxidation capabilities of different types of particles, suspensions of Fe^0, FeS, and FeS@Fe^0 were tested under vigorous aeration, and variation in oxidation-reduction potential (ORP) was measured over time. Briefly, each 100 mL of freshly prepared Fe^0, FeS, FeS@Fe^0-2/1, FeS@Fe^0-1/1, or FeS@Fe^0-1/2 suspensions (0.2 g/L as Fe) was diluted with 300 mL of deoxygenated DI water in 500 mL polycarbonate bottles, with the suspension pH buffered at 6.5 ± 0.2 by 10 mM of the MES buffer. Then, the bottles were placed on a shaker (200 rpm) with the suspensions open to the air. The ORP of the suspensions was then followed for 2 h.

3.2.5. Reductive immobilization of U(VI): Batch kinetic tests

Effect of FeS:Fe^0 molar ratio. Batch kinetic tests were conducted in duplicate in 500 mL polycarbonate bottles at 22 ± 1 ºC under anoxic conditions. The kinetic tests were initiated by adding 100 mL of a freshly prepared Fe^0, FeS, FeS@Fe^0-2/1, FeS@Fe^0-1/1 or FeS@Fe^0-1/2 suspension (0.2 g/L as Fe) into 300 mL of a deoxygenated U(VI) solution (U(VI) = 6.67 mg/L, with a proper pH buffer). The resulting experimental conditions were: initial U(VI) = 5 mg/L, particle dosage = 0.05 g/L as Fe, and pH buffer (MES) = 10 mM. Similar U(VI) concentration was detected in groundwater of the 300 and 200-BP areas at the Hanford site (5.6 mg/L) (Energy 2015) and was used by several researchers (Liu et al. 2017, Zheng et al. 2017). The bottles were then placed on a shaker (200 rpm) with nitrogen purging. After predetermined time intervals, each 5 mL of the suspension was sampled and immediately filtered through a polyethersulfone membrane (PES, 0.22 µm), and the filtrate was analyzed for U(VI) remaining in the aqueous phase. To determine U(VI) and U(IV) that were adsorbed on the particles, a widely used anoxic bicarbonate/carbonate (CARB) extraction method was followed (Liu et al. 2018, Hyun et al. 2012). Briefly, 25 mL of a suspension (which was thoroughly mixed) after the reaction was transferred to a 50 mL polycarbonate bottle pre-loaded with 25 mL of CARB extraction solution consisting of sodium carbonate (28.8 mM) and sodium bicarbonate (5.6 mM) under N_2 atmosphere. The mixture was vortexed for 1 min and then allowed to react for 1h on an end-over-end rotator. Upon filtration through 0.22 µm PES membrane, the U(VI) in the filtrate was measured, which includes both the aqueous U(VI) and extractable U(VI) from the particles. Consequently, U(IV), which is not CARB-extractable, was quantified per mass balance calculations.

Effects of water chemistry on U(VI) removal. To test the effects of water chemistry conditions on U(VI) removal, FeS@Fe^0-1/1 was further tested for U(VI) immobilization under various solution pH, bicarbonate, DOM, and cation (Na^+, Ca^{2+}, and Cu^{2+}) concentrations. The pH effect was tested by varying the solution pH from 5.5 to 9.0, where the MES buffer (10 mM) was used to keep the pH at 5.5 or 6.5, and the Tris buffer (10 mM) was used at pH 8.0 and 9.0. Control tests indicated that both buffers had no significant effect on the U(VI) removal. To gauge the effects of bicarbonate, DOM or coexistent cations, the kinetic tests were also carried out in the presence of 1 to 5 mM of HCO_3^-, 1 to 10 mg/L as TOC of HA or 1 mM of Na^+, Cu^{2+}, and Ca^{2+}. Bicarbonate was found at ~1 mM in the groundwater of the Hanford site (a major uranium-contaminated site) (Nguyen et al., 2012, Qafoku et al., 2005), and dissolved organic carbon (DOC) in the range from 1.8 to 32.3 mg/L at the site (Moser et al., 2003). Na^+ and Ca^{2+} were reported to be major cations in U(VI)-contaminated groundwater with concentrations ranging from 0.5 to 1.5 mM (Nguyen et al., 2012, Qafoku et al., 2005). In addition, Cu(II) was reported to be disposed together with U(VI) in the North Process Pond (NPP) in the 300 area of the Hanford site (Arai., et al., 2007), and researchers have tested the effect of Cu(II) (0.25-0.50 mM at pH 5.0) on the removal of U(VI) in wastewater (Li et al., 2018, Zhu et al., 2018). Thus, the effects of these cations were also tested ($Ca^{2+} = Na^+ = 1$ mM, $Cu^{2+} = 0.04$ mM, pH = 6.5).

To assess the effect of particle aging or water corrosion on the reactivity of the particles, the Fe^0 and FeS@Fe^0-1/1 suspensions (0.2 g/L as Fe) were aged for up to 21 days in the bottles tightly sealed with rubber stoppers and stored in a nitrogen-filled glovebox. The aged particles were then tested for U(VI) removal following the same procedure as described above.

3.2.6. Analytical methods

Aqueous U and Fe were determined on an inductively coupled plasma optical emission spectrometer (ICP-OES, Varian 710-ES, Palo Alto, CA, USA) and the detection limit was 0.08 mg/L for U and 0.05 mg/L for Fe. Solution pH, ORP and DO were measured by an Oakton benchtop pH 510 meter, a 2700 ORP meter, and a DO 700 meter (Oakton, CA, USA), respectively. TOC was determined using a Tekmar Dohrmann Pheonix 8000 UV-Persulfate TOC analyzer (Mason, OH, USA) with a detection limit of 0.1 mg/L.

3.3. Results and discussion

3.3.1. Material characterizations

Fig. 3-1 displays XRD patterns of Fe^0, neat FeS@Fe^0-1/1 and U-laden FeS@Fe^0-1/1. For Fe^0, the peak at 44.7° is ascribed to phase (110) of α-Fe^0 (Li et al. 2015, Du et al. 2016, Hu et al. 2017a). For FeS@Fe^0-1/1, the same α-Fe^0 peak was observed; in addition, two new peaks at around 16.4° and 49.8° were evident, which are attributed to phases (001) and (200) of mackinawite (Wolthers et al. 2003). Hyun et al. (Hyun et al. 2012) reported that mackinawite is the first FeS phase to form under sulfate-reducing conditions. The XRD results indicate that Fe^0 and FeS co-existed in the synthesized FeS@Fe^0-1/1.

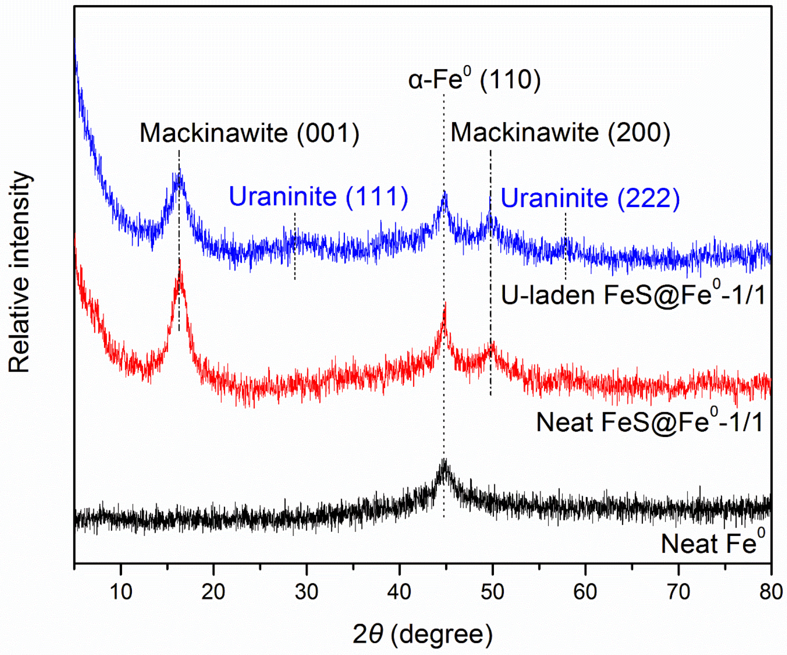

Fig. 3-1. X-ray diffraction patterns of Fe^0, neat FeS@Fe^0-1/1, and U-laden FeS@Fe^0-1/1.

Fig. 3-2a presents a representative TEM image of FeS@Fe^0-1/1 and **Fig. 3-2b** shows the STEM-HAADF image. Both images reveal the core-shell structure, i.e., a solid Fe^0 core with a flaky FeS shell (Gong et al. 2012). Based on TEM images of 60 primary particles, the mean particle size was calculated to be 114.8 ± 26.7 nm (mean ± SD) (with a core size of ~86 nm and shell thickness of ~27 nm). A similar core-shell structure was reported for particles prepared through other methods (Gong et al. 2017, Cao et al. 2017, Song et al. 2017), though the extent of the FeS coating varied. The line scan profiles (**Fig. 3-2c**) show that the Fe content was much higher in the core than in the shell, whereas the S content remained uniform. The Fe profile also suggested a shell thickness of ~25 nm. The elemental mappings (**Figs. 3-2d-2f**) further confirmed the core-shell structure of the composite material.

Compared to the dithionite method (Kim et al. 2011), our two-step reaction method offers improved control of the formation and the core-shell structure (e.g., phase distribution and S:Fe^0 ratio); and compared to the Fe^0-sacrificial method (Fan et al. 2016), our method may better preserve the reducing power of the core ZVI.

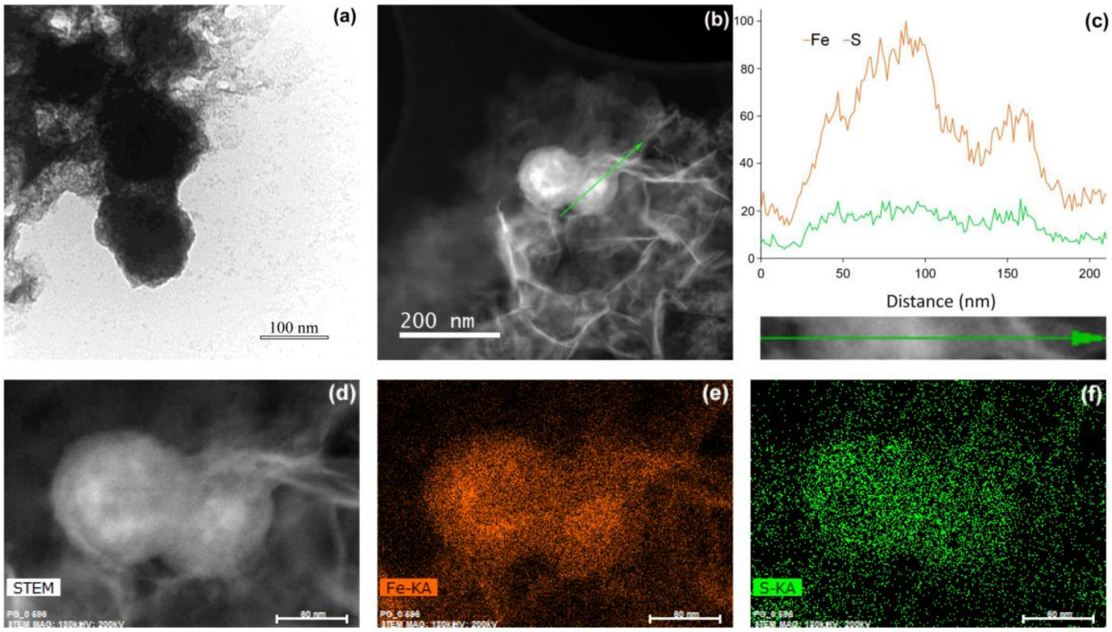

Fig. 3-2. (a) TEM image of FeS@Fe^0-1/1 (FeS:Fe molar ratio = 1:1); (b) STEM-HAADF image of FeS@Fe^0-1/1; (c) XEDS line scan profiles of Fe and S of (b); (d) STEM-HAADF image of representative FeS@Fe^0-1/1, and (e) and (f) XEDS mapping data of (d).

Magnetic characterization (**Fig. 3-3**) indicated that FeS@Fe^0-1/1 exhibited a much lower saturation magnetization (Ms) value (57.1 emu/g) than that of Fe^0 (144.7 emu/g). This is reasonable because FeS is an antiferromagnetic material, which is much weaker than the ferromagnetic Fe^0. Moreover, as ferromagnetic materials undergo much stronger magnetic dipolar interactions, the resulting Fe^0 core showed a much higher atomic density than the FeS shell. The antiferromagnet-ferromagnet coupling interactions also account for the attachment of FeS on Fe^0, for instance, through a mechanism known as exchange bias, where the surface atoms of the antiferromagnet align with the surface atoms of the ferromagnet (Forrester and Kusmartsev 2014). Moreover, compared to pristine Fe^0 particles, the coating of weaker magnetic FeS on Fe^0 is expected to diminish aggregation of the resulting FeS@Fe^0 particles due to the steric stabilization effect (Song et al. 2017). The reduced aggregation of FeS@Fe^0 was confirmed by comparing TEM images of FeS@Fe^0 and Fe^0 particles. Another practically useful attribute of FeS@Fe^0-1/1 is that it retained the magnetic property, and thus the particles can be easily separated from water through an external magnetic field. This differs from S-ZVI prepared by other methods. For instance, Gong et al. (Gong et al. 2017) reported that S-ZVI particles prepared by dithionite reduction of Fe^{3+} lost magnetic property when the S/Fe molar ratio was above 0.207., and Fan et al. (Fan et al. 2016) found that dithionite converted most ZVI to non-magnetic FeS.

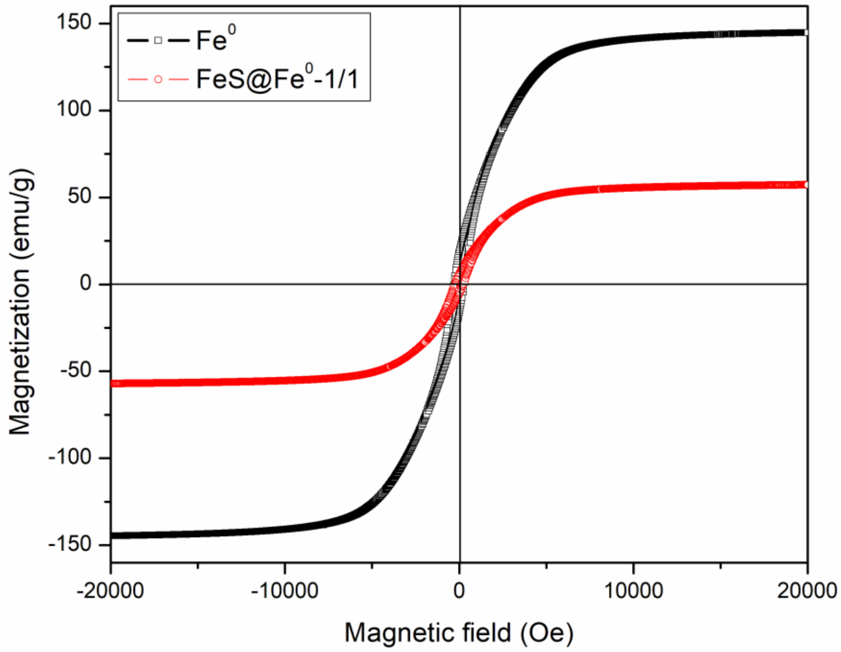

Fig. 3-3. Magnetization curves of Fe^0 and $FeS@Fe^0$-1/1.

Taken together, the two-step method in this work has the following advantages over the dithionite reduction method: 1) it can produce the desired core-shell structure, 2) it is easier to control the compositions of resulting $FeS@Fe^0$ (i.e., $FeS:Fe^0$ ratio), and 3) it may better preserve the magnetic and redox properties of the core ZVI even at higher S/Fe molar ratios.

Fig. 3-4 shows zeta potential profiles of Fe^0 and $FeS@Fe^0$-1/1 in the solution pH range of 4.0 to 9.0. While the pristine Fe^0 particles displayed a pH_{PZC} of 7.3, the FeS-coated Fe^0 showed a much lower pH_{PZC} of 5.1, which is due to the coating of FeS, which has a much lower pH_{PZC} (2.9) (Widler and Seward 2002). The much more negative surface potential of $FeS@Fe^0$-1/1 than Fe^0 in the normal pH range is conducive to interacting with cationic contaminants such as UO_2^{2+} and other cationic U(VI) species (**Fig. 3-5**).

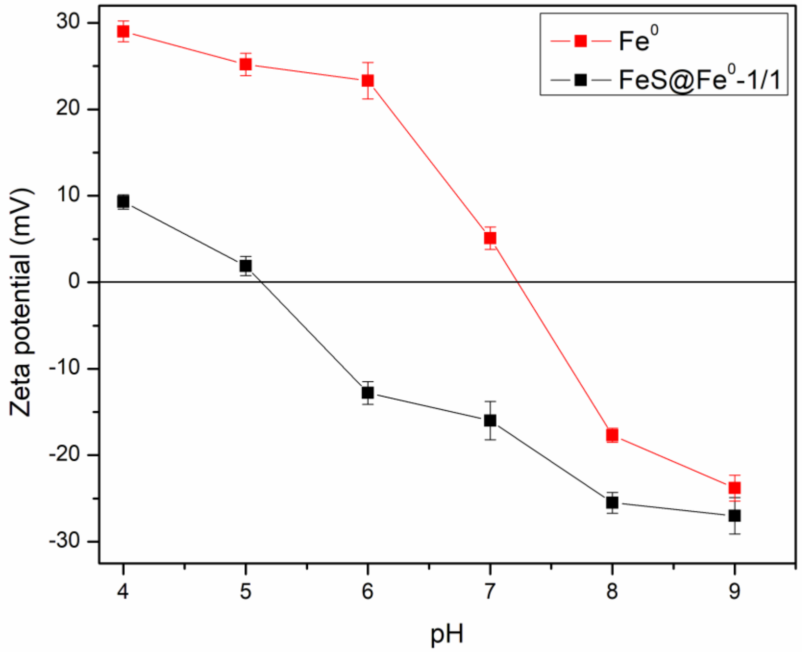

Fig. 3-4. Zeta potential of pristine Fe^0 and FeS@Fe^0-1/1 as a function of solution pH.

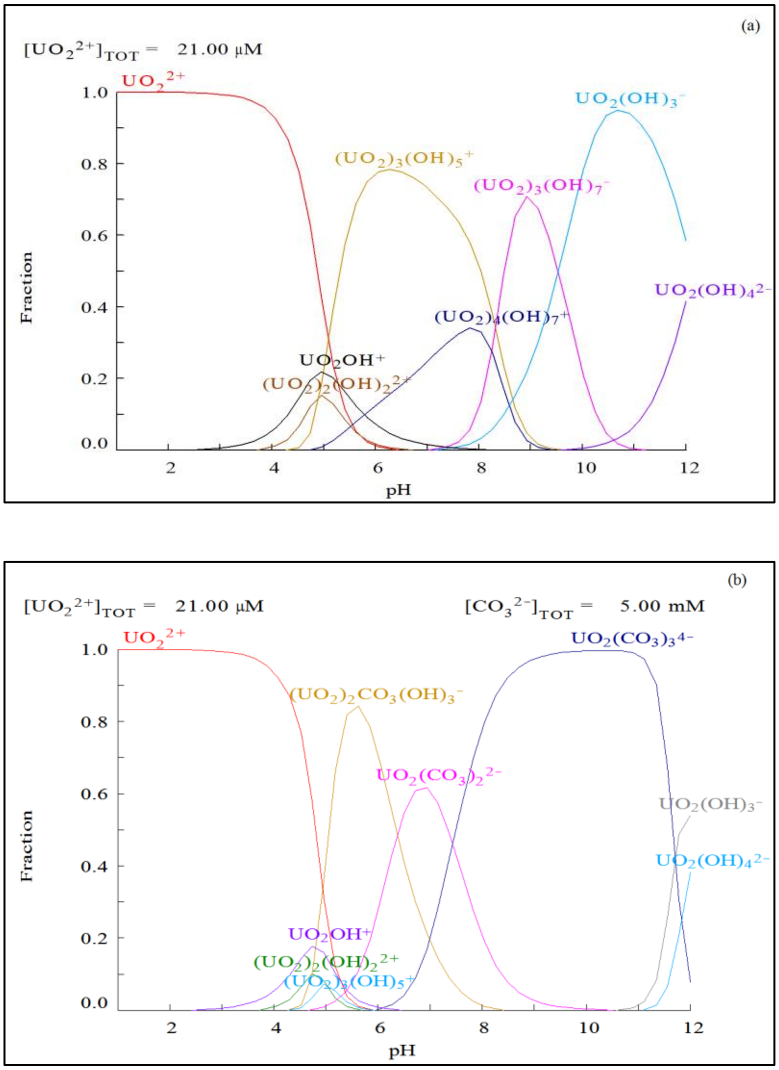

Fig. 3-5. U(VI) speciation as a function of solution pH calculated using the software MEDUSA: **(a)** in the absence of carbonate, and **(b)** in the presence of 5 mM CO_3^{2-}. (Initial U(VI) = 5 mg/L (21 µM), Temperature = 25 °C).

3.3.2. Resistance to oxygen oxidation and reactive lifetime

For immobilization of redox-active contaminants such as U(VI) in water or soil, the following features are desired: 1) the reactive material must offer strong reactivity to achieve the desired redox conversion, 2) it can provide prolonged reactive lifetime to facilitate maintaining an anoxic environment and preventing the reduced species from being re-oxidized, and 3) the reactivity loss due to side reactions (e.g., water corrosion) should be minimized. It is postulated that such apparently paradoxical criteria may be well balanced by a combination of two or more materials. For FeS@Fe^0, the less reactive FeS shell is expected to shield the highly reactive core Fe^0 from being consumed by side reactions (e.g., corrosion by water and oxygen), and the residual reactivity is expected to be long-lasting and can help inhibit re-oxidation of sequestered U. **Fig. 3-6a** compares the evolution of redox potential of Fe^0, FeS, and FeS@Fe^0-1/1 on the basis of equal Fe (50 mg/L) when the suspensions were exposed to air. The initial ORP value followed the sequence: Fe^0 (-587 mV) < FeS@Fe^0-1/1 (-338 mV) < FeS (-153 mV). Although Fe^0 showed the strongest initial reducing power, its redox potential diminished much faster than the other two materials. The ORP turned to positive after around 50 min for Fe^0, compared to 60 min for FeS and 90 min for FeS@Fe^0. In fact, the stronger reducing potential of Fe^0 lasted only for 30 min, and then FeS@Fe^0 became the most reactive material. It is well known that Fe^0 particles undergo rapid corrosion by DO (**Eqs. 3-13−14**) and water (**Eq. 3-15**) (He and Zhao 2008, Jin et al. 2018). In contrast, FeS does not undergo anoxic corrosion by water, thereby exhibiting a much slower corrosion rate (due to DO, **Eq. 3-16**) (Henderson and Demond 2013). FeS@Fe^0-1/1 took advantage of the merits of Fe^0 and FeS, resulting in much greater reactivity and longevity than either Fe^0 or FeS alone. At the end of the experiments (120 min), the redox potential sequence was changed to: FeS@Fe^0-1/1 (49 mV) < FeS (76 mV) < Fe^0 (172 mV).

$$Fe^0 + 2H_2O + O_2 \rightarrow 2Fe^{2+} + 4OH^- \qquad \textbf{(3-13)}$$

$$Fe^{2+} + 5/2H_2O + 1/4O_2 \rightarrow Fe(OH)_3\ (s) + 2H^+ \qquad \textbf{(3-14)}$$

$$Fe^0 + 2H_2O \rightarrow Fe^{2+} + H_2 + 2OH^- \qquad \textbf{(3-15)}$$

$$3FeS + 2O_2 \rightarrow 3S + Fe_3O_4 \qquad \textbf{(3-16)}$$

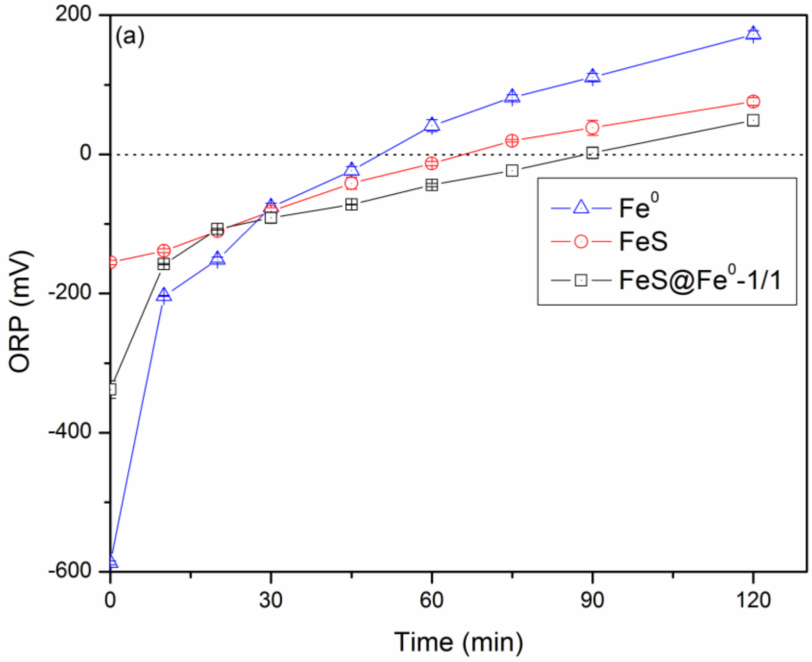

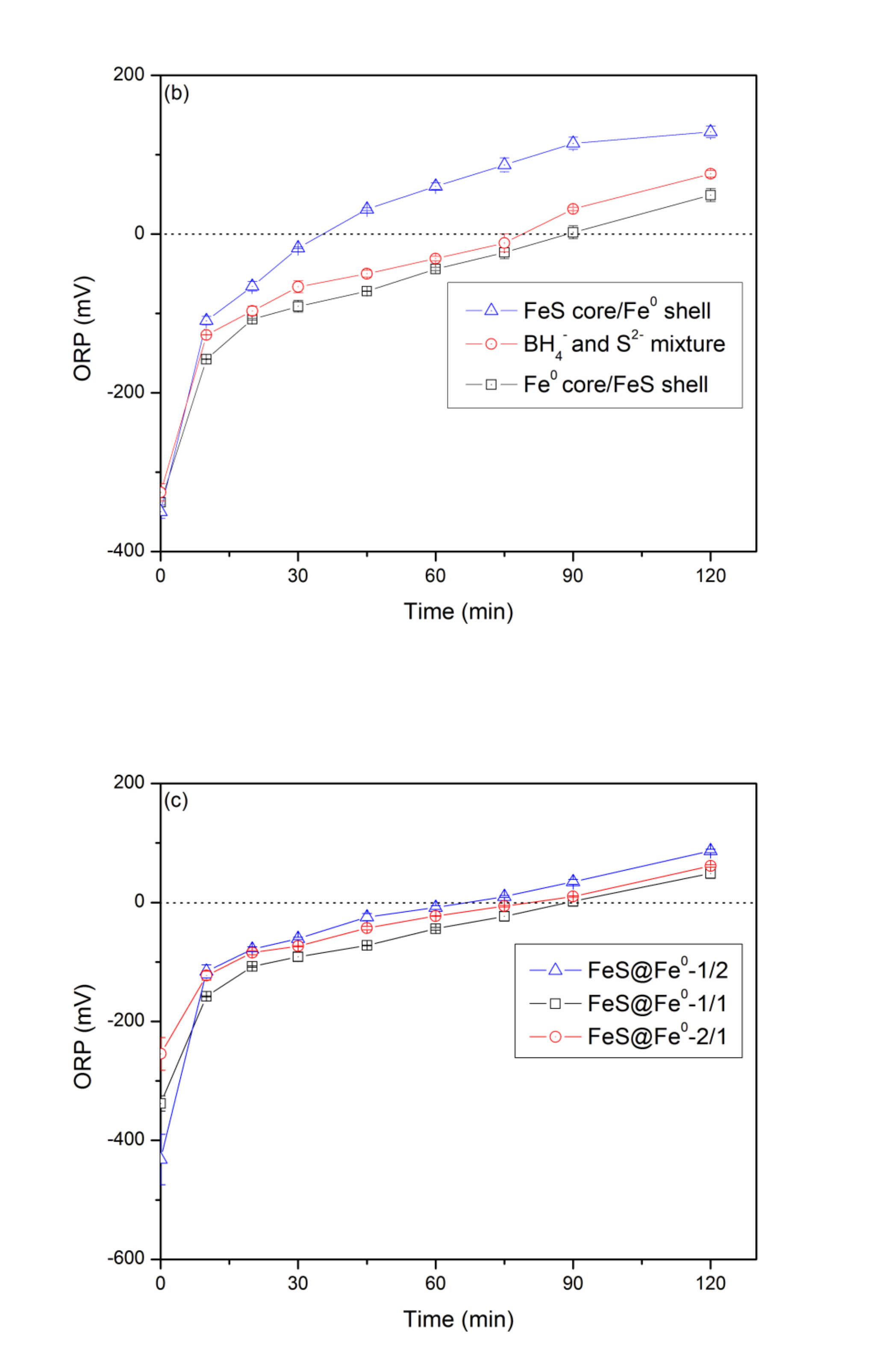

Fig. 3-6. Evolution of oxidation-reduction potential (ORP) of various reductants: (a)

FeS@Fe^0-1/1, Fe^0 and FeS, (b) FeS@Fe^0-1/1 prepared through different procedures ("BH_4^- and S^{2-} mixture" means BH^{4-} and S^{2-} were added at the same time; the Fe^0:FeS molar ratio was 1:1 in all cases), and (c) FeS@Fe^0-1/1 prepared at different Fe^0:FeS molar ratio. Material concentration = 50 mg/L as Fe in all cases.

Fig. 3-6b compares the ORP histories of FeS-Fe^0 binary particles prepared in three different ways: 1) FeS@Fe^0-1/1 as discussed above, i.e., Fe^0 core with FeS shell; 2) Fe^0@FeS-1/1, i.e., reverse the core-shell to give FeS core with Fe^0 shell (prepared by first precipitating 50% Fe^{2+} by S^{2-}, and then borohydride reduction of the remaining Fe^{2+}), and 3) Fe^0-FeS-1/1 without distinct core-shell structure (prepared by adding borohydride and S^{2-} at the same time). While the initial ORP values were comparable (-350 mV to -325 mV), the reversed core-shell structure lost its reduction power rapidly (zero ORP time = ~35 min), while FeS@Fe^0 displayed not only strongest reduction potential but longest reactive longevity (zero ORP time = ~90 min). It is noteworthy that the FeS-Fe^0 binary particles also showed much-improved reactivity (zero ORP time = ~80 min). In this case, the reduction of Fe^{2+} by BH_4^- occurred competitively with FeS precipitation, resulting in blended Fe^0-FeS binary phases. Evidently, such a mixed-phase structure can also well preserve the reducing activity of Fe^0, though not as good as the FeS@Fe^0 core-shell structure.

Fig. 3-6c compares performances of FeS@Fe^0 prepared at various Fe^0/FeS molar ratios. FeS@Fe^0-1/1 outperformed FeS@Fe^0-2/1 and FeS@Fe^0-1/2 in terms of both reduction potential and reductive lifetime. At an FeS/Fe^0 ratio of 1/2, the higher Fe^0 content gave the lower initial ORP (-432 mV), which, however, quickly rose up to zero at ~65 min. In contrast, at an FeS/Fe^0 of 2/1, the thicker FeS was able to extend the negative ORP till ~80 min. The results indicate that the core/shell molar ratio of 1/1 optimizes both reductive reactivity and longevity. In practice, the particles are expected to be used in the subsurface without significant exposure to oxygen. As such, the reductive lifetime is expected to be much longer than that in **Fig. 3-6**, which was obtained under vigorous aeration.

3.3.3. Reductive sequestration of U(VI)

Building upon the preliminary findings from the ORP measurements, reductive immobilization rates of U(VI) were examined through batch kinetic tests. **Fig. 3-7** compares the U(VI) removal rates by plain Fe^0, FeS, and $FeS@Fe^0$ prepared at various FeS/Fe^0 molar ratios. The retarded first-order model is applied to interpret the kinetic data (Lin et al. 2009):

$$-\frac{dC_t}{dt} = \frac{k_a}{1+\alpha t} C_t \text{ or } C_t = C_0 \cdot (1+\alpha t)^{-k_a/\alpha} \qquad \textbf{(3-17)}$$

where C_0 and C_t are U(VI) concentration (mg/L) at time 0 and t (min), respectively, k_a is the apparent rate constant (min^{-1}), which is analogous to the initial pseudo-first-order rate constant, and retardation factor α describes the decline of the reaction rate with time. **Fig. 3-7** shows that the model was able to adequately fit the entire kinetic data in all cases (R^2 = 0.994-1.000). For comparison, the conventional pseudo-first-order model was also tested, but the model failed to catch the data after the initial 2 min (**Table 3-1**).

Table 3-1. First-order and retarded first-order rate model parameters under various experimental conditions.

Particles	**Dosage (mg/L as Fe)**	**Experimental conditions**	**First-order model**		**Retarded first-order model**		
			k_1 **(min^{-1})**	R^2	k_a **(min^{-1})**	**α (min^{-1})**	R^2
FeS@Fe^0-1/1	35	pH 5.5	0.225	0.901	0.416	0.106	1.000
FeS@Fe^0-1/1	35	pH 6.5	0.376	0.919	1.025	0.615	0.999
FeS@Fe^0-1/1	35	pH 8.0	0.681	0.949	1.301	0.470	1.000
FeS@Fe^0-1/1	35	pH 9.0	0.808	0.889	2.348	1.155	1.000
FeS@Fe^0-1/1	50	pH 6.5, initial U(VI)=2 mg/L	1.207	1.000	1.902	0.299	1.000
FeS@Fe^0-1/1	50	pH 6.5, initial U(VI)=10 mg/L	0.476	0.935	0.969	0.318	1.000
FeS@Fe^0-1/1	50	pH 6.5, 1 mM HCO_3^-	0.592	0.891	1.733	1.193	1.000
FeS@Fe^0-1/1	50	pH 6.5, 5 mM HCO_3^-	0.322	0.926	0.731	0.435	1.000
FeS@Fe^0-1/1	50	pH 6.5, 5 mg/L HA as TOC	0.463	0.963	0.853	0.463	1.000
FeS@Fe^0-1/1	50	pH 6.5, 10 mg/L HA as TOC	0.325	0.990	0.584	0.545	0.994
FeS@Fe^0-1/1	50	pH 6.5, 1 mM Na^+	0.966	0.966	1.700	0.407	1.000
FeS@Fe^0-1/1	50	pH 6.5, 0.04 mM Cu^{2+}	0.789	0.969	1.441	0.483	1.000
FeS@Fe^0-1/1	50	pH 6.5, 1 mM Ca^{2+}	0.351	0.874	1.188	0.895	0.999
FeS@Fe^0-1/1	50	pH 6.5, particles aged 1 day	0.969	0.961	1.784	0.457	1.000
FeS@Fe^0-1/1	50	pH 6.5, particles aged 2 days	0.965	0.967	1.743	0.432	1.000
FeS@Fe^0-1/1	50	pH 6.5, particles aged 7 days	0.070	0.971	0.172	0.161	0.989
FeS@Fe^0-1/1	50	pH 6.5, particles aged 21 days	0.009	0.507	0.070	1.051	0.975
Fe^0	50	pH 6.5, particles aged 1 day	0.632	0.952	1.363	0.706	1.000
Fe^0	50	pH 6.5, particles aged 2 days	0.367	0.837	1.116	0.724	1.000
Fe^0	50	pH 6.5, particles aged 7 days	0.025	0.857	0.071	0.730	0.988
Fe^0	50	pH 6.5, particles aged 21 days	0.001	0.934	0.006	0.195	0.975

Table 3-2 gives the best-fitted model parameters. The k_a values of FeS@Fe^0-1/2 and FeS@Fe^0-1/1 were 1.640 and 1.805 min^{-1}, respectively, which are 1.19 and 1.31 times higher than that of Fe^0 (1.375 min^{-1}), which again indicates the important role of the FeS shell in preserving the reactivity of the core Fe^0. This is of practical significance as the cost of synthetic Fe^0 is over 35 times higher than that of FeS. Increasing the FeS/Fe^0 ratio to 2/1 resulted in a much lower k_a of 0.858 min^{-1}, indicating the key role of the core Fe^0 as the electron source. FeS alone showed a much slower removal rate (0.280 min^{-1}) (**Fig. 3-7**), which is related to the much lower ORP value of FeS (-153 mV) than that of Fe^0 (-587 mV) (**Fig. 3-6a**).

The promoting role of FeS in FeS@Fe^0 can be ascribed to following reasons: 1) the FeS coating can effectively inhibit water corrosion of the core Fe^0 by poisoning the hydrogen recombination, which favors the reduction by atomic hydrogen, and thus enhances the selectivity of Fe^0 towards target contaminants (Fan et al. 2017, Han and Yan 2016); and 2) the FeS coating facilitates the electron transfer from the Fe^0 core to the acceptor U(VI) cations owing to the higher electronegativity of FeS and good electron conductivity (Li et al. 2016). However, excessive FeS coating would block the electron transfer from the core Fe^0 (Li et al. 2017); and at a given total Fe mass, an elevated FeS:Fe^0 ratio results in decreased electron source (Fe^0).

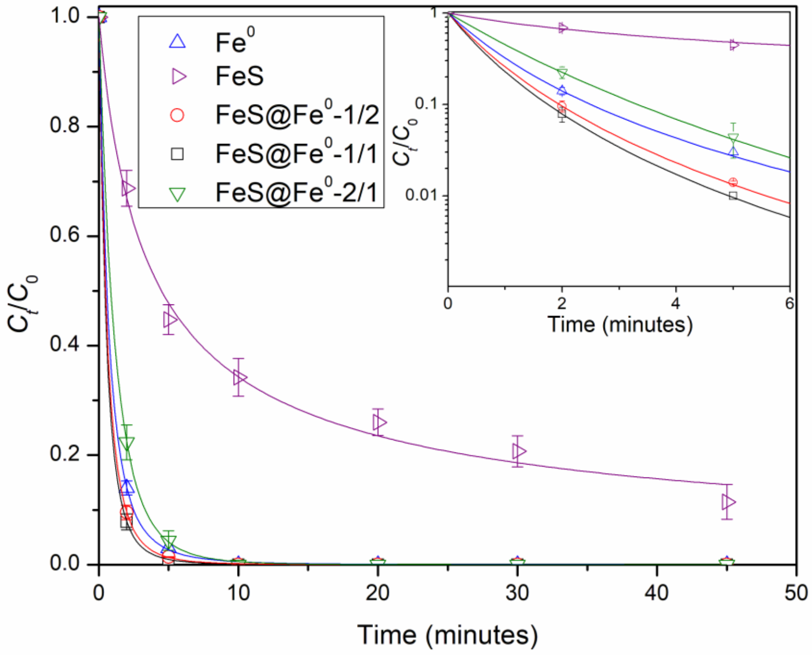

Fig. 3-7. U(VI) removal rates by ZVI (Fe^0), FeS, and FeS@Fe^0 prepared at various Fe^0/FeS molar ratios. Experimental conditions: initial U(VI) = 5 mg/L, particles dosage = 50 mg/L as Fe, MeS buffer = 10 mM, pH = 6.5 ± 0.1, and temperature = 22 ± 1 °C. Symbols: experimental data; Lines: retarded first-order model fittings. The inset shows the initial removal rates.

Table 3-2. Best-fitted parameters of the retarded first-order kinetic model.

Materials	**Retarded first-order model**		
	k_a (min^{-1})	**α (min^{-1})**	**R^2**
Fe^0	1.375	0.449	1.000
FeS	0.280	0.444	0.994
FeS@Fe^0-1/2	1.640	0.444	1.000
FeS@Fe^0-1/1	1.805	0.469	1.000
FeS@Fe^0-2/1	0.858	0.154	1.000

3.3.4. Effects of water chemistry on U(VI) removal

3.3.4.1. Effect of pH

Solution pH can affect iron corrosion rate, electron conductivity, and reactivity of FeS, and U speciation, thereby affecting the U(VI) reduction and removal. Plain ZVI is very sensitive to solution pH and is more reactive under acidic conditions due to hydrogen reduction and the passivation effect at alkaline pH (Xiong et al. 2009). The FeS coating in FeS@Fe^0 is expected to enhance electron transfer and mitigate the passivation effect (Dong et al. 2018, Han and Yan 2016). **Fig. 3-8** shows that FeS@Fe^0-1/1 was able to highly effectively remove U(VI) throughout the pH range of 5.5-9.0. Again, the retarded first-order model was able to adequately fit the rate data in all cases (R^2 = 0.999-1.000) (**Table 3-1**). Increasing pH from 5.5 to 9.0 modestly, but progressively, increased the k_a value from 0.416 to 2.348 min^{-1}. The presence of the FeS coating greatly buffered the pH sensitivity of the ZVI core. FeS@Fe^0-1/1 appears much less sensitive to pH than the dithionite-sulfidated ZVI reported by Dong et al. (Dong et al. 2018), though the trend of pH effect appears similar. The elevated removal rate of U(VI) with increasing pH could be attributed to two factors. First, at higher pH, the FeS surface is more deprotonated and the deprotonated ligands (i.e., $\equiv FeO^-$ and $\equiv S^-$) are more favorable for electron donation (Kim et al. 2013). This was supported by a cyclic voltammetry study conducted with iron sulfides (FeS_2 and $Fe_{1-x}S$), where the peak currents increased with increasing pH (Conway et al. 1980). Second, more FeS was dissolved at more acidic pH. At the end of the reaction, the soluble iron concentration was measured to be 21.4%, 13.8%, 9.6%, and 2.7% at pH 5.5, 6.5, 8.0, and 9.0, respectively, resulting in partial loss of the reactive sites (Gong et al. 2014) and the protective role of the FeS shell.

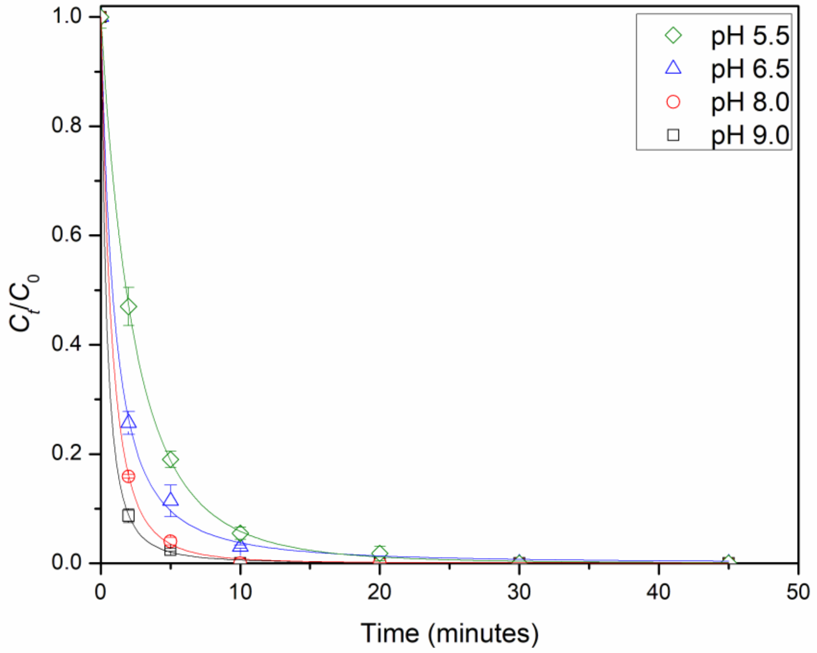

Fig. 3-8. Effects of pH on removal of U(VI) by FeS@Fe^0-1/1 at a dosage of 35 mg/L as Fe. Experimental conditions: initial U(VI) = 5 mg/L, MeS buffer = 10 mM, Tris buffer = 10 mM, pH = 5.5−9.0. Symbols: experimental data; Lines: retarded first-order model fittings.

3.3.4.2. Effect of common water ligands

Fig. 3-9 presents the effects of bicarbonate and humic acid (HA) on U(VI) removal by FeS@Fe^0-1/1. In the presence of 1 mM HCO_3^-, the k_a was only slightly decreased from 1.805 to 1.733 min^{-1}. The removal remained strong when the HCO_3^- concentration was raised to 5 mM (k_a = 0.731 min^{-1}) (**Fig. 3-9a and Table 3-1**). Likewise, nearly complete U(VI) removal was achieved within 45 min in the presence of 5 mg/L of HA as TOC, though the k_a was lowered by a factor of 2.12 (to 0.853 min^{-1}). In the more extreme case, when the HA concentration as elevated to 10 mg/L as TOC, >98% U(VI) removal was still achieved within 45 min (k_a = 0.584 min^{-1}) (**Fig. 3-9b and Table 3-1**).

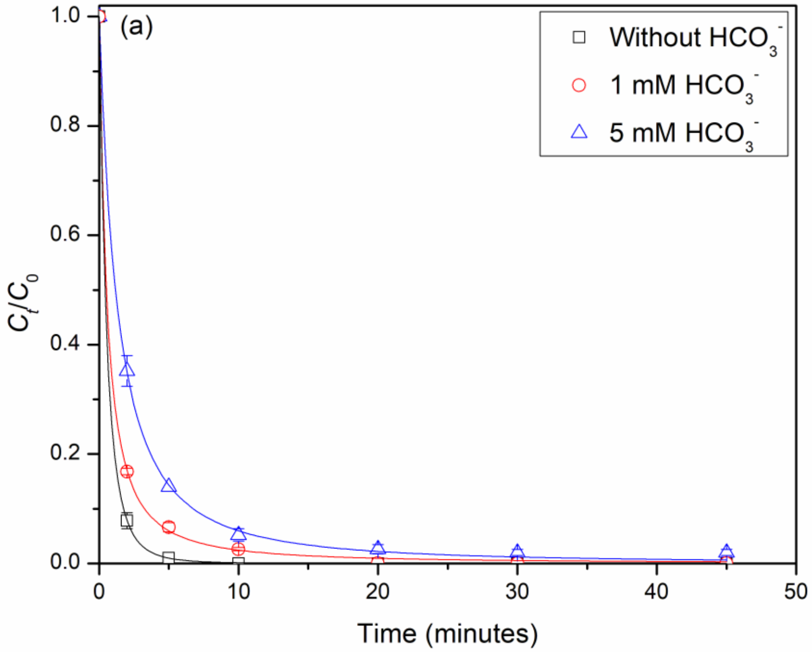

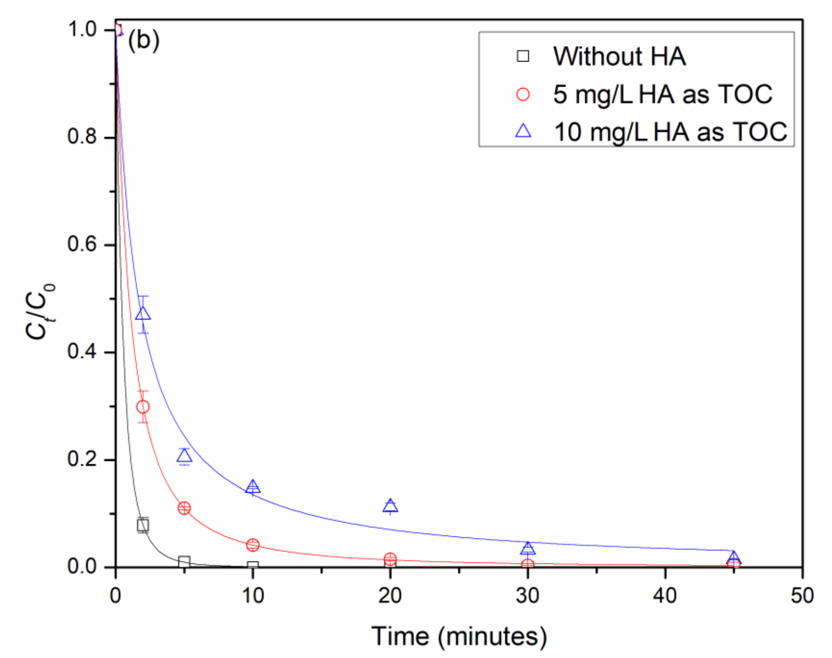

Fig. 3-9. Effects of (a) bicarbonate, and (b) humic acid on removal of U(VI) by FeS@Fe^0-1/1. Experimental conditions: particles dosage = 50 mg/L as Fe, initial U(VI) = 5 mg/L, MeS buffer = 10 mM, pH = 6.5 ± 0.1, bicarbonate = 1-5 mM, humic acid = 5-10 mg/L as TOC. Symbols: experimental data; Lines: retarded first-order model fittings.

Bicarbonate can complex with various U(VI) species, and thus affect interactions between FeS@Fe^0 and U(VI). **Fig. 3-5** shows U(VI) speciation in the absence or presence of carbonate as a function of pH. At alkaline pH, CO_3^{2-}/HCO_3^- can complex with UO_2^{2+} to form stable complexes, such as $UO_2(CO_3)_3^{4-}$, $UO_2(CO_3)_2^{2-}$, and $(UO_2)_2CO_3(OH)_3^-$ (**Fig. 3-5b**). These anionic uranyl complexes will hinder their adsorption onto the negatively charged FeS@Fe^0-1/1 (**Fig. 3-4–3-5**) due to electrostatic repulsion (Li et al. 2018). In addition, dissolved carbonate species can accelerate the corrosion of Fe^0, whereas elevated precipitation of $FeCO_3$ may passivate the reactive sites (Agrawal et al. 2002). Evidently, the FeS coating in FeS@Fe^0-1/1 remarkably mitigated the inhibitive effect of bicarbonate, which is more impeding for bare ZVI.

HA can pose several contrasting effects on U(VI) uptake by FeS@Fe^0-1/1. First, HA can complex with U(VI) to form binary UO_2HA(II) and ternary UO_2(OH)HA(I) complexes, thereby enhancing U(VI) solubility and reducing U(VI) adsorption (Křepelová et al. 2006). Second, HA can be adsorbed by FeS or Fe^0 (Giasuddin et al. 2007), which diminishes the accessibility of reactive sites and impedes the electron transfer. Third, immobilized HA on the FeS@Fe^0 surface may provide additional sorption sites for U(VI) *via* surface complexation, facilitating U(VI) sorption. While HA or DOM has been known to inhibit the reactivity of plain ZVI particles (Xie and Shang 2007), the inhibition effect on FeS@Fe^0 was much alleviated due to the FeS coating.

3.3.4.3. Effects of coexisting cations

Fig. 3-10 shows the effect of coexistent Na^+, Ca^{2+}, and Cu^{2+} on the removal of U(VI) by FeS@Fe^0. The effect of Na^+ (1 mM) was statistically insignificant ($p = 0.211$) with a k_a value of 1.701 min^{-1} (**Table 3-1**). Likewise, the effect of 0.04 mM of Cu^{2+} (the maximal solubility at pH 6.5) was also insignificant ($p < 0.101$) ($k_a = 1.441$ min^{-1}). The presence of 1 mM of Ca^{2+} caused a tailing in the kinetic profile ($k_a = 1.188$ min^{-1}), though nearly complete U(VI) removal was still achieved in 45 min. At the experimental pH (6.5), U(VI) is present as various cationic species (**Fig. 3-4a**). As such, the co-existing cations may compete for the adsorption sites. Since bivalent cations are more favorably adsorbed, Cu^{2+} and Ca^{2+} showed more effect than Na^+ (note the less notable effect Cu^{2+} was due to its much lower concentration). Moreover, Ca^{2+} can form calcium uranyl carbonate complexes according to **Eqs.** (**3-18**) and (**3-19**), and FeS@Fe^0-1/1 particles are unfavorable for these anionic and electron neutral complexes (Yin et al. 2018, Liu et al. 2016).

$$UO_2^{2+} + Ca^{2+} + 3CO_3^{2-} = CaUO_2(CO_3)_3^{2-} \qquad \textbf{(3-18)}$$

$$UO_2^{2+} + 2Ca^{2+} + 3CO_3^{2-} = CaUO_2(CO_3)_3\ (aq) \qquad \textbf{(3-19)}$$

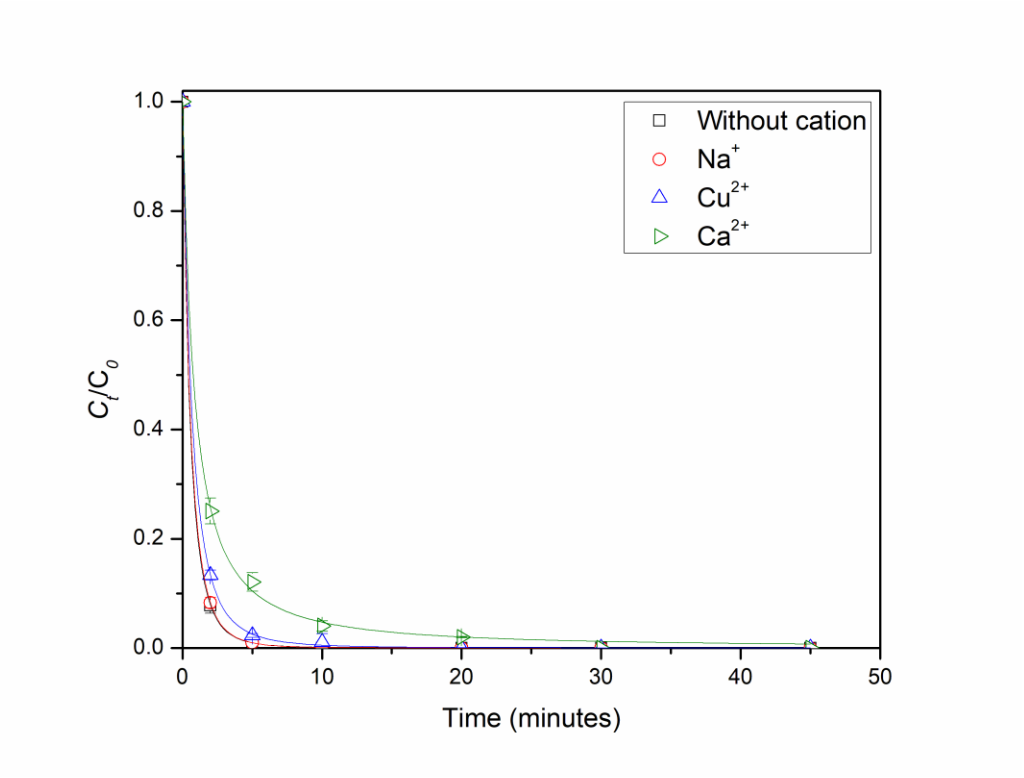

Fig. 3-10. Effects of coexisting cations on the removal of U(VI) by FeS@Fe^0-1/1. Experimental conditions: particle dosage = 50 mg/L as Fe, initial U(VI) = 5 mg/L, MeS buffer = 10 mM, pH = 6.5 ± 0.1, Na^+ = Ca^{2+} = 1 mM, Cu^{2+} = 0.04 mM. Symbols: experimental data; Lines: retarded first-order model fittings.

3.3.5. Effect of material aging

As stated earlier, the key purpose to modify the core ZVI was to preserve the reactivity and to extend the reactive lifetime by shielding the core from the background corrosions. **Fig. 3-11** compares the effects of aging time (i.e., particle storage time in aqueous solution) on the U(VI) removal rate by FeS@Fe^0-1/1 and Fe^0. It was evident that water corrosion has almost no distinctive effect on the U(VI) removal by FeS@Fe^0-1/1 after 2 days of aging, where k_a still kept at 1.743 min^{-1} (nearly the same as that of fresh FeS@Fe^0-1/1) (**Fig. 3-11a and Table 3-1**). In contrast, the 2-day aging reduced the k_a value for bare Fe^0 to 1.116 min^{-1} (by a factor of 1.23) (**Fig. 3-11b and Table 3-1**). The difference became even more distinctive as the aging time was extended. After 7 days of aging, the k_a value for FeS@Fe^0-1/1 was lessened by 10.49 times, but 19.37 times for plain Fe^0; and the 45-minute U(VI) removal reached 93.7% by FeS@Fe^0-1/1, but only 27.3% for the Fe^0 particles. While the Fe^0 particles were almost exhausted after 21 days of aging (with only 6.4% of U(VI) removed), FeS@Fe^0-1/1 still removed 25.3% of U(VI). The results are in line with those by Fan et al. (Fan et al. 2016), who reported that sulfidation at S/Fe molar ratios ≥ 0.3 can effectively suppress the reaction with water, and preserve the reducing power towards TCE. Dong et al. (Dong et al. 2018) found that the aging of S-nZVI for 10 and 20 days only decreased the dechlorination efficiency of TCE by 1.04 and 1.13 times, respectively, and they claimed that the FeS coating was able to alleviate the surface passivation of Fe^0. Nonetheless, extensive exposure to water or DO should be avoided in practical applications to make the most use of the reactivity of FeS@Fe^0.

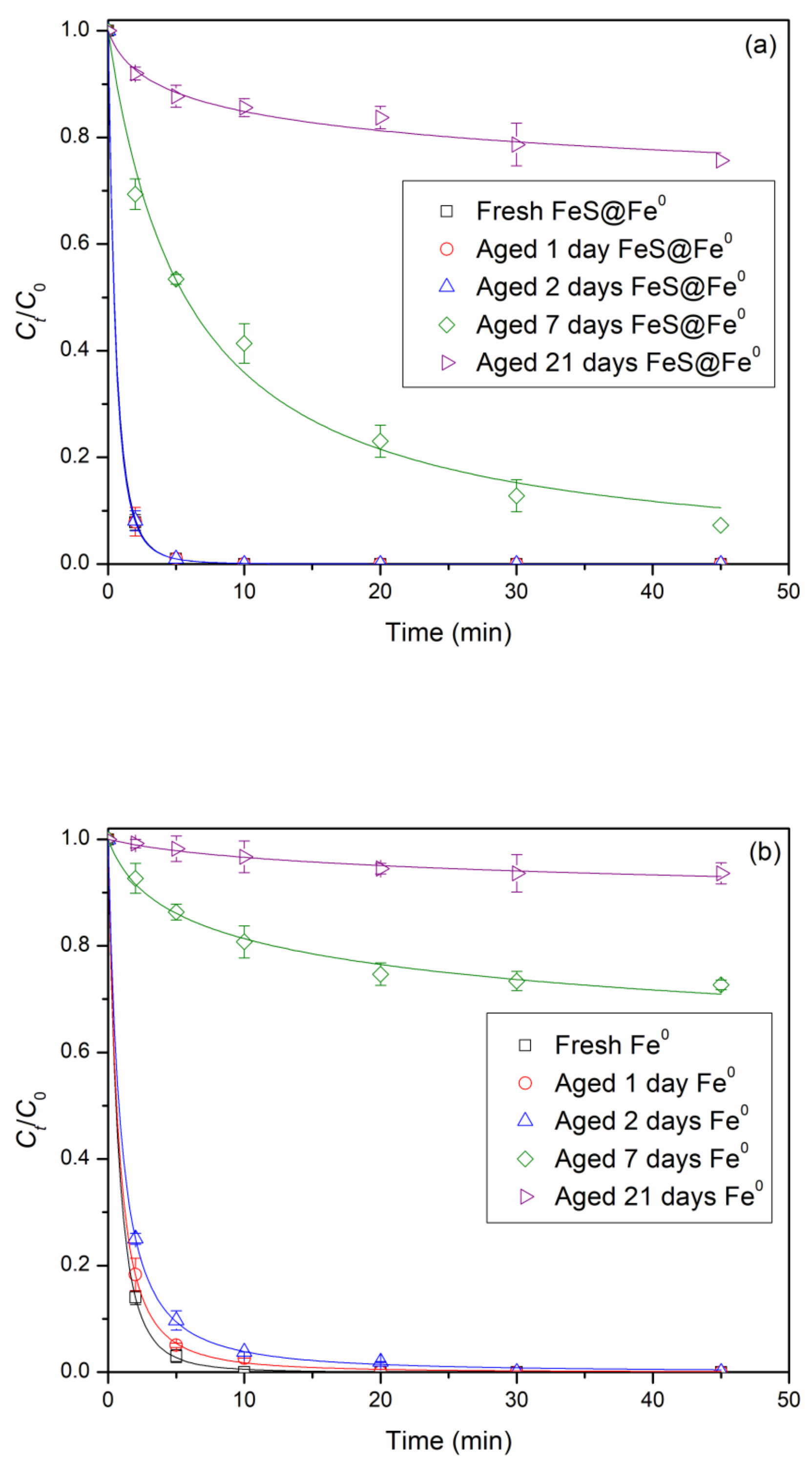

Fig. 3-11. Effects of material aging on the removal of U(VI) by: (a) FeS@Fe^0-1/1, and (b)

Fe^0. Experimental conditions: particles dosage = 50 mg/L as Fe, initial U(VI) = 5 mg/L, MeS buffer = 10 mM, pH = 6.5 ± 0.1. Symbols: experimental data; Lines: retarded first-order model fittings.

3.3.6. Mechanism for U(VI) removal by FeS@Fe^0

To gain deeper insight into the underlying mechanism for U(VI) removal, FeS@Fe^0-1/1 before and after the reaction with U(VI) at pH 6.5 was further characterized by XRD, FTIR, and XPS analyses. The XRD patterns in **Fig. 3-1** shows that upon U loading, two new weak peaks appeared at around 28.5° and 58.1°, corresponding to phases (111) and (222) of uraninite (UO_2), respectively (Valdivieso et al. 2001). The XRD results provide direct evidence on the reductive conversion of soluble U(VI) into UO_2 precipitates.

Fig. 3-12 shows the FTIR spectra of FeS@Fe^0-1/1 before and after the reaction. In both cases, the peaks at 2160, 2020, and 1980 cm^{-1} are ascribed to the stretching vibrations of B−H bonds (Yang et al. 2015), which resulted from the reaction with borohydride. The peaks at 1360 cm^{-1} and 1320 cm^{-1} are assigned to S=O vibrations from sulfate (Abdulhamid et al. 2006), and the enhanced peak intensity upon reacting with uranium indicates an increase of sulfate content. The peaks between 622 and 465 cm^{-1} are assigned to stretching vibrations of typical Fe−S and Fe−O bonds (Du et al. 2016, Dong et al. 2018), resulting from iron sulfides and iron oxides. Upon reaction of with U(VI), a new peak at 822 cm^{-1} was observed, which is ascribed to the O=U=O bond vibration from uranyl (UO_2^{2+}) (Gorman-Lewis et al. 2008), suggesting direct adsorption of UO_2^{2+} *via* ion pairing (**Eqs. 3-20−22**) (Li et al. 2015, Hyun et al. 2012),

$$\equiv Fe^+ + H_2O \leftrightarrow \equiv FeOH + H^+ \qquad \textbf{(3-20)}$$

$$UO_2^{2+} + 2(\equiv FeOH) \leftrightarrow (\equiv FeO)_2UO_2 + 2H^+ \quad \textbf{(3-21)}$$

$$UO_2^{2+} + \equiv FeS \leftrightarrow \equiv S^{2-}\text{-}UO_2^{2+} + Fe^{2+} \quad \textbf{(3-22)}$$

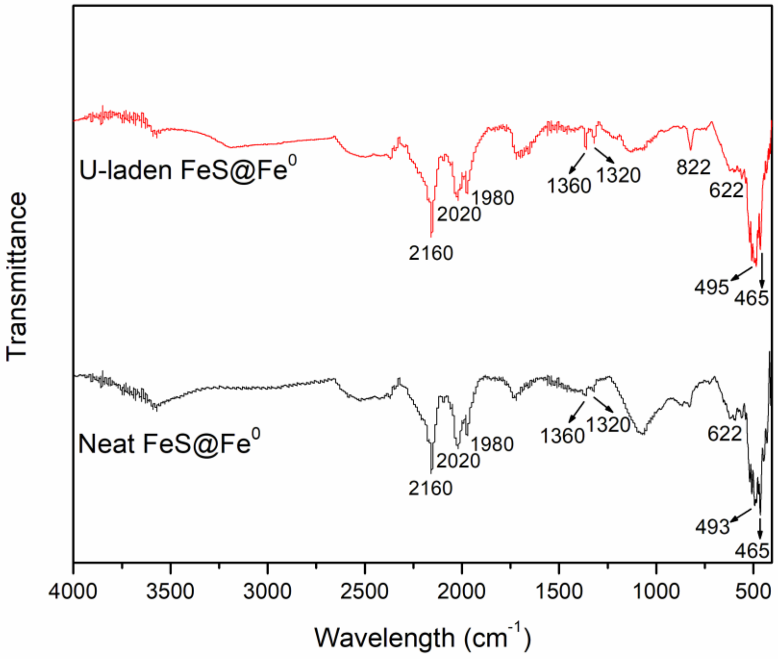

Fig. 3-12. FTIR spectra of Neat and U-laden FeS@Fe^0-1/1.

The surface elemental compositions and oxidation states of neat and U-loaded FeS@Fe^0-1/1 were characterized by XPS (**Fig. 3-13**). The survey XPS spectra (**Fig. 10a**) indicate that the surface elements of neat FeS@Fe^0-1/1 include O (61.6%), S (20.4%), and Fe (18.0%). Upon reaction with U(VI), the elemental compositions were changed to O (68.9%), S (19.1%), Fe (9.8%), and U (2.3%). The remarkable decrease in Fe and rise in O are in line with the direct UO_2^{2+} adsorption mechanism (**Eqs. 3-20−22**). For neat FeS@Fe^0-1/1, the peaks at 707.5, 710.5, and 713.4 eV in the high-resolution spectra of Fe 2p (**Fig. 10b)** represent Fe^0 (Gong et al. 2015), Fe(II)-S (Hua and Deng 2008, Hu et al.

2017b), and Fe(III)-O (Jin et al. 2018, Thomas et al. 1998), respectively. After reaction with U(VI), the surface Fe^0 decreased from 12.7% for virgin $FeS@Fe^0$-1/1 to 9.5%, Fe(II) in Fe(II)-S decreased from 73.5% to 49.9%, and Fe(III) increased from 13.8% to 40.6%. The changes in Fe oxidation states indicate that both Fe^0 and Fe(II) may act as electron donors in the reduction of U(VI) by ZVI, as illustrated by **Eqs.** (**3-23**) and (**3-24**) (Li et al. 2015):

$$\equiv UO_2^{2+} + Fe^0 \rightarrow UO_2(s) + Fe^{2+} \quad \mathbf{(3\text{-}23)}$$

$$\equiv UO_2^{2+} + 2Fe(II)_{\text{Sorbed or Structural}} + 2H_2O \rightarrow UO_2(s) + 2Fe(III) + 4OH^- \quad \mathbf{(3\text{-}24)}$$

Fe(II) ions at the solid-solution interface are often classified as sorbed Fe(II) and structural Fe(II) ions. Charlet et al. (Charlet et al. 1998) reported that reduction of UVI) by ZVI was coupled with oxidation of Fe(II) ions sorbed on iron corrosion products such as hematite, with Fe^0 serving as the source of Fe(II). The assertion was evidenced by the equilibrium E_h values measured during U immobilization reaction with ZVI. Moreover, the researchers observed that the U(VI) reduction rate was proportional to the sorbed concentrations of Fe(II) and U(VI). Kang et al. (Kang et al. 2011) reported that electron transfer mediated by surface-associated Fe(II) ions was responsible for the reduction of aqueous Se(IV) by pyrite. And Huo et al. (Huo et al. 2017) reported that sorbed Fe(II) ions played a key role in reductive immobilization of pertechnetate using synthetic pyrite nanoparticles. Based on these findings and given the observed much lower reactivity of plain FeS (**Fig. 3-**), we can deduce that Fe(II) ions, which were mainly released from the Fe^0 core but sorbed at the FeS-Fe_nO_m-Solution interfaces, played an important role in the rapid reductive removal of U(VI).

In addition, structural Fe(II) in iron corrosion products may also reduce U(VI). For instance, Magnetite is a corrosion product on Fe^0 and it can rapidly adsorb uranyl ions and gradually reduce U(VI) to U(IV), coupled with oxidation of magnetite into maghemite (Scott et al. 2005), which are consistent with our XPS data. White and Peterson [74] pointed out that the half-cell potential for the solid-state oxidation of Fe(II)→Fe(III) ranges from -0.34 to -0.65 V, indicating that in the solid-state Fe(II) is a stronger reducing agent than the aqueous Fe(II) (-0.77 V). For our case, however, the role of structural F(II) ions is likely to be kinetically limited because of the core-shell structure, which may hinder the accessibility of the octahedral sites.

While **Fig. 3-7** revealed a much weaker reactivity of plain FeS than FeS@Fe^0, the role of S in FeS@Fe^0 is yet to be explored. **Fig. 3-13c** shows high-resolution spectra in the vicinity of S 2p of neat and U-laden FeS@Fe^0-1/1. For the neat particles, the peaks centered at 161.4, 162.5, 163.3, 166.7, and 168.7 eV are ascribed to S in the form of FeS, FeS_2, S_n^{2-}, SO_3^{2-}, and surface-bound SO_4^{2-}, respectively (Du et al. 2016, Song et al. 2017, Thomas et al. 1998). After reaction with U(VI), FeS decreased from 29.3% to 16.9%, and FeS_2 from 31.2% to 26.5%, indicating the consumption of S^{2-} and S_2^{2-} during U(VI) oxidation. In the meantime, S_n^{2-} increased from 27.7% to 34.0%, SO_3^{2-} from 1.3% to 2.8%, and SO_4^{2-} from 10.5% to 19.8%, suggesting that S^{2-} and S_2^{2-} in FeS and FeS_2 were partially oxidized during reduction of U(VI). Previous researches have proposed the following redox reactions facilitated by S^{2-} or S_2^{2-} (**Eqs. 3-25‒31**) (Gong et al. 2017, Scott et al. 2007).

$$FeS\ (s) + H^+ \leftrightarrow Fe^{2+} + HS^- \qquad \textbf{(3-25)}$$

$$4UO_2^{2+} + HS^- + 4H_2O \rightarrow 4UO_2(s) + SO_4^{2-} + 9H^+ \qquad \textbf{(3-26)}$$

$$3UO_2^{2+} + HS^- + 3H_2O \rightarrow 3UO_2(s) + SO_3^{2-} + 7H^+ \quad \textbf{(3-27)}$$

$$(n\text{-}1)UO_2^{2+} + nHS^- \rightarrow (n\text{-}1)UO_2\ (s) + S_n^{2-} + nH^+ \quad \textbf{(3-28)}$$

$$15{\equiv}UO_2^{2+} + 2FeS_2 + 16H_2O \rightarrow 15UO_2\ (s) + 2Fe^{3+} + 4SO_4^{2-} + 32H^+ \quad \textbf{(3-29)}$$

$$11{\equiv}UO_2^{2+} + 2FeS_2 + 12H_2O \rightarrow 11UO_2\ (s) + 2Fe^{3+} + 4SO_3^{2-} + 24H^+ \quad \textbf{(3-30)}$$

$$(3n\text{-}4)UO_2^{2+} + 2nFeS_2 \rightarrow (3n\text{-}4)UO_2\ (s) + 2nFe^{3+} + 4S_n^{2-} \quad \textbf{(3-31)}$$

Fig. 3-13d shows the high-resolution spectra of U 4f on FeS@Fe^0-1/1. Deconvolution of the U $4f_{7/2}$ peak revealed the existence of both U(IV) (55.1%, 380.7 eV) and U(VI) (44.9%, 382.1 eV) (Cai et al. 2017, Shao et al. 2015). This result is comparable to the uranium extraction data, where 41.7% of U(VI) was extractable while 58.3% of U(VI) was reduced, indicating both adsorption and reduction are operative.

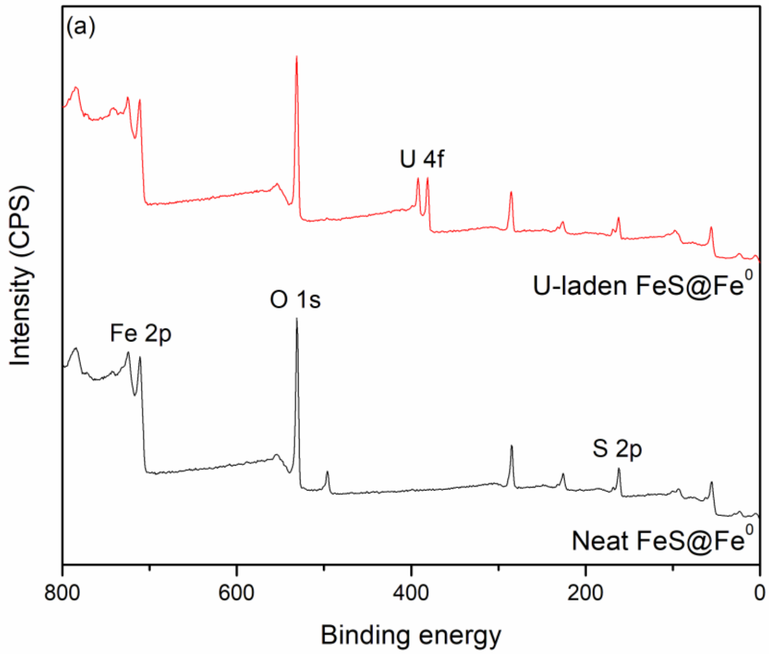

(a)
Intensity (CPS)
U 4f
U-laden FeS@Fe^0
O 1s
Fe 2p
S 2p
Neat FeS@Fe^0
800
600
400
200
0
Binding energy

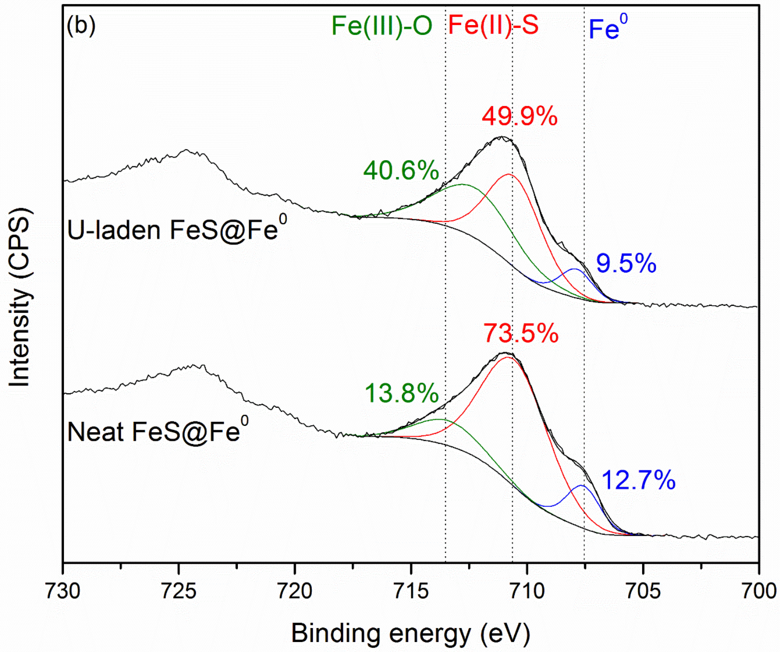

(b)
Fe(III)-O
Fe(II)-S
Fe^0
49.9%
40.6%
9.5%
U-laden FeS@Fe^0
73.5%
13.8%
12.7%
Neat FeS@Fe^0
Intensity (CPS)
730
725
720
715
710
705
700
Binding energy (eV)

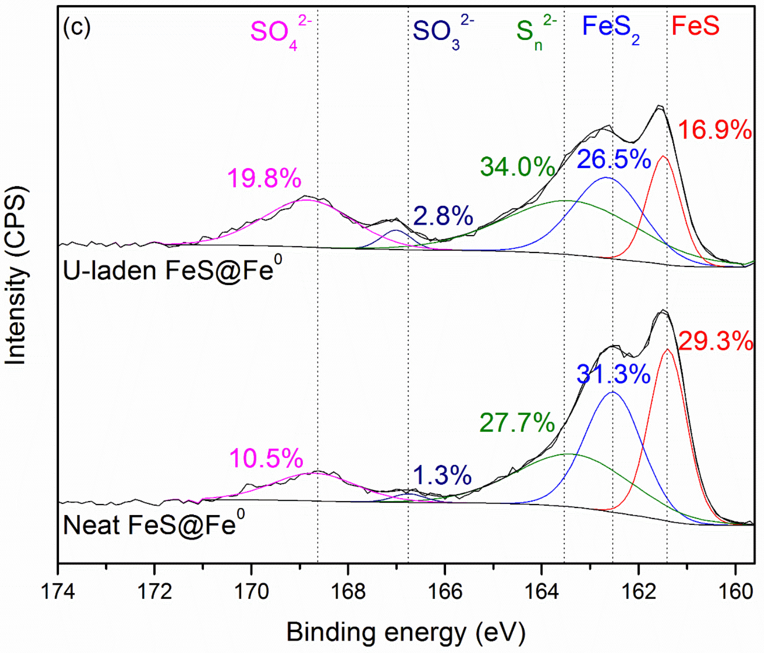

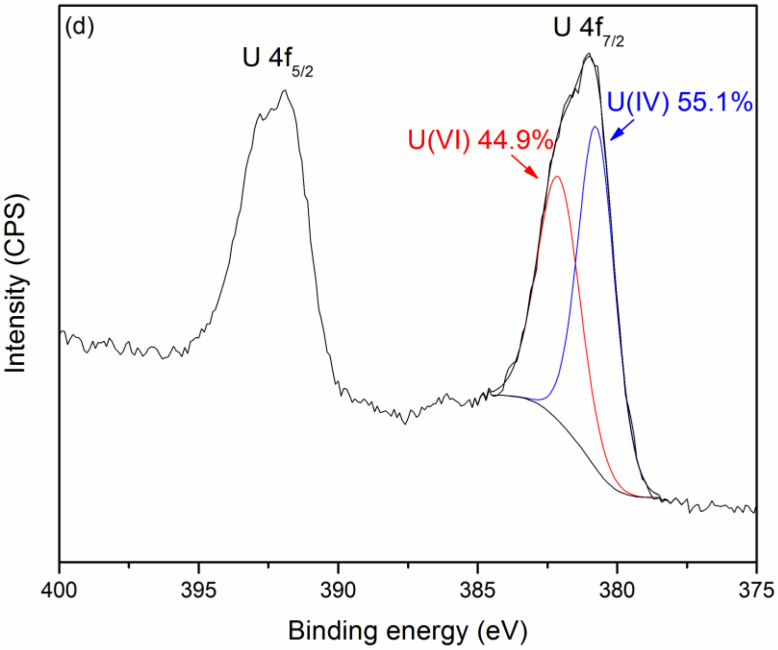

Fig. 3-13. XPS spectra of FeS@Fe^0-1/1 before and after reaction with U(VI): (a) survey

XPS, (b) high resolution of Fe 2p, (c) high resolution of S 2p, and (d) high resolution of U 4f.

Based on the XRD, FTIR and XPS characterizations, along with the rapid removal U(VI) removal kinetics, **Fig. 3-14** presents a conceptualized representation of the U(VI) removal mechanism by FeS@Fe^0. First, U(VI) ions are rapidly adsorbed onto the surface of the particles *via* electrostatic attraction and/or surface complexation; and subsequently, the sorbed U(VI) ions are reduced by Fe^0, FeS, and FeS$_2$ to U(IV), resulting in precipitation of UO$_{2(s)}$ and formation of Fe(II), Fe(III), S$_n^{2-}$, SO$_3^{2-}$ and SO$_4^{2-}$. The primary electron donors include Fe^0 and sorbed Fe^{2+} and structural Fe^{2+}, with Fe^0 being the key source of electrons and Fe^{2+}, whereas S^{2-} and S$_2^{2-}$ also contributed to the reduction process.

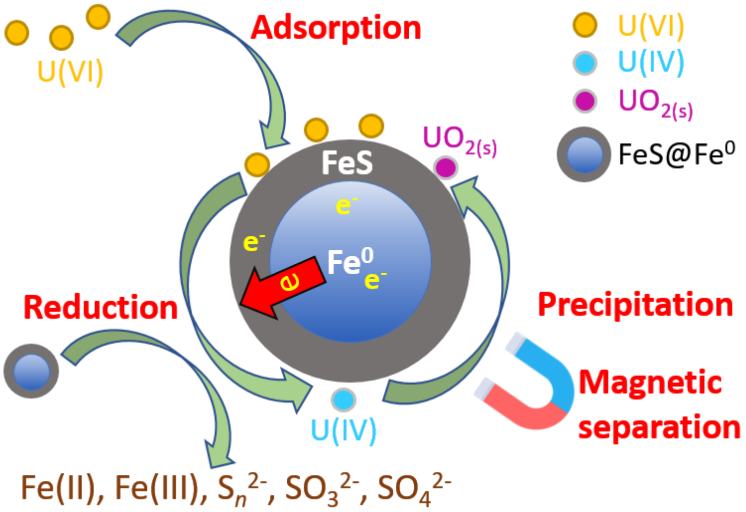

Fig. 3-14. Schematic representation of the reaction mechanism for U(VI) removal by FeS@Fe^0.

3.4. Conclusions

This study prepared and tested a new type of FeS-coated Fe^0 particles, and tested the material for reductive immobilization U(VI) in aqueous solution under various water chemistry conditions. The key findings are recapped as follows:

1) A new type of FeS-coated Fe^0 particles was prepared by coating the core Fe^0 with *in situ* formed FeS through a facile one-pot, two-step (reduction-precipitation) approach. Compared to conventional ZVI or sulfidated ZVI prepared by other methods, the method is not only easier to operate but facilitates control of the S/Fe molar ratio and the core-shell structure. XRD, STEM, XEDS, and PPMS characterizations confirmed the compositions, core-shell structure, and magnetic properties.
2) The FeS coating was able to facilitate the preservation of the reactivity of the core Fe^0 by preventing it from corrosion by water or DO, and thus alleviating the surface passivation of Fe^0. FeS@Fe^0-1/1 with an Fe^0/FeS molar ratio of 1:1 exhibited the highest reductive reactivity and reactivity longevity.
3) The retarded first-order kinetic model adequately fit the kinetic data of U(VI) removal.
4) FeS@Fe^0-1/1 can highly effectively remove U(VI) in the broad pH range (5.5-9.0) and in the presence of high concentrations of bicarbonate (1-5 mM) and HA (5-10 mg/L as TOC). Higher pH was found more favorable for the reaction, while elevated HA and bicarbonate concentrations were more inhibitive to the reaction.
5) Both adsorption and reductive conversion of UO_2^{2+} to $UO_{2(s)}$ were responsible for U(VI) removal by FeS@Fe^0-1/1. While Fe^0 was the primary electron source, sorbed Fe(II)

and structural Fe(II) are also effective electron donors for U(VI) reduction. In addition, S^{2-} and S_2^{2-} also contributed to U(VI) reduction.

Chapter 4. Simultaneous Adsorption of Uranium(VI) and 2-Chlorophenol by Activated Carbon Fiber supported Titanate Nanotubes (TNTs@ACF): Synergistic Effect

4.1. Introduction

Uranium (U) is a common contaminant in soil and groundwater resulting from uranium mining and processing, nuclear energy power plants, nuclear weapon tests and nuclear accidents (Chen et al., 2017; Hu et al., 2010). The biotoxicity, bioaccumulation and long half-life (4.5 × 10^9 years for ^{238}U, the main isotope of uranium) of uranium raise public concern and research interests about its effective clean-up. (Barillet et al., 2011; Domingo, 2001; Jaffey et al., 1971; Priest et al., 2001). Chlorinated phenols (CPs) are one of the most common POPs in industrial wastewater. The most important pollutant sources for CPs are wastewater from pesticide, paint, solvent pharmaceutics, and paper and pulp industries (Aksu and Yener, 2001; Schellenberg et al., 1984).

Among all the treatment technologies, the adsorption of contaminants is well studied and widely applied. Activated carbon is usually used to adsorb organic pollutants due to its high adsorption capacity and lower cost (Aksu and Yener, 2001). Titanate nanotubes (TNTs) is an emerging adsorbent for heavy metal adsorption, which exhibits very high uptake capacity towards metal ions and works well in various conditions (Liu et al., 2013).

In some circumstances, heavy metal contaminants coexist with organic pollutants (Riley and Zachara, 1992), and the single-function material is not sufficient for the simultaneous removal of both heavy metal and organic compounds. In this study, a new type of activated carbon fibers supported titanate nanotubes (TNTs@ACFs) is synthesized through a facile one-step hydrothermal treatment. The goal of this study is to test the TNTs@ACFs for U(VI) and 2-CP removal in the single and binary system and understand the synergistic effect on U(VI) and 2-CP adsorption.

4.2. Materials and methods

4.2.1. Materials and Chemicals

Nano-TiO_2 (P25, ca. 80% anatase and 20% rutile, Evonik, Germany), NaOH (Acros Organics, Fair Lawn, NJ, USA) and activated carbon fibers (ACC-FM100, Calgon Zorflex, USA) were used to synthesize TNTs@ACF. Uranyl nitrate dihydrate ($UO_2(NO_3)_2{\cdot}2H_2O$, U in the form of ^{238}U) was purchased from International Bio-Analytical Industrial Inc. (FL, USA), and a U(VI) stock solution of 1000 mg/L was prepared with the addition of 1 mL concentrated HNO_3 to acidify the solution ($pH \approx 2.7$). 2-Chlorophenol from Sigma-Aldrich (St. Louis, MO, USA) was used to prepare a 2-Chlorophenol stock solution of 1000 mg/L and stored at 4 °C. All stock solutions were prepared with Millipore deionized (DI) water (18.2 MΩ cm). Leonardite Humic Acid (HA) 1S104H was obtained International Humic Substances Society (IHSS, St. Paul, MN, USA).

4.2.2. Preparation and characterization of TNTs@ACF.

TNTs@ACF was synthesized through a one-step hydrothermal method modified from our previous study (Liu et al., 2016a). Briefly, 1.2 g of P25 and 1.2 g of ACF and were mixed with 66.7 mL of a 10.8 mol/L NaOH solution and stirred for 12 h. Then, the mixture was transferred to a Teflon reactor sealed with a stainless-steel cover and heated in a muffle furnace at 130 °C for 72 h. The black precipitate (TNTs@ACF) was collected and washed with DI water until pH ~9 and dried in an oven at 105 °C for 4 h.

The morphology information was taken on a Leo 1530 VP field emission scanning electron microscope (FE-SEM) and a JEOL JEM-2100 transmission electron microscope (TEM), respectively. X-ray powder diffraction (XRD) patterns were collected using a Dmax/2400 XRD (Rigaku, Japan) at 100 kV and 40 mA, with the Cu $\kappa\alpha$ radiation (λ = 1.5418 Å) and a scanning rate (2θ) of 4°/min. Zeta potential (ζ) was characterized by a Malvern Zetasizer Nano ZS (Malvern Instrument, Worcestershire, UK). UV-vis absorption spectra were scanned on a SpectraMax M2 spectrophotometer (Molecular Devices, CA, USA). Fourier transform infrared (FTIR) spectroscopy analysis was acquired from a Nicolet iS50 FTIR spectrometer (Thermal Fisher Scientific, Madison, WI, USA). X-ray photoelectron spectroscopy (XPS) characterizations were taken on a XIS-Ultra instrument from Kratos Analytical (Manchester, UK) using Al $K\alpha$ radiation at 15 kV and 15 mA. The static charge effect was compensated using the C 1s peak at 284.80 eV.

4.2.3. Batch adsorption experiments

4.2.3.1. Adsorption kinetics and isotherm

All the adsorption experiments were conducted in duplicate in amber glass bottles with Teflon-lined caps at 22 °C (preliminary tests showed no adsorption of U(VI) or 2-CP by glass bottles and Teflon lined caps). The kinetic tests were initiated by adding 0.02 g of as-prepared TNTs@ACF into 100 mL of U(VI) or 2-CP solution with an initial concentration of 20 mg/L and pH adjusted to 5, then the bottles were placed on a horizontal shaker (200 rpm). The solution pH was kept constant through intermittent adjustment by 0.01 M NaOH or HCl. After a predetermined time interval, 2 mL of sample was taken and immediately filtered through a 0.22 µm Nylon membrane filter, and the filtrates were analyzed to determine the concentration of remained U(VI) or 2-CP per section 2.4.

The U(VI) and 2-CP uptake at time *t* (q_t, mg/g) are calculated by the following equation:

$$q_t = \frac{(C_0 - C_t)V}{m} \quad \textbf{(4-1)}$$

where C_0 and C_t (mg/L) are the concentrations of U(VI) and 2-CP in the initial and at time *t* in the aqueous phase, respectively; *V* (L) is the solution volume and *m* (g) is the mass of the TNTs@ACF.

Experiments on single adsorption isotherm for U(VI) or 2-CP were conducted with U(VI) or 2-CP solution initial concentration ranging from 5 to 300 mg/L and TNTs@ACF dosage of 0.2 g/L at pH 5, while for adsorption isotherms in a binary system, U(VI) and 2-CP were mixed to achieve initial mass concentration ratios of 1:2 and 2:1. After equilibrated for 24 h, the remained concentration of U(VI) or 2-CP in the aqueous phase were determined per section 2.4.

The equilibrium U(VI) and 2-CP uptake (q_e, mg/g) is given by:

$$q_e = \frac{(C_0 - C_e)V}{m} \quad \textbf{(4-2)}$$

where C_0 and C_e (mg/L) are the initial and equilibrium concentrations of U(VI) and 2-CP in the aqueous phase, respectively; *V* (L) is the solution volume and *m* (g) is the mass of the TNTs@ACF.

4.2.3.2. Effect of pH and HA

To probe the effect of pH on the adsorption of U(VI) or 2-CP by TNTs@ACF, the equilibrium adsorption tests were conducted in the pH range of 3.0 to 10.0 with the materials dosage of 0.2 g/L and initial U(VI) or 2-CP concentration of 50 mg/L. For the effect of HA, the equilibrium adsorption tests were also conducted in the presence of 1–10 mg/L as TOC of HA with a fixed pH 5. U(VI) speciation at various pH levels was calculated using software MEDUSA.

4.2.4. Chemical analysis

U(VI) concentration was determined with a Varian 710-ES inductively coupled plasma optical emission spectrometry (ICP-OES, Palo Alto, CA, USA) and the detection limit was 0.07 mg/L. 2-CP concentration was measured on an Agilent 1100 high-performance liquid chromatography (HPLC, USA) equipped with a Zorbax SB-C18 column (2.1 mm × 150 mm, 5 μm) and a diode array detector (DAD). A mixture of methanol (HPLC grade) and ultrapure water (v/v of 60:40) was used as the mobile phase at a flow rate of 0.8 mL/min and the eluate analyzed at a UV array detector of 280 nm. The detection limit of 2-CP by HPLC was 0.02 mg/L.

4.3. Results and discussion

4.3.1. Characterization

The morphology and nanostructure of the as-synthesized material were characterized by FE-SEM and TEM images (**Fig. 4-1**). Unlike the reported neat and smooth surface of untreated ACF (Meng et al., 2014; Park and Jang, 2003), the surface of the TNTs@ACF was evidently rougher and TNTs aggregates were observed on the surface of ACF, indicating the TNTs were successfully loaded onto the ACF surface (**Fig. 4-1a**). A similar rough surface of ACF was also observed after TiO_2 loaded onto ACF (Meng et al., 2014). The TEM image confirmed the hollow and open-ended tubular structure of TNTs, with an inner diameter ca. 5 nm and outer diameter ca. 9 nm (Liu et al., 2013). It is also noted that some micro-ACF particles were patched on the TNTs, which is likely stripped from the bulk ACF during the hydrothermal treatment and this phenomenon is consistent with previous studies (Liu et al., 2016a; Ma et al., 2017). Therefore, the morphology studies showed TNTs is not only supported by the bulk ACF, but also modified by the micro-ACF particles.

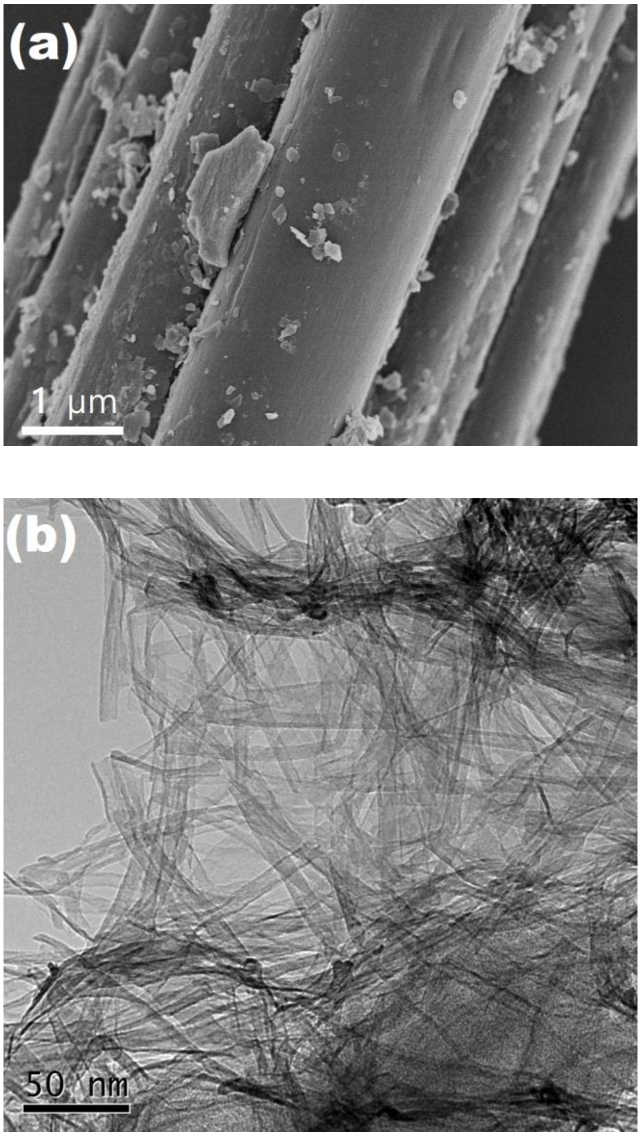

Fig. 4-1. (a) FE-SEM image of TNTs@ACF; **(b)** TEM image of TNTs@ACF.

Fig. 4-2 shows the XRD patterns of neat ACF, TNTs, TNTs@ACF, and U-laden TNTs@ACF. For neat ACF, two peaks at 13.0° and 43.7° were ascribed to the diffraction peaks of graphitic carbon (JCPDS 89-8491) (Dhand et al., 2017; García-Diéguez et al., 2010; Lee et al., 2016). Several minor peaks at 11.8°, 23.7°, 34.8°, 39.4°, and 47.2° were also observed on ACF, which could be due to the diffraction peaks of silicon dioxide (JCPDS 31-1233) (Shukla et al., 2010; Wei et al., 2016). This was also confirmed by the XPS study of the neat ACF, where Si peak was observed on the survey spectra of neat ACF (**Fig. 4-3**) and accounted for 6% of the atomic percentage (**Table 4-1**). For neat TNTs, the diffraction at 2θ value of 9.5°, 24.3°, 28.4°, 48.3°, and 61.8° are all assigned to sodium tri-titanate, with a chemical formula of $Na_xH_{2-x}Ti_3O_7$ (Li et al., 2018; Liu et al., 2013; Liu et al., 2016a). The tri-titanate is composed of triple edge-sharing [TiO6] as a skeletal structure, while 9.5° and 28.4° correspond to interlayer spacing in layered titanates, with exchangeable H^+/Na^+ located in interlayers (Liu et al., 2016a; Ylhäinen et al., 2012). For neat TNTs@ACF, all peaks observed for TNTs remained and a minor graphitic carbon peak at 12.8° was also presented, confirming the ACF was covered by TNTs and was in line with the morphology results. The impurity peaks of SiO_2 were washed off (**Fig. 4-10a and Table 4-1**) via the hydrothermal alkaline treatment during the material preparation (Liu et al., 2016a).

Table 4-1. Surface atomic percentage of fresh ACF and TNTs@ACF and U-laden TNTs@ACF obtained by XPS.

Material	**Element atomic percent (%)**					
	C	O	Ti	Na	Si	U
ACF	81.8	12.2	0	0	6.0	0
TNTs@ACF	62.0	25.7	8.4	3.9	0	0
U(VI)-ladend	61.8	27.5	8.5	1.1	0	1.1
U(VI)- and 2-CP-laden	61.7	27.8	8.3	1.1	0	1.1

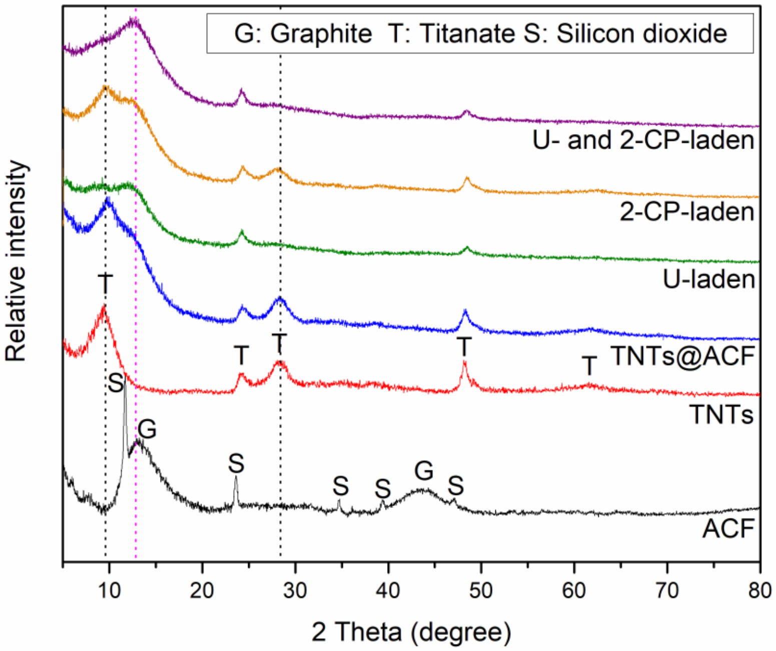

Fig. 4-2. XRD patterns of neat ACF, TNTs, TNTs@ACF, and U-laden TNTs@ACF.

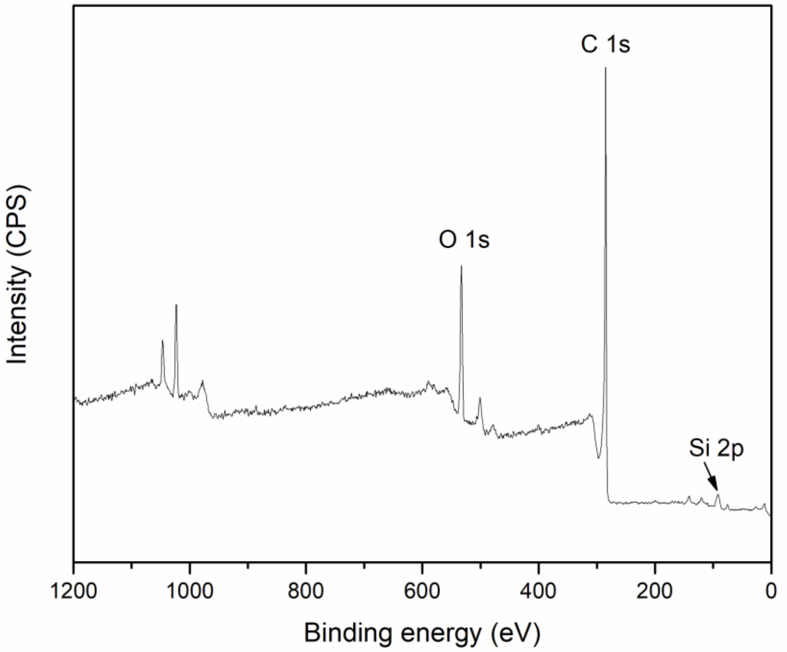

Fig. 4-3. Survey XPS spectra of ACF.

Fig. 4-4 shows the zeta potential profiles of ACF, TNTs, and TNTs@ACF in the pH range of 2–10. For pristine ACF and TNTs, the point of zero charge (pH_{pzc}) was determined to be 2.6 and 3.3, respectively, while the composite TNTs@ACF displayed a pH_{pzc} of 2.7, which suggests the dominant role of TNTs for the surface potential of TNTs@ACF. The negative surface potential of TNTs@ACF over a wide pH range (3.0–10.0) would facilitate the adsorption of U(VI) cations.

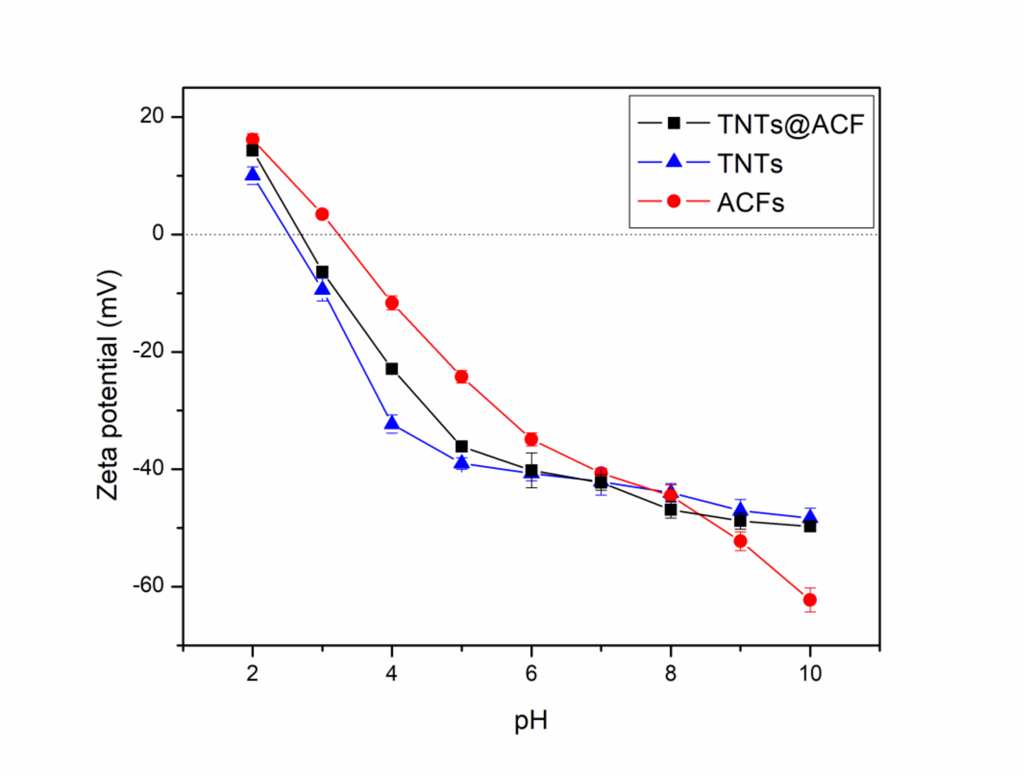

Fig. 4-4. Zeta potential of TNTs, ACF, and TNTs@ACF as a function of solution pH.

4.3.2. Adsorption kinetics

Fig. 4-5 represents the adsorption kinetics of U(VI) or 2-CP by TNTs@ACF with the initial concentration of 20 mg/L. The U(VI) or 2-CP was rapidly adsorbed by TNTs@ACF with the most uptake occurred in the first 15 min and 120 min for 2-CP and U(VI), respectively. The fast adsorption rate is owing to plenty of micropores directly exposed on the surface of ACF, which allows smaller mass transfer resistance (Liu et al., 2010), and abundant ion-exchange sites (–OH/–ONa) in the interlayer of TNTs (Liu et al., 2013; Liu et al., 2016b). At equilibrium, the removal efficiency of U(VI) and 2-CP reached 99% and 60% with finial uptake of 99.5 and 60.1 mg/g, respectively, at the TNTs@ACF dosage of 0.2 g/L.

The adsorption kinetic data was interpreted by the following pseudo-first-order, pseudo-second-order models and intraparticle diffusion models (Ho and McKay, 1998; Kumar, 2006):

$$\text{Pseudo-first-order model: } q_t = q_e - q_e \exp(-k_1 t) \tag{4-3}$$

$$\text{Pseudo-second-order model: } q_t = \frac{k_2 q_e^2 t}{1 + k_2 q_e t} \tag{4-4}$$

$$\text{Intraparticle diffusion model: } q_t = k_{id} t^{0.5} + C \tag{4-5}$$

where q_t and q_e (mg/g) are the U(VI) and 2-CP uptakes at time t and at equilibrium, respectively; k_1 (min^{-1}), k_2 (g/(mg·min)) and k_{id} ($\text{mg/(g}\cdot\text{min}^{0.5})$) are the rate constants of pseudo-first-order, pseudo-second-order, and intraparticle diffusion model, respectively; and C (mg/g) is a constant related to the boundary layer thickness.

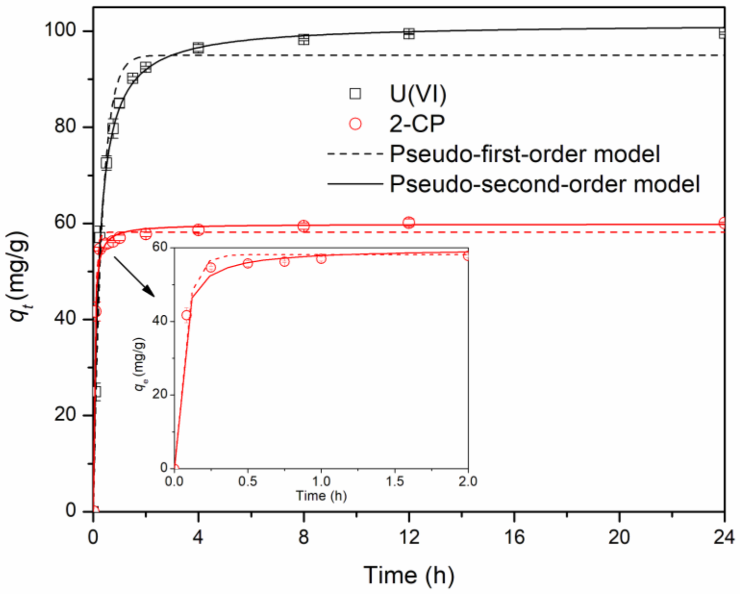

Fig. 4-5. Adsorption kinetics of U(VI) and 2-CP by TNTs@ACF. Experimental conditions: initial concentration of U(VI) and 2-CP = 20 mg/L, material dosage = 0.2 g/L, pH = 5.0 ± 0.1. q_t refers to the uptake of U(VI) and 2-CP at time t. Straight lines: pseudo-first-order model fittings; Dashed lines: pseudo-second-order model fittings. The inset shows the initial uptake rate.

Table 4-2 summarized the best-fitted parameters of the three kinetic models. Apparently, the pseudo-second-order showed better fitting results for the kinetic data, with correlation coefficient $R^2 \geq 0.99$ and the experimental and simulated equilibrium uptakes are in good agreement for both U(VI) and 2-CP. The intraparticle diffusion model usually fits well for AC where film or intraparticle diffusion controls the adsorption rate (Liu et al., 2010; Zogorski et al., 1976), however it can poorly interpret the experimental data in this study ($R^2 \leq 0.47$), suggesting the rate-limiting step may be chemical sorption (Ho and McKay, 2000).

The initial adsorption rate h (mg/(g·min)) is defined as (Ho and McKay, 2000):

$$h = k_2 q_e^{\ 2} \tag{4-6}$$

The initial adsorption rate for U(VI) and 2-CP are calculated to be 487.72 and 1719.63 mg/(g·min), respectively. The higher initial adsorption rate for 2-CP may suggest the preferential adsorption of 2-CP onto TNTs@ACF over U(VI).

Table 4-2. Best-fitted parameters of the pseudo-first-order, pseudo-second-order, and intraparticle diffusion kinetic models for the adsorption of U(VI) or 2-CP by TNTs@ACF

Kinetic models	**Parameters**	**Contaminants**	
		U(VI)	2-CP
Pseudo-first-order kinetic model	k_1 (min^{-1})	3.06	14.72
	$q_{e,\,cal}$ [a] (mg/g)	95.04	58.21
	R^2	0.98	0.98
Pseudo-second-order kinetic model	k_2 (g/(mg·min))	0.047	0.48
	$q_{e,\,cal}$ (mg/g)	101.62	59.89
	h (mg/(g·min))	487.72	1719.63
	R^2	0.99	0.99
Intraparticle diffusion model	k_{id} (mg/(g·min$^{0.5}$))	15.09	5.91
	C (mg/g)	50.50	41.38
	R^2	0.47	0.26
	$q_{e,\,exp}$ [b] (mg/g)	99.62	60.14

[a] Model simulated equilibrium capacity of adsorbates.

[b] Experimental equilibrium uptake of adsorbates.

4.3.3. Adsorption isotherm

4.3.3.1. Adsorption isotherm in the single system

Fig. 4-6 gives the adsorption isotherms of U(VI) and 2-CP on TNTs@ACF in the single system. Two classic Langmuir and Freundlich isotherm models (Freundlich, 1907; Langmuir, 1918) and a dual-mode model (Liu et al., 2016a; Zhao et al., 2001) were applied to fit experimental data.

Langmuir model is based on the assumption of a monolayer adsorption surface with homogenous and equivalent adsorption sites, and there are no interactions between adsorbate and adsorbent sites (Langmuir, 1918), which is defined as:

$$q_e = \frac{Q_{\max} b C_e}{1 + bC_e} \qquad \textbf{(4-7)}$$

where C_e (mg/L) is the equilibrium concentration of U(VI) and 2-CP in the aqueous phase, $Q_{\max}$ (mg/g) is the maximal Langmuir adsorption capacity, b (L/mg) is the Langmuir affinity constant related to the free energy of adsorption.

Freundlich model is an empirical equation that assumes the energetically heterogeneous adsorbent surface (Freundlich, 1907), which is expressed as:

$$q_e = K_F C_e^{1/n} \qquad \textbf{(4-8)}$$

where K_F (mg/g·(L/mg)$^{1/n}$) and n are the Freundlich constants related to the adsorption capacity and the adsorption intensity of the adsorbent, respectively.

In our previous studies (Liu et al., 2016a), a dual-mode adsorption model was proposed to elucidate the adsorption process of phenanthrene onto TNTs@AC, which contains

Langmuir-type adsorption in the low concentration range and capillary condensation in the high concentration range, and is represented as:

$$q_e = \frac{Q_{max} b C_e}{1 + b C_e} + K_d C_e \tag{4-9}$$

where K_d is the distribution coefficient; $Q_{\max}$ and b are the corresponding constants of the Langmuir model.

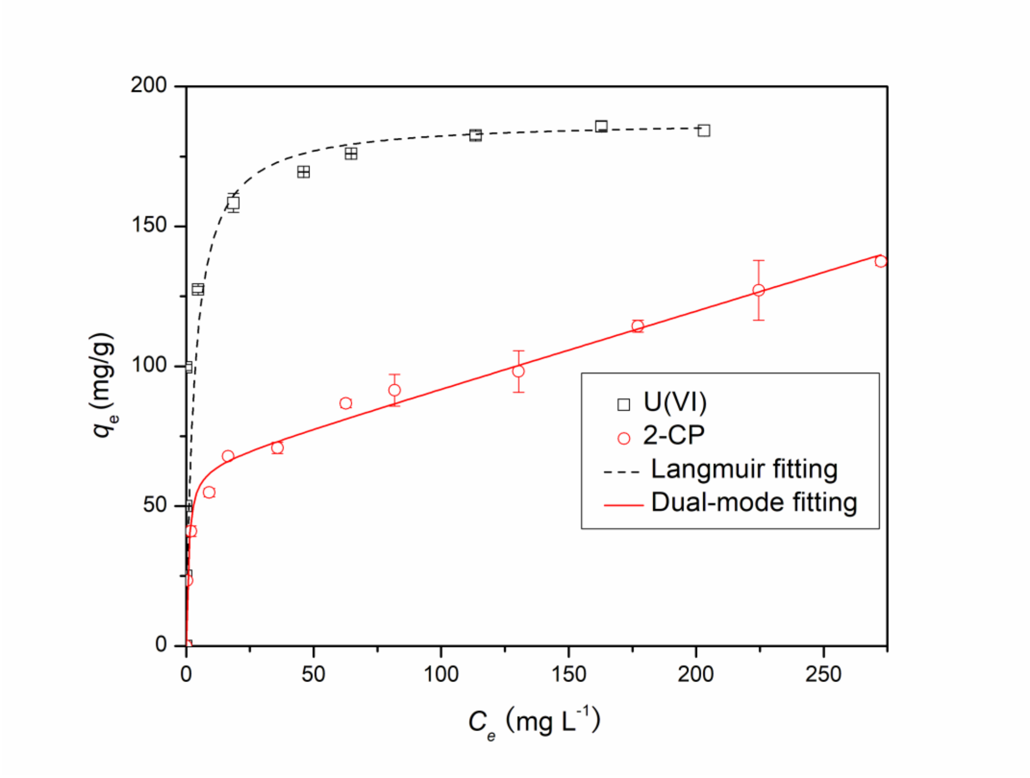

Fig. 4-6. Adsorption isotherms of U(VI) and 2-CP onto TNTs@ACFs in the single system. Experimental conditions: initial concentration of U(VI) = 5–240 mg/L, 2-CP = 5–300 mg/L, materials dosage = 0.2g/L, pH = 5.0 ± 0.1, and temperature = 22 ± 1 °C. q_e refers to the equilibrium uptake of U(VI) and 2-CP. Straight lines: dual-mode model fittings; dashed lines: Langmuir model fitting.

Table 4-3 presents the calculated isotherm parameters for adsorption of U(VI) or 2-CP in the single system. For U(VI), the Langmuir model shows the best fitting result (R^2 = 0.98) among the three models, with maximum capacity ($Q_{\max}$) determined to be 188.03 mg/g. This observation is consistent with U(VI) adsorption by TNTs, indicating TNTs may serve as the main adsorption sites in the composite material (Liu et al., 2016b). The high adsorption capacity for U(VI) is due to the large specific area and abundant adsorption sites (−OH/−ONa) (Liu et al., 2013). For 2-CP, however, the dual-mode model gives better fitting (R^2 = 0.99) than the classic Langmuir and Freundlich model, which is likely attributed to combined adsorption on the ACF surface and "hole-filling" or capillary condensation in the nanotubes (Liu et al., 2016a). Based on the Langmuir model, the maximum adsorption capacity ($Q_{\max}$) of 2-CP was determined to be 122.14 mg/g.

Table 4-3. Isotherm model parameters for adsorption of U(VI) or 2-CP by TNTs@ACF in the single system.

Kinetic models	Parameters	Contaminants	
		U(VI)	2-CP
Langmuir model	Q_{max} (mg/g)	188.03	122.14
	b (L/mg)	0.32	0.068
	R^2	0.98	0.86
Freundlich model	K_F (mg/g ·(L/mg)$^{1/n}$)	119.84	30.35
	n	11.57	3.86
	R^2	0.93	0.98
Dual-mode model	K_d (L/g)	0.21	0.28
	Q_{max} (mg/g)	150.92	64.64
	b (L/mg)	20.94	1.18
	R^2	0.92	0.99

4.3.3.2. Adsorption isotherm in the binary system

Fig. 4-7 depicted the adsorption isotherm of U(VI) and 2-CP in the binary system and **Table 4-4** listed the corresponding isotherm parameters. Evidently, the adsorption capacity in the binary system was larger than that in the single system. The Langmuir maximum adsorption capacity ($Q_{\max}$) for U(VI) was 188.03, 242.32, and 248.63 mg/g with U(VI) only, U(VI) to 2-CP mass ratio of 2:1 and 1:2, respectively, while the $Q_{\max}$ for 2-CP increased from 122.14 mg/g in the single system to 169.11 and 255.60 mg/g at U(VI) to 2-CP mass ratio of 1:2 and 2:1, respectively. The experimental data was better interpreted by the dual-mode model, with $R^2 > 0.97$ for all cases, suggesting other than the above mentioned "hole-filling" or capillary condensation in the nanotubes, some other promotive mechanism may also contribute to the enhanced adsorption. The synergistic effect could be due to the additional adsorption sites on the TNTs@ACF after U(VI) complexes with 2-CP. For example, in the single system, U(VI) was mainly adsorbed by TNTs and ACF only provided limited adsorption capacity; while in binary system, U(VI) complexes with 2-CP so ACF could also effectively adsorb the U(VI)–2-CP complex and enhance the total U(VI) uptake. Similarly, after 2-CP complexed with U(VI), except the original adsorption sites on ACF, TNTs could also provide additional adsorption capacity for U(VI)–2-CP complex and thereby enhancing the total 2-CP adsorption (see **Section 3.5** for detail). This speculation is in line with the increased distribution coefficient (K_d) value when more complexes are formed (**Table 4-4**). For example, the K_d value of U(VI) adsorption was 0.21 L/g in the single system, while it increased to 0.66 and 0.69 L/g at U(VI) to 2-CP mass ratio of 2:1 and 1:2. A lower U(VI) to 2-CP mass ratio means more 2-CP presented in the system with the same U(VI) concentration, resulting in more U(VI)-2-CP complex formation. The same trend was also observed for 2-CP.

Table 4-4. Isotherm model parameters for adsorption of U(VI) and 2-CP by TNTs@ACF in the binary system.

Kinetic models	**Parameters**	**1:2** [a]		**2:1** [a]	
		U(VI)	2-CP	U(VI)	2-CP
Langmuir model	Q_{max} (mg/g)	248.63	169.11	242.32	255.60
	b (L/mg)	0.32	0.029	0.28	0.013
	R^2	0.78	0.90	0.76	0.92
Freundlich model	K_F (mg/g ·(L/mg)$^{1/n}$)	113.99	23.94	114.21	20.01
	N	6.16	2.90	6.55	2.37
	R^2	0.94	0.98	0.92	0.98
Dual-mode model	K_d (L/g)	0.69	0.39	0.66	0.64
	Q_{max} (mg/g)	151.62	71.23	143.21	60.34
	b (L/mg)	58.11	0.41	93.25	2.69
	R^2	0.97	0.99	0.97	0.99

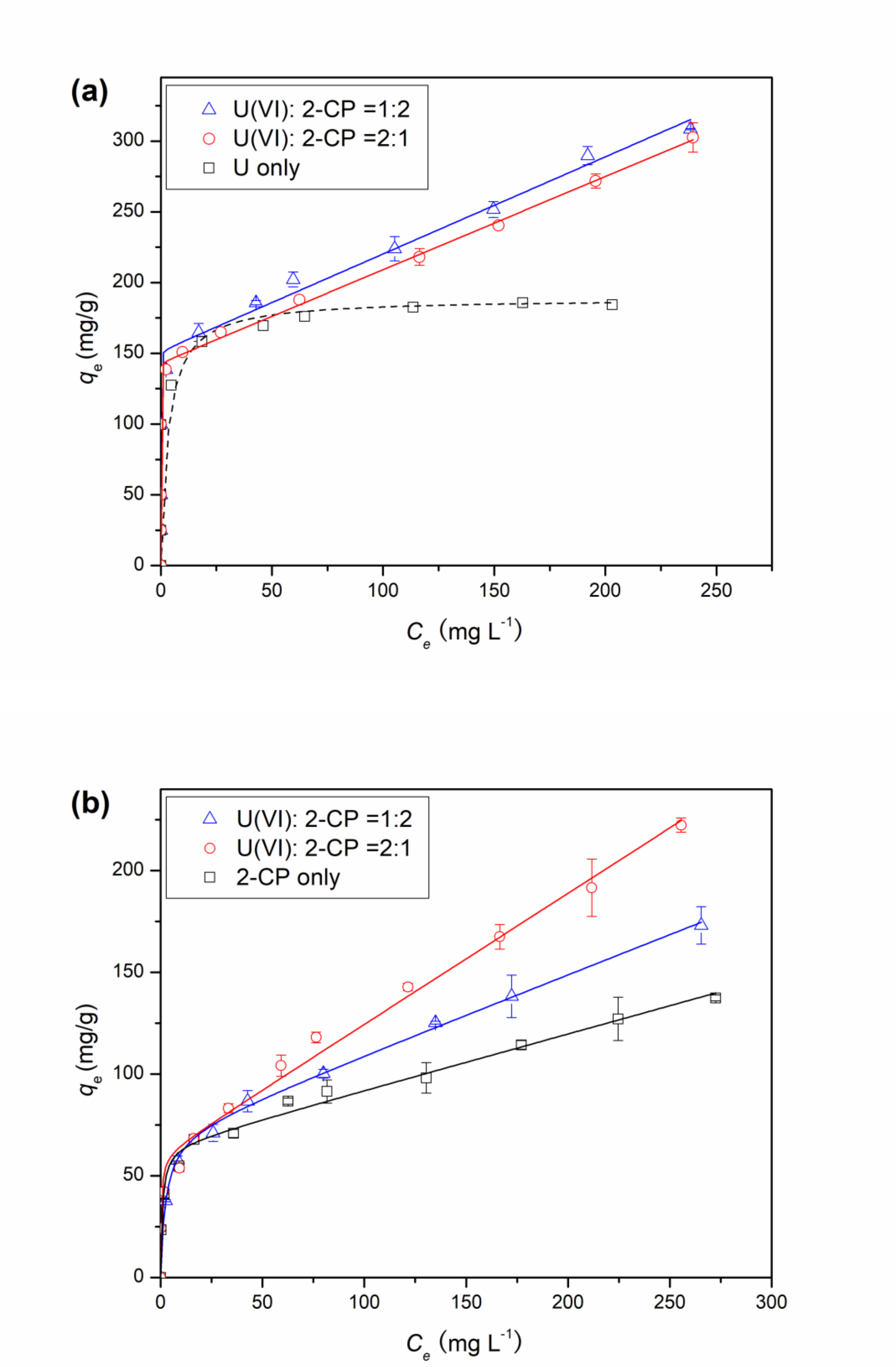

Fig. 4-7. Adsorption isotherm of **(a)** U(VI) and **(b)** 2-CP by TNTs@ACFs in the binary

system (isotherm in the single system was plotted here for comparison). Experimental conditions: initial concentration of U(VI) and 2-CP = 5–300 mg/L, materials dosage = 0.2g/L, pH = 5.0 ± 0.1, and temperature = 22 ± 1 °C. q_e refers to the equilibrium uptake of U(VI) and 2-CP. Straight lines: dual-mode model fittings; dashed lines: Langmuir model fitting.

4.3.4. Effects of pH and Humic acid

4.3.4.1. Effects of pH

The effect of pH on the adsorption of U(VI) and 2-CP was investigated by batch techniques and shown in **Fig. 4-8a**. For U(VI), the equilibrium uptake increased significantly with increasing the pH from 3.0 to 7.0, with a maximum uptake at pH 7 (241.3 mg/L), while the U(VI) uptake dropped at pH > 7.0. As shown in **Fig. 4-4**, at pH < 7.0, the zeta potential of the material sharply turned less negative with decreased pH, thereby remarkably weakening the electrostatic attractions between the TNTs@ACF and cationic species (UO_2^{2+}, UO_2OH^+, $(UO_2)_2(OH)_2^{2+}$, $(UO_2)_3(OH)_5^+$, and $(UO_2)_4(OH)_7^+$) (**Fig S2**) (especially at pH 3.0). Besides, excess H^+ also compete for adsorption sites at low pH. Except for strong electrostatic attraction, the strong reducing power of the ACF was also responsible for the high uptake of U(VI). Sun et al. (Sun et al., 2016) observed oxygen-containing groups in the carbon nanofibers (CNFs) could not only strongly complex with U(VI) but also partially reduce the U(VI) to U(IV). In the XPS results below (**section 3.5**), the high resolution of U $4f_{7/2}$ peak could be deconvoluted into U(VI) and U(IV) species, confirming the partial reduction of U(VI) by ACF. At pH >7.0, the zeta potential of TNTs@ACF remained negative (< -42.3 mV), while the predominant U(VI) species changed to $(UO_2)_3(OH)_7^-$, $(UO_2)_2(OH)_3^-$, and $(UO_2)_2(OH)_4^{2-}$ uranyl anions (**Fig. 2-5**), which were strongly repelled by the negatively-charged surface and thereby inhibiting the U(VI) uptake.

Unlike U(VI), the uptake of 2-CP by TNTs@ACF at various pH levels showed a clear adsorption edge. At pH ≤ 7.0, the uptake reaches a plateau and keeps stable adsorption capacity of ca. 69.7 mg/g, then the adsorption capacity gradually decreased at pH above 7.0. This trend is consistent with the pKa value of 2-CP (8.52) (Liu et al., 2010). At pH < pKa, the 2-CP is in protonated form and no electrostatic repulsion force exists between 2-CP and TNTs@ACF, thus the adsorption capacity keeps at a high level and unchanged. While at pH > pKa, the 2-CP deprotonated and repelled by the negatively charged TNTs@ACF surface (pH_{pzc} = 2.7). Further increasing the pH, the 2-CP dissociate to a higher degree and the ACFs surface became more negatively charged, resulting in an enhanced repulsive force between each other and lower adsorption capacity. The adsorbed 2-CP anions would also contribute to the increased electrostatic repulsion to inhibit the uptake of free 2-CP anions. Moreover, deprotonation will cause a decrease in the hydrophobicity of 2-CP, thereby diminishing the affinity of 2-CP to ACF (Liu et al., 2010).

4.3.4.2. Effects of Humic acid

The results of the adsorption of U(VI) and 2-CP onto TNTs@ACF in the presence of HA are shown in **Fig. 4-8b**. Increasing the HA concentration from 0 to 10 mg/L as TOC, the adsorption capacity of U(VI) progressively enhanced from 158 to 164.7 mg/g. HA may pose distinct effects on the U(VI) adsorption. On the one hand, HA can easily form binary $UO_2HA(II)$ and ternary $UO_2(OH)HA(I)$ complexes in water and inhibit the adsorption of U(VI) by TNTs@ACF (Duan et al., 2019). On the other hand, HA can be adsorbed by TNTs@ACF through complexation with Ti and hydrophobic interactions, π–π interactions, polar/electrostatic interactions, and hydrogen-bonding with ACF (Liu et al., 2016b; Yazdani et al., 2019). Then, the surface sorbed HA could provide more adsorption sites to complex with U(VI) ions from the aqueous phase. Enhanced uptake of heavy metal (e.g., Cd, Cr, Pb, U) in the presence of humic acid was observed by other researchers (Abate and Masini, 2005; Lai et al., 2002; Tan et al., 2017). For example, Tan et al (2017) found adsorption capacity of U(VI) increased from 12 mg/g in the absence of HA to 42 mg/g and 59 mg/g in the presence of 10 mg/L and 25 mg/L HA, respectively. Evidently, the ad-solubilization effect of HA on U(VI) uptake by TNTs@ACF outcompeted the solubilization effect in the present study.

2-CP adsorption capacity was increased from 69.8 mg/g to 80.2 mg/g with HA concentration increased from 0 to 5 mg/L as TOC, while slightly decreased to 73.8 mg/g when further increasing the HA concentration to 10 mg/L as TOC. The promotive effect of HA on 2-CP adsorption could be attributed to two aspects: 1) TNTs can hardly adsorb hydrophobic hydrocarbons due to the hydrophilic nature (W. Liu et al., 2016a), while HA sorbed on the TNTs can amend the TNTs surface from no affinity to accessible towards 2-CP, thereby providing additional sorption sites for 2-CP. 2) the sorbed HA on TNTs@ACF contains 4.76 and 1.47 meq/g of carboxyl and phenolic groups, respectively (Fujii et al., 2014), and the hydroxy group of 2-CP can interact with oxygen-containing groups in HA *via* hydrogen bonding thus enhancing the 2-CP uptake (Wang et al., 2009). Sun et al. (2012) reported the adsorption capacity of 1-naphthol was enhanced from 54.5 mg/g for neat multiwall carbon nanotubes (MWCNTs) to 97.1 mg/g for HA-coated MWCNTs, and they ascribed mechanism of enhanced adsorption to more sorption sites induced from oxygen-containing groups associated with HA. The inhibitive effect at high

HA concentration (10 mg/L as TOC) may be due to the elevated aggregation of HA molecules on TNT surface (Tsang et al., 2009), which makes the oxygen-containing groups less accessible for 2-CP.

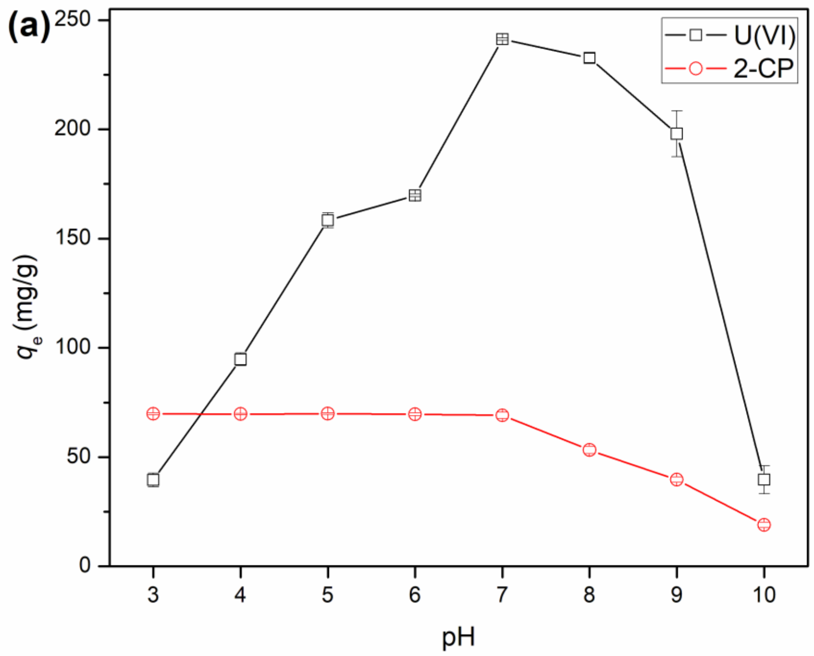

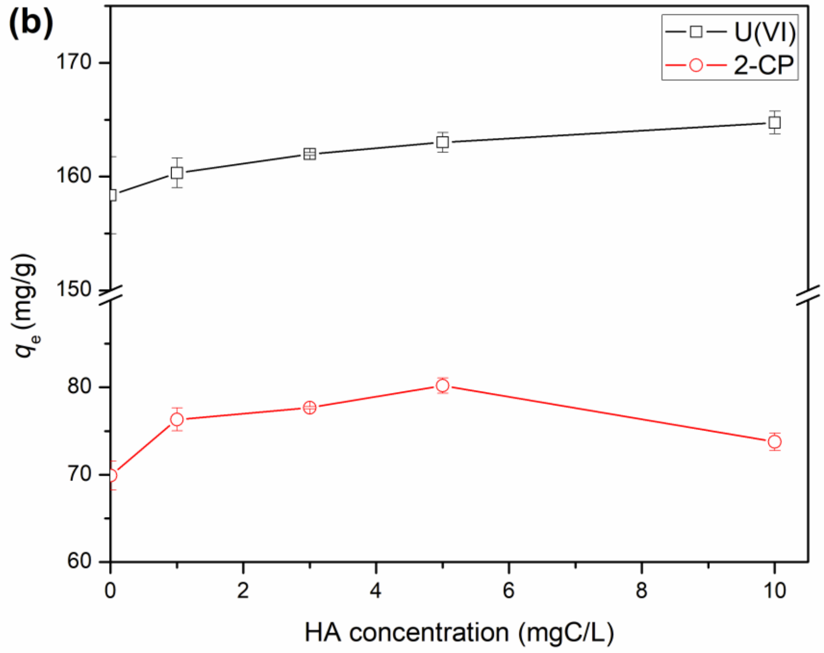

Fig. 4-8. Effects of (a) pH, (b) HA on equilibrium uptake of U(VI) and 2-CP by TNTs@ACF. Experimental conditions: initial concentration of U(VI) and 2-CP = 50 mg/L, material dosage = 0.2 g/L, pH = 5.0 ± 0.1. q_e refers to the equilibrium uptake of U(VI) and 2-CP.

4.3.5. Mechanism for enhanced adsorption of U(VI) and 2-CP in the binary system

XRD, XPS, FTIR, and UV-vis characterizations were further investigated to elucidate the underlying mechanism of enhanced adsorption of U(VI) and 2-CP by TNTs@ACF in the binary system. As shown in the XRD patterns (**Fig. 4-2**), for samples loaded with U(VI), the intensity of peaks at 9.5° and 28.4° that represent the interlayer distance of TNTs sharply diminished, indicating the interlayer distance is enlarged after the ion exchange between U(VI) with a larger ionic radius and Na^+/H^+ (Ma et al., 2017). This observation is different with the previous study of neat TNTs that interlayer structure was not significantly altered during the ion-exchange process (Liu et al., 2013; Liu et al., 2016b), but in line with the interaction between TNTs@AC and Pb(II), which could be due to the metastable state of TNTs caused by intrusion of micro-carbon into the interlayer of TNTs during the formation of the tubular structure (Ma et al., 2017). Other TNTs characteristic diffraction peaks remain similar to the fresh TNTs@ACF, suggesting the ion-exchange process does not change the basic [TiO6] octahedron structure of TNTs (Liu et al., 2016b). Compared to the neat TNTs@ACF, the intensity of graphitic diffraction peak at 13º was increased after sample laden with U(VI) or 2-CP, and significant enhancement was observed in the U(VI) and 2-CP binary system. This finding is consistent with Namasivayam and Kavitha (2006)'s result, in which they observed the enhancement of the graphitic diffraction peak after the adsorption of dye and phenol molecules, and they explained the adsorption reaction would alter the structure of the carbon resulting from the molecules diffuse into the micropores and macropores and adsorb mostly by chemisorption. The stronger alteration of the pore structure in the binary system than that of the single system suggesting the synergistic effect of U(VI) and 2-CP co-adsorption by ACF.

The survey XPS analyses of **Fig. 4-9a** show that the elemental composition of neat TNTs@ACF are C (62.0%), O (25.7%), Na (3.9%), and Ti (8.4%) (**Table 4-1**). Based on the basic structure of titanate ($Na_xH_{2-x}Ti_3O_7$), the chemical formula of as-prepared TNTs@ACF in this study can be written as $[Na_{1.39}H_{0.61}Ti_3O_7\cdot 2.18H_2O][22.14C]$, in which "$[Na_{1.39}H_{0.61}Ti_3O_7\cdot 2.18H_2O]$" stands for the structure of TNTs and "[22.14C]" represents ACF. According to the manufacturer, the ACF is 100% activated carbon, thus the TNTs to ACF mass ratio is determined to be 1:0.92. After loaded with U(VI) in single and binary system, U 4f peak was clearly identified in the survey spectra while the intensity of Na 1s peak was significantly suppressed, suggesting the mechanism of U(VI) uptake is mainly owing to the ion-exchange between U(VI) and –ONa in the interlayer of TNTs (Liu et al., 2016b). The O content increased from 25.7% to 27.5 and 27.8% in the single and binary system, respectively, which is due to the uptake of uranyl ions (UO_2^{2+}) and uranyl hydroxide complexes (e.g. $UO_2(OH)^+$). The chemical formula of U(VI)-laden samples was calculated to be $[(UO_2)_{0.39}Na_{0.39}H_{1.22}Ti_3O_7 \cdot 1.92H_2O][21.81C]$ and $[(UO_2)_{0.40}Na_{0.40}H_{1.2}Ti_3O_7 \cdot 2.25H_2O][22.30C]$ for single system and binary system, respectively. For U(VI)-laden sample, the high-resolution of U 4f spectra (**Fig. 4-9b**) is deconvoluted into two peaks at 382.3 and 380.6 eV, which are ascribed to U(VI) and U(IV), respectively (Duan et al., 2019). It shows U(VI) is not only adsorbed by TNTs@ACF but also partially reduced to U(IV). Our previous work (Liu et al., 2016b) confirmed the adsorbed U on TNTs are all in the oxidation state of U(VI) and no reduction of U(VI) occurred, so it is likely that ACF contributes to the U(VI) reduction. The speculation is proved in Sun et al. (2016)'s study of U(VI) adsorption on carbonaceous nanofibers, in which a U(IV) peak was also found in their U 4f spectra and the reduction of U(VI) is verified by X-ray absorption near edge structure (XANES) analysis. In the U(VI)–2-CP binary system, the binding energy of U(VI) slightly shifts to 382.2 eV, indicating the chemical environment change for U(VI) caused by U(VI) complexing with 2-CP (Li et al., 2014; J. Liu et al., 2016), while U(IV) remains the same at 380.6 eV, implying no complex formed between U(IV) and 2-CP. The C 1s spectra further confirms the redox reaction between U(VI) and ACF (**Fig. 4-9c**). Before loaded with contaminants, fresh TNTs@ACF contains four carbon peaks, i.e., C-C/C-H (37.4%) at 284.8 eV, C-O (44.4%) at 285.4 eV, C=O (12.2%) at 287.0 eV, and C(O)O (6.0%) at 289.0 eV (Liu et al., 2016a; Sun et al., 2016; Wang et al., 2018). Upon adsorption of U(VI), the C-O percentage decreased from 44.4% to 34.8% and 36.7% and C(O)O group increased from 6.0% to 14.2% and 12.6% for the single and binary system, respectively, which indicates the oxidation of R-CH_2OH groups to R-COOH groups in contact with U(VI) according the equation as follows (Sun et al., 2016):

$$2R\text{-}CH_2OH + 2UO_2^{2+} + O_2 = 2R\text{-}COOH + 2UO_2(s) + 4H^+ \qquad (\mathbf{4\text{-}10})$$

The high-resolution profile of O 1s in TNTs@ACF was fitted to three peaks (**Fig. 4-9d**), which are lattice O of [TiO_6] (37.4%) at 530.7 eV, O from hydroxyl groups bonded with metal or carbon (M-OH/C-OH) (28.5%) at 532.1 eV, suggesting the C–O–Ti bond linkage between TNTs and ACF, and a minor peak of O from combined water (3.6%) at 536.0 eV (Liu et al., 2016a; Ma et al., 2017). M-OH/C-OH peak increased to ca. 39% in the U(VI)-laden samples, which is ascribed to the uptake of uranyl species bonded oxygen.

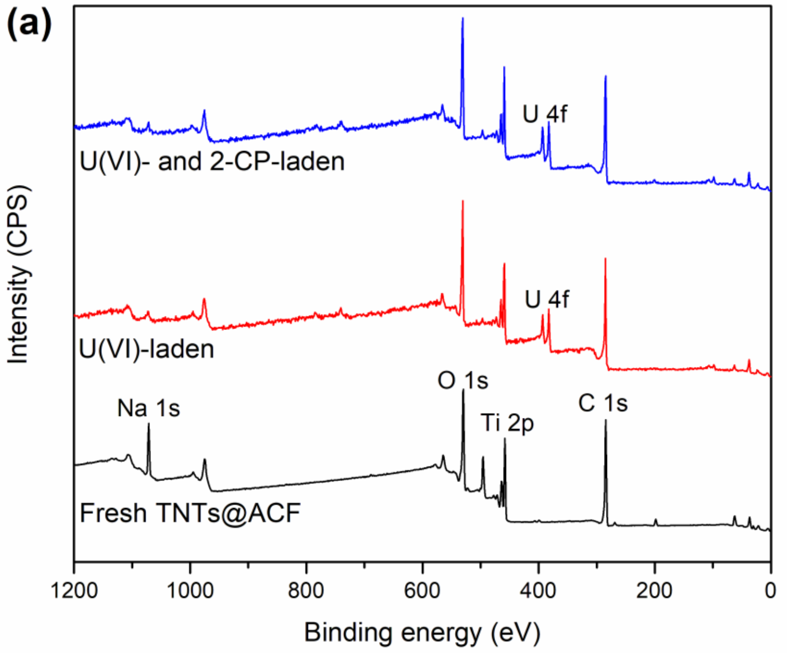
(a)
U(VI)- and 2-CP-laden
U 4f
U(VI)-laden
U 4f
Na 1s
O 1s
Ti 2p
C 1s
Fresh TNTs@ACF
Intensity (CPS)
1200
1000
800
600
400
200
0
Binding energy (eV)

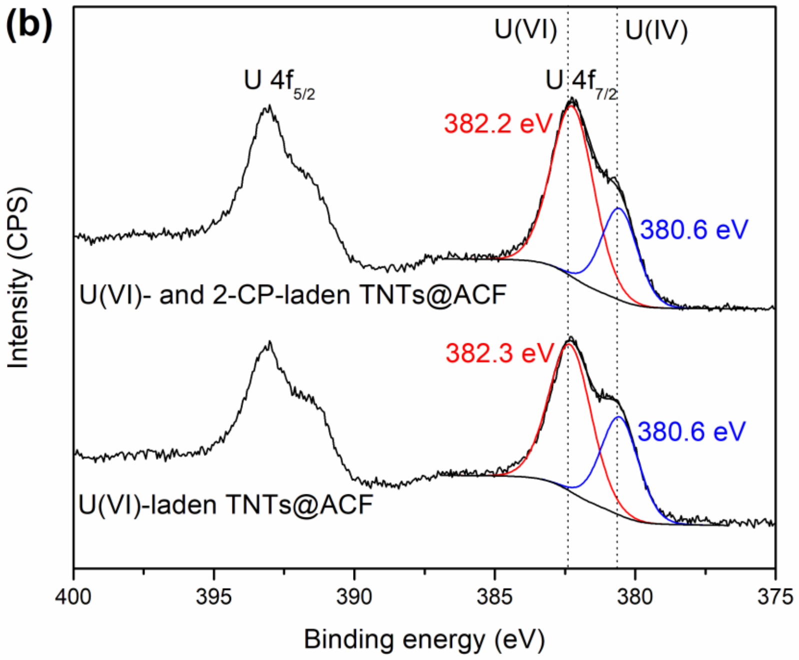
(b)
U(VI)
U(IV)
U 4f$_{5/2}$
U 4f$_{7/2}$
382.2 eV
380.6 eV
U(VI)- and 2-CP-laden TNTs@ACF
382.3 eV
380.6 eV
U(VI)-laden TNTs@ACF
Intensity (CPS)
400
395
390
385
380
375
Binding energy (eV)

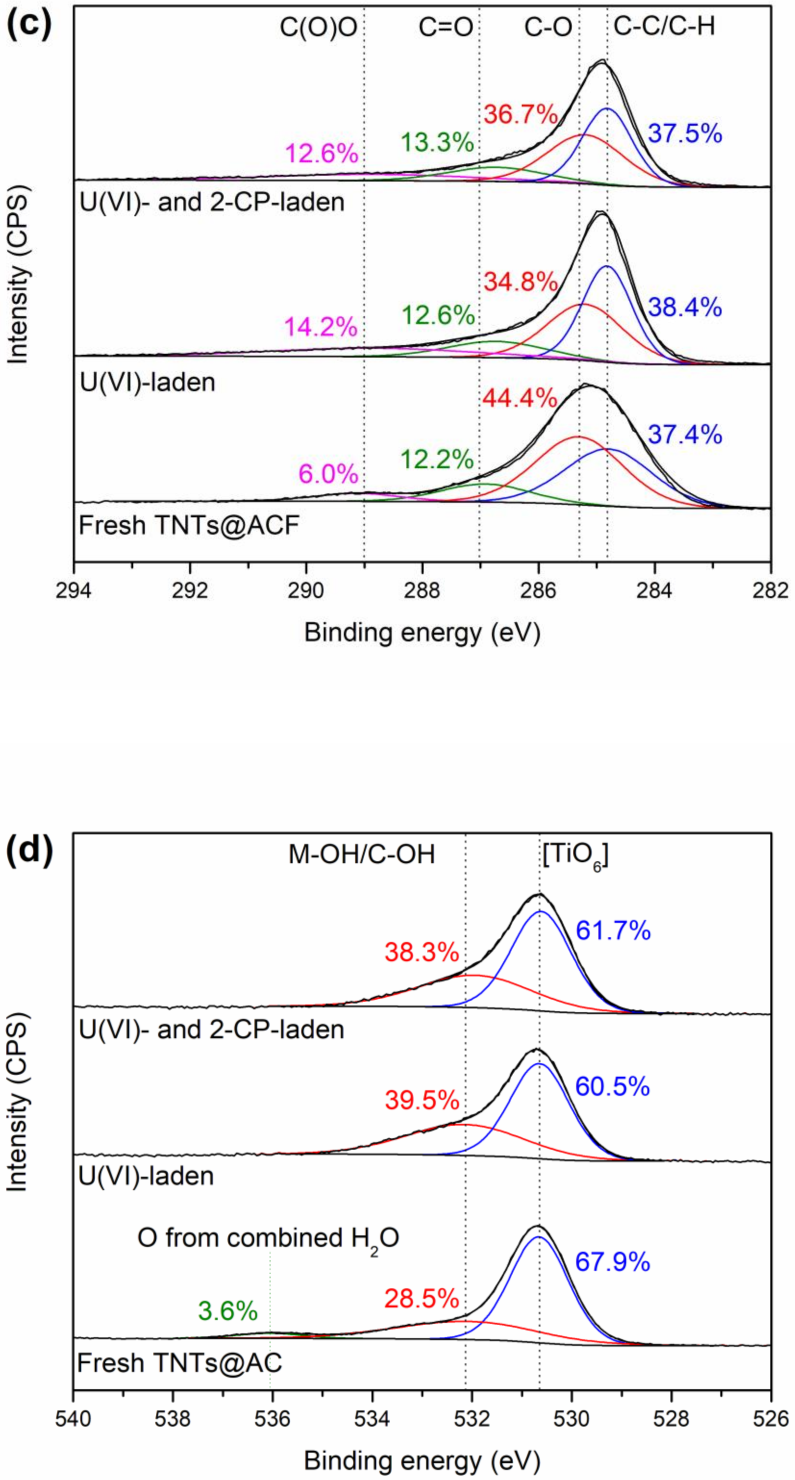

Fig. 4-9. XPS spectra of TNTs@ACF and U-laden TNTs@ACF. **(a)** Survey XPS, **(b)** high

resolution of U 4f, **(c)** high resolution of C 1s, and **(d)** high resolution of O1s.

Fig. 4-10 shows the FTIR spectra of neat TNTs and TNTs@ACF before and after adsorption of U(VI) and/or 2-CP. Four characteristic peaks at 3302, 1640, 1342, and 892 cm^{-1} are observed on the neat TNTs, which are attributed to of O–H vibration of hydroxyl groups, H–O–H vibration from bonded water molecules, O–Na band of TNTs, and coordinated Ti–O involving non-bridging oxygen atoms coordinated with Na ions ($TiO(ONa)_2$), respectively (Hua et al., 2017; Liu et al., 2016b, 2016a; Wang et al., 2015). These bands were all observed on neat TNTs@ACF with peaks center shifted to a lower frequency, indicating the interactions between TNTs and ACF. Upon reaction with U(VI) (**spectra c**), the peak center of $TiO(ONa)_2$ shifted from 887 cm^{-1} of neat TNTs@ACF to 919 cm^{-1} and peak O–Na disappeared, which is due to the ion-exchange of Na^+ in $TiO(ONa)_2$ with UO_2^{2+} (Liu et al., 2016b; Wang et al., 2015). After adsorption of 2-CP (**spectra d**), broad doublet peaks at 3344 and 3238 cm^{-1} are attributed to the characteristic phenolic O–H vibration bands (Li et al., 2014). Compared to the neat TNTs@ACF, the intensity of peak at 1626 cm^{-1} is remarkably enhanced, which is due to the overlap of stretching vibration of C=C groups (aromatic ring deformation) (Oliveira et al., 2016) and the H–O–H band. A new minor peak at 1434 cm^{-1} is observed, which is owing to the fundamental C–C stretching vibration of the benzene ring (Sahasrabudhe et al., 2001). In the U(VI) and 2-CP simultaneous system (**spectra e**), doublet phenolic bands remarkably weakened and shifted to 3187 cm^{-1} and the modification of phenolic O–H band would reveal the coordination of phenolic oxygen to the uranyl ion (Azam et al., 2015; Chen et al., 2010). The shifting of the uranyl band (from 919 cm^{-1} in the single system to 911 cm^{-1} in the binary system) also proves the complexation between 2-CP and U(VI) (Bernstein et al., 2014). Moreover, the peak intensity of the aromatic C=C band reduced and the C–C band disappeared upon mixing 2-CP with U(VI). The change of aromatic band intensity is likely due to the π–cation interactions between U(VI) cations and 2-CP molecules. A study of benzene adsorption by zeolite loaded with various group IIA cations showed different intensity of benzene characteristic bands, and they explained the phenomenon was due to the intermolecular interaction between π-electron cloud and cations (Sahasrabudhe et al., 2001). Consequently, both 2-CP and U(VI) could be adsorbed by TNTs@ACF in the single system, while 2-CP and U(VI) bonded together in the binary system through complexation and π-cation interactions.

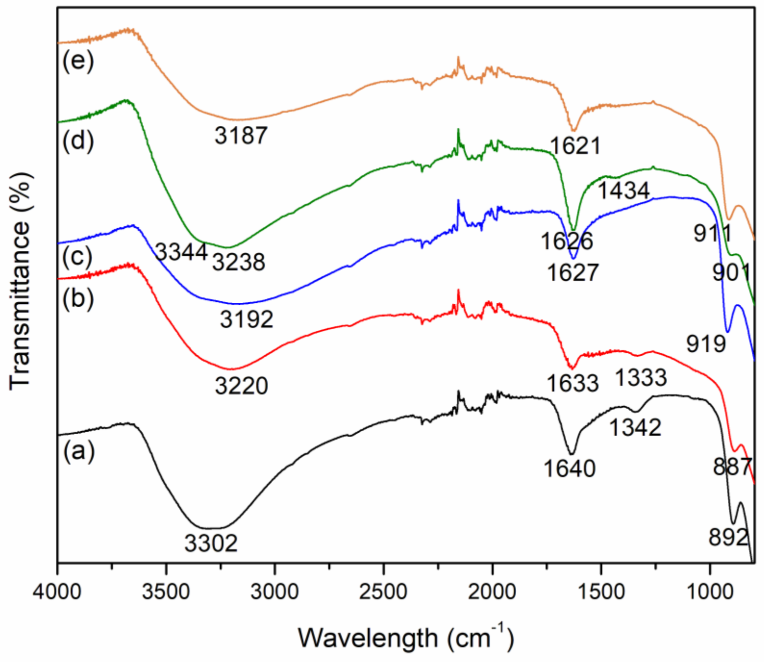

Fig. 4-10. FTIR spectra of **(a)** TNTs, **(b)** TNTs@ACF, **(c)** U-laden TNTs@ACF, **(d)** 2-CP-laden TNTs@ACF, and **(e)** U- and 2-CP-laden TNTs@ACF.

Fig. 4-11 represents the measured UV-vis absorbance spectra at a U(VI) concentration of 300 mg/L at pH 5 as a function of the 2-CP concentration. Evidently, an enhanced absorbance and blue shift of the absorbance maxima when the 2-CP concentration increased from 0 to 600 mg/L, indicating the formation of uranyl and 2-CP complexes (Glorius et al., 2007). Sarakha et al. (2000) analyzed the UV-vis absorbance spectra of U(VI)/4-CP mixture and observed a similar increase of absorbance when 4-CP to U(VI) molar ratio increased, who attributed the enhancement to complexing of the phenolic group with UO_2^{2+}.

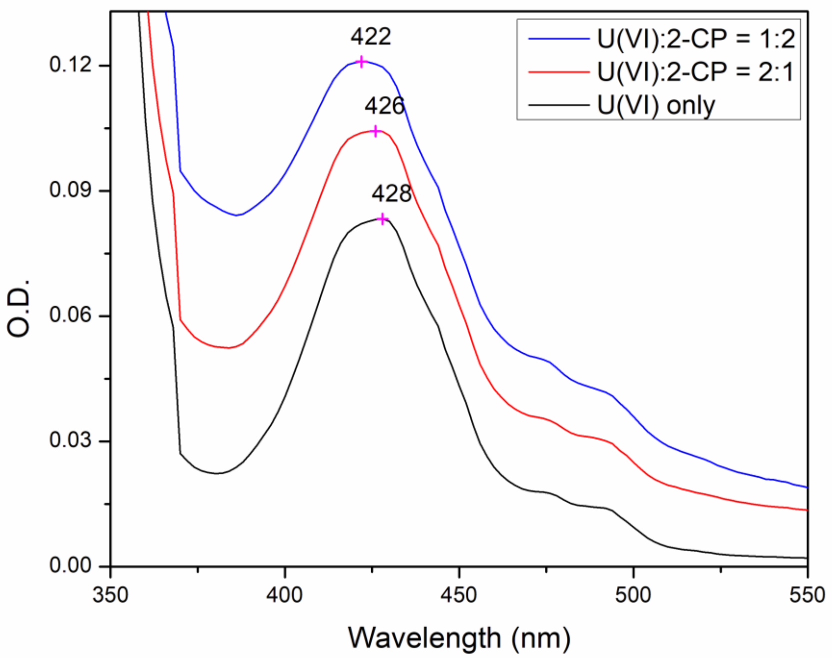

Fig. 4-11. UV-Vis absorption spectra of U(VI) alone and U(VI)/2-CP mixture at various mass ratios. Experimental conditions: U(VI) = 300 mg/L, 2-CP = 150–600 mg/L, pH = 5.0 ± 0.2.

4.4. Conclusions

This study prepared a new type of TNTs@ACF composite materials through a one-step hydrothermal approach and tested the material for remove of U(VI) and 2-CP in the single and binary system. FESEM and TEM characterization confirmed TNTs is not only supported by the bulk ACF, but also modified by the micro-ACF particles. The material exhibited high adsorption capacity for U(VI) (188.03 mg/g) and 2-CP (122.14 mg/g), while an increased adsorption capacity was observed in the binary system and can reach up to 248.63 and 255.60 mg/g for U(VI) and 2-CP, respectively. The pseudo-second-order adsorption model better fitted the kinetic data with $R^2 > 0.99$, while the dual-mode model successfully interpreted the adsorption isotherms with $R^2 > 0.97$ for all cases. XRD, XPS, FTIR and UV-vis studies of TNTs@ACF before and after reaction with U(VI) and 2-CP confirmed the adsorption mechanism of U(VI) is mainly due to ion-exchange between uranyl ions and –OH/ONa functional groups located in the interlayer of TNTs, while the uptake of 2-CP is owing to the hydrophobic interactions, π–π interactions and hole filling process. The enhanced adsorption of U(VI) and 2-CP in the binary system results from the complexation of uranyl ions and phenolic group and π–cation interaction of U(VI) cations and benzene ring that provide additional adsorption sites and synergistically promote adsorption capacity. The optimal working pH for U(VI) ranges from 6–8, with the maximum capacity at pH 7, while an adsorption edge at pH 7 is observed for 2-CP. Increasing the HA concentration from 0 to 10 mg/L as TOC would enhance the U(VI) adsorption capacity from 158.4 to 164.7 mg/L. 2-CP uptake was enhanced in the HA concentration range of 0–5 mg/L as TOC, but 10 mg/L as TOC of HA would impede the adsorption. TNTs@ACF appear promising for simultaneous removal of U(VI) and 2-CP from complex wastewater.

Chapter 5. Conclusions and Suggestions for Future Research

5.1. Summary and conclusions

Uranium wastewater mainly comes from nuclear weapon manufacturing and testing, nuclear power plant operation, and uranium mining and processing. Due to the sparing solubility of U(IV), reductive immobilization of U(VI) works as a popular strategy to treat U(VI) contamination. In this study, two kinds of iron particles, i.e., CMC-FeS and FeS@Fe^0 are prepared and tested for reductive removal of U(VI) under various water chemistry conditions. Adsorption is another practical approach to remove U(VI) from waste and a new type of TNTs@ACF nanomaterials were synthesized for simultaneous adsorption of U(VI) and 2-CP from water.

The optimal CMC-FeS was obtained at the CMC-to-FeS molar ratio of 0.0010, which showed both high particle stability and U(VI) removal efficiency. CMC-FeS performed well over the pH range 6.0-9.0, and the best removal occurred at pH 7.0 and 8.0, where > 95% U removal was achieved with 1 hour. The retarded first-order model adequately interpreted the kinetic data, representing a mechanistically sounder model for heterogeneous reactants of decaying reactivity. Ca^{2+} has stronger inhibitive effects than Na$^+$, while the presence of bicarbonate significantly decreased the removal rate. The reaction was enhanced in the presence of 1 mg/L of HA as TOC, while a higher concentration of HA (5-10 mg/L as TOC) impeded the reaction. Further, 87% of U(VI) removal was still reached under complex synthetic groundwater conditions. Fourier transform infrared spectroscopy, X-ray photoelectron spectroscopy, and extraction studies indicated that the reductive conversion of UO_2^{2+} to $UO_{2(s)}$ was the primary mechanism for immobilization of U(VI) by CMC-FeS, which accounted for 90% of U removal at pH 7.0. S^{2-} and S_2^{2-} were the primary electron sources, whereas sorbed and structural Fe(II) acted as supplementary electron donors for U(VI) reduction. The immobilized U remained highly stable under anoxic condition after 180 days of aging, while ~26% immobilized U was remobilized when exposed to air for 180 days. The long-term stability is attributed to the reductive protecting potential of CMC-FeS, the formation of uraninite and the associated structural resistance to oxidation, and the high affinity of the FeS oxidation products toward U(VI).

A new type of FeS-modified ZVI core-shell particles (FeS@Fe^0) through a facile two-step reaction approach, and then tested for reductive sequestration of U(VI) in water. X-ray diffraction, Scanning transmission electron microscopy, and physical property analyses confirmed the formation of the core-shell structure, surface compositions, and magnetic properties. Batch kinetic tests showed that FeS@Fe^0 with an Fe^0/FeS molar ratio of 1:1 offered the highest U(VI) reduction rate, prolonged reactive life than pristine ZVI, and the reduced uranium was most resistant to re-oxidation when exposed to oxygen. The retarded first-order kinetic model was able to adequately interpret the experimental rate data. FeS@Fe^0 performed well over the pH range 5.5-9.0, with higher pH more favoring the reaction. High concentrations (5-10 mg/L) of humic acid, bicarbonate (1-5 mM) and Ca^{2+} (1 mM) showed only modest inhibition to the U(VI) reduction. Fourier transform infrared spectroscopy, X-ray photoelectron spectroscopy, and extraction studies indicated that U(VI) was immobilized *via* both direct adsorption and reductive precipitation, where Fe^0 was the main electron source, with Fe^0, sorbed Fe(II) and structural Fe(II) acting as the electron donors. $FeS@Fe^0$ may serve as an improved material for the efficient immobilization of U(VI) and other redox-active contaminants in water.

Morphology studies of TNTs@ACF show the TNTs were well supported by the ACF and modified with some micro-carbon particles patched on the surface. The as-prepared materials exhibit excellent adsorption capacity for U(VI) and 2-CP in the single system, while a significant enhancement of the adsorption capacity for both contaminants were observed in the binary system. Neutral pH favors the adsorption of U(VI) and 2-CP. Humic acid enhances the adsorption of U(VI) but only increases the adsorption capacity of 2-CP when HA < 5 mg/L as TOC, and a higher HA concentration will impede the adsorption of 2-CP. The uptake of U(VI) by TNTs@ACF is mainly occurring through ion-exchange between uranyl ions and –OH/ONa functional groups located in the interlayers of TNTs, while for, while the uptake of 2-CP is owing to the hydrophobic interactions, π–π interactions and hole filling process. The enhanced adsorption of U(VI) and 2-CP in the binary system results from the complexation of uranyl ions and phenolic group and π–cation interaction of U(VI) cations and benzene ring that provide additional adsorption sites and synergistically promote adsorption capacity. TNTs@ACF appears promising for the treatment of uranium and organic pollutants coexisting wastewater.

5.2. Suggestions for future work

This study investigated the removal of U(VI) from wastewater using two categories of nanomaterials, namely, iron-based nanoparticles and titanate based nanomaterials. There are still scientific gaps need to be filled and the specific suggestions are as follows:

1) Iron-based nanoparticles could effectively remove U(VI) through adsorption and reduction under anoxic conditions, but their performance under oxic conditions needs to be tested in order to better understand the practical application of iron-based nanoparticles for treatment of U(VI) from wastewater.
2) The application of synthesized nanomaterials for other heavy metals and radionuclides or competitive removal needs be studied to broaden the usage of the materials.
3) The photoreduction of U(VI) and photodegradation of 2-CP by TNTs@ACF needs to be tested to further immobilization/degradation of the contaminants.
4) Density function theory calculation is a powerful tool to understand the chemical reaction and the usage of DFT can facilitate the elucidation of the reaction mechanism of U(VI) removal.
5) The toxicity of the synthesized nanomaterials to the environment remains unclear so studies are needed for the of the iron-based nanoparticles and titanate nanomaterials

References

Abdulhamid, H., Fridell, E., Dawody, J., Skoglundh, M., 2006. In situ FTIR study of SO_2 interaction with $Pt/BaCO_3/Al_2O_3$ NO_x storage catalysts under lean and rich conditions. J. Catal. 241, 200–210.

Abate, G., Masini, J.C., 2005. Influence of pH, ionic strength and humic acid on adsorption of Cd(II) and Pb(II) onto vermiculite. Colloids Surfaces A Physicochem. Eng. Asp. 262, 33–39.

Agrawal, A., Ferguson, W.J., Gardner, B.O., Christ, J.A., Bandstra, J.Z., Tratnyek, P.G., 2002. Effects of carbonate species on the kinetics of dechlorination of 1,1,1-trichloroethane by zero-valent iron. Environ. Sci. Technol. 36, 4326–4333.

Arai, Y., Marcus, M.A., Tamura, N., Davis, J.A. and Zachara, J.M., 2007. Spectroscopic evidence for uranium bearing precipitates in vadose zone sediments at the Hanford 300-area site. Environ. Sci. Technol. 41, 4633–4639.

Azam, M., Al-Resayes, S.I., Velmurugan, G., Venuvanalingam, P., Wagler, J., Kroke, E., 2015. Novel uranyl(VI) complexes incorporating propylene-bridged salen-type N_2O_2-ligands: A structural and computational approach. Dalt. Trans. 44, 568–577.

Backett, R., Jue, Z., Giddings, J.C., 1987. Determination of Molecular Weight Distributions of Fulvic and Humic Acids Using Flow Field-Flow Fractionation. Environ. Sci. Technol. 21, 289–295.

Bernstein, K.J., Do-Thanh, C.L., Penchoff, D.A., Alan Cramer, S., Murdock, C.R., Lu, Z., Harrison, R.J., Camden, J.P., Jenkins, D.M., 2014. The synthesis and spectroscopic characterization of an aromatic uranium amidoxime complex. Inorganica Chim. Acta. 421, 374–379.

Bi, Y., Hayes, K.F., 2014. Nano-FeS inhibits UO_2 reoxidation under varied oxic conditions. Environ. Sci. Technol. 48, 632–640.

Bi, Y., Hyun, S.P., Kukkadapu, R., Hayes, K.F., 2013. Oxidative dissolution of UO_2 in a simulated groundwater containing synthetic nanocrystalline mackinawite. Geochim. Cosmochim. Acta. 102, 175–190.

Bi, Y., Stylo, M., Bernier-Latmani, R., Hayes, K.F., 2016. Rapid Mobilization of Noncrystalline U(IV) Coupled with FeS Oxidation. Environ. Sci. Technol. 50, 1403–1411.

Cao, Z., Liu, X., Xu, J., Zhang, J., Yang, Y., Zhou, J., Xu, X., Lowry, G.V., 2017. Removal of antibiotic florfenicol by sulfide-modified nanoscale zero-valent iron. Environ. Sci. Technol. 51, 11269–11277.

Carpenter, J., Bi, Y., Hayes, K.F., 2015. Influence of iron sulfides on abiotic oxidation of UO_2 by nitrite and dissolved oxygen in natural sediments. Environ. Sci. Technol. 49, 1078–1085.

Chen, H., Zhang, Z., Yang, Z., Yang, Q., Li, B., Bai, Z., 2015. Heterogeneous fenton-like catalytic degradation of 2,4-dichlorophenoxyacetic acid in water with FeS. Chem. Eng. J. 273, 481–489.

Chen, Y.C., Lo, S.L., Kuo, J., 2010. Pb(II) adsorption capacity and behavior of titanate nanotubes made by microwave hydrothermal method. Colloids Surfaces A Physicochem. Eng. Asp. 361, 126–131.

Chiriţă, P., Descostes, M., Schlegel, M.L., 2008. Oxidation of FeS by oxygen-bearing acidic solutions. J. Colloid Interface Sci. 321, 84–95.

Conway, B.E., Ku, J.C.H., Ho, F.C., 1980. The electrochemical surface reactivity of iron sulfide, FeS2. J. Colloid Interface Sci. 75(2), 357–372.

Crane, R.A., Pullin, H., Scott, T.B., 2015. The influence of calcium, sodium and bicarbonate on the uptake of uranium onto nanoscale zero-valent iron particles. Chem. Eng. J. 277, 252–259.

Descostes, M., Schlegel, M.L., Eglizaud, N., Descamps, F., Miserque, F., Simoni, E., 2010. Uptake of uranium and trace elements in pyrite (FeS_2) suspensions. Geochim. Cosmochim. Acta. 74, 1551–1562.

Dhand, V., Mittal, G., Rhee, K.Y., Park, S.J., 2017. Synthesis and comparison of different spinel ferrites and their catalytic activity during chemical vapor deposition of polymorphic nanocarbons. Int. J. Precis. Eng. Manuf. Green Technol. 4, 441–451.

Domingo, J.L., 2001. Reproductive and developmental toxicity of natural and depleted uranium: A review. Reprod. Toxicol. 15, 603–609.

Dong, H., Zhang, C., Deng, J., Jiang, Z., Zhang, L., Cheng, Y., Hou, K., Tang, L., Zeng, G., 2018. Factors influencing degradation of trichloroethylene by sulfide-modified nanoscale zero-valent iron in aqueous solution. Water Res. 135, 1–10.

Dong, H., Zhao, F., Zeng, G., Tang, L., Fan, C., Zhang, L., Zeng, Y., He, Q., Xie, Y., Wu, Y., 2016. Aging study on carboxymethyl cellulose-coated zero-valent iron nanoparticles in water: Chemical transformation and structural evolution. J. Hazard. Mater. 312, 234–242.

Dong, W., Brooks, S.C., 2006. Determination of the formation constants of ternary complexes of uranyl and carbonate with alkaline earth metals (Mg^{2+}, Ca^{2+}, Sr^{2+}, and Ba^{2+}) using anion exchange method. Environ. Sci. Technol. 40, 4689–4695.

Du, J., Bao, J., Lu, C., Werner, D., 2016. Reductive sequestration of chromate by hierarchical FeS@Fe^0 particles. Water Res. 102, 73–81.

Duan, J., Ji, H., Liu, W., Zhao, X., Han, B., Tian, S., Zhao, D., 2019. Enhanced immobilization of U(VI) using a new type of FeS-modified Fe^0 core-shell particles. Chem. Eng. J. 359, 1617–1628.

Ehrhardt, J., Charlet, L., Poincare, H., 2010. U(VI) Sorption and Reduction by Fe (II) Sorbed on Montmorillonite. Environ. Sci. Technol. 44, 3779–3785.

Fan, D., Anitori, R.P., Tebo, B.M., Tratnyek, P.G., Lezama Pacheco, J.S., Kukkadapu, R.K., Engelhard, M.H., Bowden, M.E., Kovarik, L., Arey, B.W., 2013. Reductive sequestration of pertechnetate (^{99}TcO^{4-}) by nano zerovalent iron (nZVI) transformed by abiotic sulfide. Environ. Sci. Technol. 47, 5302–5310.

Fan, D., Anitori, R.P., Tebo, B.M., Tratnyek, P.G., Lezama Pacheco, J.S., Kukkadapu, R.K., Kovarik, L., Engelhard, M.H., Bowden, M.E., 2014. Oxidative remobilization of technetium sequestered by sulfide-transformed nano zerovalent iron. Environ. Sci. Technol. 48, 7409–7417.

Fan, D., Lan, Y., Tratnyek, P.G., Johnson, R.L., Filip, J., O'Carroll, D.M., Nunez Garcia, A., Agrawal, A., 2017. Sulfidation of Iron-Based Materials: A Review of Processes and Implications for Water Treatment and Remediation. Environ. Sci. Technol. 51, 13070–13085.

Fan, D., O’Brien Johnson, G., Tratnyek, P.G., Johnson, R.L., 2016. Sulfidation of nano zerovalent iron (nZVI) for improved selectivity during in-situ chemical reduction (ISCR). Environ. Sci. Technol. 50, 9558–9565.

Fiedor, J. N., Bostick, W. D., Jarabek, R. J. & Farrel, J. 1998. Understanding the mechanism of uranium removal from groundwater by zero-valent iron using X-ray photoelectron spectroscopy. Environ. Sci. Technol. 32, 1466–1473.

Forrester, M., Kusmartsev, F., 2014. The nano-mechanics and magnetic properties of high moment synthetic antiferromagnetic particles. Phys. Status solidi-A, 211(4), 884–889.

Frazier, S.W., Kretzschmar, R., Kraemer, S.M., 2005. Bacterial siderophores promote dissolution of UO_2 under reducing conditions. Environ. Sci. Technol. 39, 5709–5715.

Freundlich, H., 1907. Über die Adsorption in Lösungen. Zeitschrift für Phys. Chemie 57U.

Fujii, M., Imaoka, A., Yoshimura, C., Waite, T.D., 2014. Effects of molecular composition of natural organic matter on ferric iron complexation at circumneutral pH. Environ. Sci. Technol. 48, 4414–4424.

Gallegos, T.J., Fuller, C.C., Webb, S.M., Betterton, W., 2013. Uranium(VI) interactions with mackinawite in the presence and absence of bicarbonate and oxygen. Environ. Sci. Technol. 47, 7357–7364.

García-Diéguez, M., Pieta, I.S., Herrera, M.C., Larrubia, M.A., Malpartida, I., Alemany, L.J., 2010. Transient study of the dry reforming of methane over Pt supported on different γ-Al_2O_3. Catal. Today 149, 380–387.

Giasuddin, A.B., Kanel, S.R., Choi, H., 2007. Adsorption of humic acid onto nanoscale zerovalent iron and its effect on arsenic removal. Environ. Sci. Technol. 41(6), 2022–2027.

Glaus, M.A., Hummel, W., Loon, L.R.V., 1995. Stability of Mixed-Ugand Complexes of Metal Ions with Humic Substances and Low Molecular Weight Ligands. Environ. Sci. Technol. 29, 2150–2153.

Glorius, M., Moll, H., Bernhard, G., 2007. Complexation of uranium(VI) with aromatic acids in aqueous solution-a comparison of hydroxamic acids and benzoic acid. Radiochim. Acta. 95, 151–157.

Gong, J., Lee, C.S., Chang, Y.Y., Chang, Y.S., 2015. Novel self-assembled bimetallic structure of Bi/Fe^0: The oxidative and reductive degradation of hexahydro-1,3,5-trinitro-1,3,5-triazine (RDX). J. Hazard. Mater., 286, 107–117.

Gong, Y., Gai, L., Tang, J., Fu, J., Wang, Q., Zeng, E.Y., 2017. Reduction of Cr(VI) in simulated groundwater by FeS-coated iron magnetic nanoparticles. Sci. Total Environ. 595, 743–751.

Gong, Y., Liu, Y., Xiong, Z., Zhao, D., 2014. Immobilization of mercury by carboxymethyl cellulose stabilized iron sulfide nanoparticles: Reaction mechanisms and effects of stabilizer and water chemistry. Environ. Sci. Technol. 48, 3986–3994.

Gong, Y., Liu, Y., Xiong, Z., Zhao, D., 2014. Immobilization of mercury by carboxymethyl cellulose stabilized iron sulfide nanoparticles: Reaction mechanisms and effects of stabilizer and water chemistry. Environ. Sci. Technol. 48, 3986–3994.

Gong, Y., Tang, J., Zhao, D., 2016. Application of iron sulfide particles for groundwater and soil remediation: A review. Water Res. 89, 309–320.

Gorman-Lewis, D., Skanthakumar, S., Jensen, M., Mekki, S., Nagy, K.L., Soderholm, L., 2008. FTIR characterization of amorphous uranyl-silicates. Chem. Geol. 253, 136–140.

Han, W., Gao, M., 2008. Investigations on iron sulfide nanosheets prepared via a single-source precursor approach. Cryst. Growth Des. 8, 1023–1030.

Han, Y., Yan, W., 2016. Reductive Dechlorination of Trichloroethene by Zero-valent Iron Nanoparticles: Reactivity Enhancement through Sulfidation Treatment. Environ. Sci. Technol. 50, 12992–13001.

He, F., Zhao, D., 2007. Manipulating the size and dispersibility of zerovalent iron nanoparticles by use of carboxymethyl cellulose stabilizers. Environ. Sci. Technol. 41, 6216–6221.

He, F., Zhao, D., 2008. Hydrodechlorination of trichloroethene using stabilized Fe-Pd nanoparticles: Reaction mechanism and effects of stabilizers, catalysts and reaction conditions. Appl. Catal. B Environ. 84, 533–540.

He, F., Zhao, D., Liu, J., Roberts, C.B., 2007. Stabilization of Fe-Pd nanoparticles with sodium carboxymethyl cellulose for enhanced transport and dechlorination of trichloroethylene in soil and groundwater. Ind. Eng. Chem. Res. 46, 29–34.

Henderson, A.D., Demond, A.H., 2013. Permeability of iron sulfide (FeS)-based materials for groundwater remediation. Water Res. 47, 1267–1276.

Ho, C.H., Miller, N.H., 1985. Effect of humic acid on uranium uptake by hematite particles. J. Colloid Interface Sci. 106, 281–288.

Ho, Y.S., McKay, G., 1998. Sorption of copper(II) from aqueous solution by Peat. Water. Air. Soil Pollut. 158, 77–97.

Ho, Y.S., McKay, G., 2000. The kinetics of sorption of divalent metal ions onto sphagnum moss peat. Water Res. 34, 735–742.

Hu, Q.H., Weng, J.Q., Wang, J.S., 2010. Sources of anthropogenic radionuclides in the environment: A review. J. Environ. Radioact. 101, 426–437.

Hua, B., Deng, B., 2008. Reductive immobilization of uranium(VI) by amorphous iron sulfide. Environ. Sci. Technol. 42, 8703–8708.

Hua, B., Xu, H., Terry, J., Deng, B., 2006. Kinetics of uranium(VI) reduction by hydrogen sulfide in anoxic aqueous systems. Environ. Sci. Technol. 40, 4666–4671.

Hua, S., Yu, X., Li, F., Duan, J., Ji, H., Liu, W., 2017. Hydrogen titanate nanosheets with both adsorptive and photocatalytic properties used for organic dyes removal. Colloids Surfaces A Physicochem. Eng. Asp. 516, 211–218.

Huo, L., Xie, W., Qian, T., Guan, X., Zhao, D., 2017. Reductive immobilization of pertechnetate in soil and groundwater using synthetic pyrite nanoparticles. Chemosphere, 174, 456–465.

Hyun, S.P., Davis, J.A., Sun, K., Hayes, K.F., 2012. Uranium(VI) reduction by iron(II) monosulfide mackinawite. Environ. Sci. Technol. 46, 3369–3376.

Kang, M., Chen, F., Wu, S., Yang, Y., Bruggeman, C., Charlet, L., 2011. Effect of pH on aqueous Se(IV) reduction by pyrite. Environ. Sci. Technol. 45, 2704–2710.

Kim, E.J., Kim, J.H., Azad, A.M., Chang, Y.S., 2011. Facile synthesis and characterization of Fe/FeS nanoparticles for environmental applications. ACS Appl. Mater. Interfaces. 3, 1457–1462.

Kim, E.J., Murugesan, K., Kim, J.H., Tratnyek, P.G., Chang, Y.S., 2013. Remediation of trichloroethylene by FeS-coated iron nanoparticles in simulated and real groundwater: Effects of water chemistry. Ind. Eng. Chem. Res. 52, 9343–9350.

Křepelová, A., Sachs, S., Bernhard, G., 2006. Uranium(VI) sorption onto kaolinite in the presence and absence of humic acid. Radiochim. Acta. 94, 825–833.

Kumar, K.V., 2006. Linear and non-linear regression analysis for the sorption kinetics of methylene blue onto activated carbon. J. Hazard. Mater. 137, 1538–1544.

Lai, C.H., Chen, C.Y., Wei, B.L., Yeh, S.H., 2002. Cadmium adsorption on goethite-coated sand in the presence of humic acid. Water Res. 36, 4943–4950.

Langmuir, I., 1918. The adsorption of gases on plane surfaces of glass, mica and platinum. J. Am. Chem. Soc. 40, 1361–1403.

Lee, D. kyu, Ahn, C.W., Jeon, H.J., 2016. Web of carbon fibers coated with 3D snowflake-shaped Ni_3S_2/Ni produced by electroless Ni plating: A binder-free cathode electrode for lithium batteries. Microelectron. Eng. 166, 1–4.

Li, B., Li, S., Liu, J., Wang, B., Yang, S., 2015. Vertically aligned sulfur-graphene nanowalls on substrates for ultrafast lithium-sulfur batteries. Nano Lett. 15, 3073–3079.

Li, B., Ma, L., Tian, Y., Yang, Xiaodan, Li, J., Bai, C., Yang, Xiaoyu, Zhang, S., Li, S., Jin, Y., 2014. A catechol-like phenolic ligand-functionalized hydrothermal carbon: One-pot synthesis, characterization and sorption behavior toward uranium. J. Hazard. Mater. 271, 41–49.

Li, D., Mao, Z., Zhong, Y., Huang, W., Wu, Y., Peng, P.A., 2016. Reductive transformation of tetrabromobisphenol A by sulfidated nano zerovalent iron. Water Res. 103, 1–9.

Li, D., Zhu, X., Zhong, Y., Huang, W., Peng, P., 2017. Abiotic transformation of hexabromocyclododecane by sulfidated nanoscale zerovalent iron: Kinetics, mechanism and influencing factors. Water Res. 121, 140–149.

Li, F., Du, P., Liu, W., Li, X., Ji, H., Duan, J., Zhao, D., 2018. Hydrothermal synthesis of graphene grafted titania/titanate nanosheets for photocatalytic degradation of 4-chlorophenol: Solar-light-driven photocatalytic activity and computational chemistry analysis. Chem. Eng. J. 331, 685–694.

Li, J., Zhang, X., Sun, Y., Liang, L., Pan, B.C., Zhang, W., Guan, X., 2017. Advances in Sulfidation of Zerovalent Iron for Water Decontamination. Environ. Sci. Technol. 51, 13533–13544.

Li, Y., Li, L., Chen, T., Duan, T., Yao, W., Zheng, K., Dai, L. and Zhu, W., 2018. Bioassembly of fungal hypha/graphene oxide aerogel as high performance adsorbents for U (VI) removal. Chem. Eng. J. 347, 407–414.

Li, Z.J., Wang, L., Yuan, L.Y., Xiao, C.L., Mei, L., Zheng, L.R., Zhang, J., Yang, J.H., Zhao, Y.L., Zhu, Z.T., Chai, Z.F., Shi, W.Q., 2015. Efficient removal of uranium from aqueous solution by zero-valent iron nanoparticle and its graphene composite. J. Hazard. Mater. 290, 26–33.

Lin, K., Liu, W., Gan, J., 2009. Reaction of tetrabromobisphenol A (TBBPA) with manganese dioxide: Kinetics, products, and pathways. Environ. Sci. Technol. 43, 4480–4486.

Liu, J., Zhu, R., Xu, T., Xu, Y., Ge, F., Xi, Y., Zhu, J., He, H., 2016. Co-adsorption of phosphate and zinc(II) on the surface of ferrihydrite. Chemosphere. 144, 1148–1155.

Liu, Q.S., Zheng, T., Wang, P., Jiang, J.P., Li, N., 2010. Adsorption isotherm, kinetic and mechanism studies of some substituted phenols on activated carbon fibers. Chem. Eng. J. 157, 348–356.

Liu, W., Cai, Z., Zhao, X., Wang, T., Li, F., Zhao, D., 2016a. High-Capacity and Photoregenerable Composite Material for Efficient Adsorption and Degradation of Phenanthrene in Water. Environ. Sci. Technol. 50, 11174–11183.

Liu, W., Wang, T., Borthwick, A.G.L., Wang, Y., Yin, X., Li, X., Ni, J., 2013. Adsorption of Pb^{2+}, Cd^{2+}, Cu^{2+} and Cr^{3+} onto titanate nanotubes: Competition and effect of inorganic ions. Sci. Total Environ. 456, 171–180.

Liu, W., Zhao, X., Wang, T., Zhao, D., Ni, J., 2016b. Adsorption of U(VI) by multilayer titanate nanotubes: Effects of inorganic cations, carbonate and natural organic matter. Chem. Eng. J. 286, 427–435.

Liu, X., Du, P., Pan, W., Dang, C., Qian, T., Liu, H., Liu, W., Zhao, D., 2018. Immobilization of uranium(VI) by niobate/titanate nanoflakes heterojunction through combined adsorption and solar-light-driven photocatalytic reduction. Appl. Catal. B-Environ. 231, 11–12.

Lyu, H., Tang, J., Huang, Y., Gai, L., Zeng, E.Y., Liber, K., Gong, Y., 2017. Removal of hexavalent chromium from aqueous solutions by a novel biochar supported nanoscale iron sulfide composite. Chem. Eng. J. 322, 516–524.

Ma, J., Li, F., Qian, T., Liu, H., Liu, W., Zhao, D., 2017. Natural organic matter resistant powder activated charcoal supported titanate nanotubes for adsorption of Pb(II). Chem. Eng. J. 315, 191–200.

Ma, R., Yin, L., Li, L., Zhang, S., Wen, T., Zhang, C., Wang, Xiangxue, Chen, Z., Hayat, T., Wang, Xiangke, 2018. Comparative Investigation of Fe_2O_3 and $Fe_{1-x}S$ Nanostructures for Uranium Decontamination . ACS Appl. Nano Mater. 1, 5543–5552.

Meng, H., Hou, W., Xu, X., Xu, J., Zhang, X., 2014. TiO_2-loaded activated carbon fiber: Hydrothermal synthesis, adsorption properties and photo catalytic activity under visible light irradiation. Particuology 14, 38–43.

Mesquita, A.M., Guimarães, I.R., Castro, G.M.M. d., Gonçalves, M.A., Ramalho, T.C., Guerreiro, M.C., 2016. Boron as a promoter in the goethite (α-FeOOH) phase: Organic compound degradation by Fenton reaction. Appl. Catal. B Environ. 192, 286–295.

Moser, D.P., Fredrickson, J.K., Geist, D.R., Arntzen, E.V., Peacock, A.D., Li, S.M.W., Spadoni, T. and McKinley, J.P., 2003. Biogeochemical processes and microbial characteristics across groundwater-surface water boundaries of the Hanford Reach of the Columbia River. Environ. Sci. Technol. 37, 5127–5134.

Mullet, M., Boursiquot, S., Abdelmoula, M., Génin, J.M., Ehrhardt, J.J., 2002. Surface chemistry and structural properties of mackinawite prepared by reaction of sulfide ions with metallic iron. Geochim. Cosmochim. Acta. 66, 829–836.

Namasivayam, C., Kavitha, D., 2006. IR, XRD and SEM studies on the mechanism of adsorption of dyes and phenols by coir pith carbon from aqueous phase. Microchem. J. 82, 43–48.

Nguyen, H.D., Cao, B., Mishra, B., Boyanov, M.I., Kemner, K.M., Fredrickson, J.K., Beyenal, H., 2012. Microscale geochemical gradients in Hanford 300 Area sediment biofilms and influence of uranium. Water Res. 46, 227–234.

Nolan, J. and Weber, K.A., 2015. Natural uranium contamination in major US aquifers linked to nitrate. Environ. Sci. Technol. Lett. 2, 215–220.

Noubactep, C., Meinrath, G., Dietrich, P., Merkel, B., 2003. Mitigating uranium in groundwater: Prospects and limitations. Environ. Sci. Technol. 37, 4304–4308.

Oliveira, R.N., Mancini, M.C., Oliveira, F.C.S. de, Passos, T.M., Quilty, B., Thiré, R.M. da S.M., McGuinness, G.B., Oliveira, R.N., Mancini, M.C., Oliveira, F.C.S. de, Passos, T.M., Quilty, B., Thiré, R.M. da S.M., McGuinness, G.B., 2016. FTIR analysis and quantification of phenols and flavonoids of five commercially available plants extracts used in wound healing. Matéria (Rio Janeiro). 21, 767–779.

Park, S.J., Jang, Y.S., 2003. Preparation and characterization of activated carbon fibers supported with silver metal for antibacterial behavior. J. Colloid Interface Sci. 261, 238–243.

Parkman, R.H., Charnock, J.M., Bryan, N.D., Livens, F.R., Vaughan, D.J., 1999. Reactions of copper and cadmium ions in aqueous solution with goethite, lepidocrocite, mackinawite, and pyrite. Am. Mineral. 84, 407–419.

Pearson, R.G., 1988. Absolute electronegativity and hardness: Application to inorganic chemistry. Inorg. Chem. 27, 734–740.

Plathe, K.L., Lee, S.W., Tebo, B.M., Bargar, J.R. and Bernier-Latmani, R., 2013. Impact of microbial Mn oxidation on the remobilization of bioreduced U(IV). Environ. Sci. Technol. 47, 3606–3613.

Popescu, I.C., Filip, P., Humelnicu, D., Humelnicu, I., Scott, T.B., Crane, R.A., 2013. Removal of uranium(VI) from aqueous systems by nanoscale zero-valent iron particles suspended in carboxy-methyl cellulose. J. Nucl. Mater. 443, 250–255.

Qafoku, N.P., Zachara, J.M., Liu, C., Gassman, P.L., Qafoku, O.S. and Smith, S.C., 2005. Kinetic desorption and sorption of U (VI) during reactive transport in a contaminated Hanford sediment. Environ. Sci. Technol. 39, 3157–3165.

Riley, R.G. and Zachara, J.M., 1992. Chemical contaminants on DOE lands and selection of contaminant mixtures for subsurface science research (No. DOE/ER-0547T). Pacific Northwest Lab., Richland, WA (United States).

Sahasrabudhe, A., Kamble, V.S., Tripathi, A.K., Gupta, N.M., 2001. FTIR Study on Molecular Motions of Benzene Adsorbed in ZSM-5 Zeolite: Role of Charge-Balancing Cations and Pore Size. J. Phys. Chem. B. 105, 4374-4379.

Sarakha, M., Bolte, M., Burrows, H.D., 2000. Electron-transfer oxidation of chlorophenols by uranyl ion excited state in aqueous solution. Steady-state and Nanosecond flash photolysis studies. J. Phys. Chem. A 104, 3142–3149.

Scott, T.B., Allen, G.C., Heard, P.J., Randell, M.G., 2005. Reduction of U(VI) to U(IV) on the surface of magnetite. Geochim. Cosmochim. Acta. 69(24), 5639–5646.

Scott, T.B., Tort, O.R., Allen, G.C., 2007. Aqueous uptake of uranium onto pyrite surfaces; reactivity of fresh versus weathered material. Geochim. Cosmochim. Acta. 71(21), 5044–5053.

Shao, D., Ren, X., Wen, J., Hu, S., Xiong, J., Jiang, T., Wang, Xiaolin, Wang, Xiangke, 2016. Immobilization of uranium by biomaterial stabilized FeS nanoparticles: Effects of stabilizer and enrichment mechanism. J. Hazard. Mater. 302, 1–9.

Shao, D., Wang, X., Li, J., Huang, Y., Ren, X., Hou, G., Wang, X., 2015. Reductive immobilization of uranium by PAAM–FeS/Fe_3O_4 magnetic composites. Environ. Sci.: Water Res. Tech. 1, 169–176.

Shukla, P.R., Wang, S., Sun, H., Ang, H.M., Tadé, M., 2010. Activated carbon supported cobalt catalysts for advanced oxidation of organic contaminants in aqueous solution. Appl. Catal. B Environ. 100, 529–534.

Song, S., Su, Y., Adeleye, A.S., Zhang, Y., Zhou, X., 2017. Optimal design and characterization of sulfide-modified nanoscale zerovalent iron for diclofenac removal. Appl. Catal. B-Environ., 201, 211–220.

Spycher, N.F., Issarangkun, M., Stewart, B.D., Sevinç Şengör, S., Belding, E., Ginn, T.R., Peyton, B.M., Sani, R.K., 2011. Biogenic uraninite precipitation and its reoxidation by iron(III) (hydr)oxides: A reaction modeling approach. Geochim. Cosmochim. Acta. 75, 4426–4440.

Su, Y., Adeleye, A.S., Keller, A.A., Huang, Y., Dai, C., Zhou, X., Zhang, Y., 2015. Magnetic sulfide-modified nanoscale zerovalent iron (S-nZVI) for dissolved metal ion removal. Water Res. 74, 47–57.

Sun, Y., Wu, Z.Y., Wang, Xiangxue, Ding, C., Cheng, W., Yu, S.H., Wang, Xiangke, 2016. Macroscopic and Microscopic Investigation of U(VI) and Eu(III) Adsorption on Carbonaceous Nanofibers. Environ. Sci. Technol. 50, 4459–4467.

Tan, L., Wang, Xiangxue, Tan, X., Mei, H., Chen, C., Hayat, T., Alsaedi, A., Wen, T., Lu, S., Wang, Xiangke, 2017. Bonding properties of humic acid with attapulgite and its influence on U(VI) sorption. Chem. Geol. 464, 91–100.

Thomas, J.E., Jones, C.F., Skinner, W.M., Smart, R.S.C., 1998. The role of surface sulfur species in the inhibition of pyrrhotite dissolution in acid conditions. Geochim. Cosmochim. Acta. 62(9), 1555–1565.

Tratnyek, P.G., Salter-Blanc, A.J., Nurmi, J.T., Amonette, J.E., Liu, J., Wang, C., Dohnalkova, A., Baer, D.R., 2011. Reactivity of zerovalent metals in aquatic media: Effects of organic surface coatings, in: ACS Symposium Series. American Chemical Society, pp. 381–406.

UNSC, 1993. United Nations Scientific Committee on the effects of atomic radiation. Sources and effects of ionizing radiation: Report to the general assembly with scientific annexes. United Nations. ISBN 92-1-142200-0.

Valdivieso, F., Pijolat, M., Soustelle, M., Jourde, J., 2001. Reduction of uranium oxide U3O8 into uranium dioxide UO_2 by ammonia. Solid State Ion., 141, 117–122.

Veeramani, H., Alessi, D.S., Suvorova, E.I., Lezama-Pacheco, J.S., Stubbs, J.E., Sharp, J.O., Dippon, U., Kappler, A., Bargar, J.R., Bernier-Latmani, R., 2011. Products of abiotic U(VI) reduction by biogenic magnetite and vivianite. Geochim. Cosmochim. Acta. 75, 2512–2528.

Veeramani, H., Scheinost, A.C., Monsegue, N., Qafoku, N.P., Kukkadapu, R., Newville, M., Lanzirotti, A., Pruden, A., Murayama, M., Hochella, M.F., 2013. Abiotic reductive immobilization of U(VI) by biogenic mackinawite. Environ. Sci. Technol. 47, 2361–2369.

Wang, Q., Lei, X., Pan, F., Xia, D., Shang, Y., Sun, W., Liu, W., 2018. A new type of activated carbon fibre supported titanate nanotubes for high-capacity adsorption and degradation of methylene blue. Colloids Surfaces A Physicochem. Eng. Asp. 555, 605–614.

Wang, Y., Liu, W., Wang, T., Ni, J., 2015. Arsenate adsorption onto Fe-TNTs prepared by a novel water-ethanol hydrothermal method: Mechanism and synergistic effect. J. Colloid Interface Sci. 440, 253–262.

Wei, C., Tang, Y., Zhang, G., Zhang, Q., Zhan, X., Chen, F., 2016. Facile fabrication of highly omniphobic and self-cleaning surfaces based on water mediated fluorinated nanosilica aggregation. RSC Adv. 6, 74340–74348.

Widler, A.M., Seward, T.M., 2002. The adsorption of gold(I) hydrosulphide complexes by iron sulphide surfaces. Geochim. Cosmochim. Acta. 66, 383–402.

Wolthers, M., Van der Gaast, S.J., Rickard, D., 2003. The structure of disordered mackinawite. Am. Mineral. 88, 2007–2015.

Xie, L., Shang, C., 2007. The effects of operational parameters and common anions on the reactivity of zero-valent iron in bromate reduction. Chemosphere, 66(9), 1652–1659.

Xing, M., Xu, L., Wang, J., 2016. Mechanism of Co(II) adsorption by zero valent iron/graphene nanocomposite. J. Hazard. Mater. 301, 286–296.

Xiong, Z., Zhao, D., Pan, G., 2009. Rapid and controlled transformation of nitrate in water and brine by stabilized iron nanoparticles. J. Nanopart. Res. 11, 807–819.

Xu, Y., Schoonen, M.A., 2000. The absolute energy positions of conduction and valence bands of selected semiconducting minerals. Am. Mineral. 85, 543–556.

Yan, S., Hua, B., Bao, Z., Yang, J., Liu, C., Deng, B., 2010. Uranium(VI) removal by nanoscale zerovalent iron in anoxic batch systems. Environ. Sci. Technol. 44, 7783–7789.

Yang, Y., Liu, Y., Li, Y., Gao, M., Pan, H., 2015. Fluorine-substituted $Mg(BH_4)_2 \cdot 2NH_3$ with improved dehydrogenation properties for hydrogen storage. J. Mater. Chem. A. 3, 570–578.

Yazdani, M.R., Duimovich, N., Tiraferri, A., Laurell, P., Borghei, M., Zimmerman, J.B., Vahala, R., 2019. Tailored mesoporous biochar sorbents from pinecone biomass for the adsorption of natural organic matter from lake water. J. Mol. Liq. 291, 111248.

Ylhäinen, E.K., Nunes, M.R., Silvestre, A.J., Monteiro, O.C., 2012. Synthesis of titanate nanostructures using amorphous precursor material and their adsorption/photocatalytic properties. J. Mater. Sci. 47, 4305–4312.

Zhao, D., Pignatello, J.J., White, J.C., Braida, W., Fcrrandino, F., 2001. Dual-mode modeling of competitive and concentration-dependent sorption and desorption kinetics of polycyclic aromatic hydrocarbons in soils, Water Resour Res. 37, 2205–2212.

Zhao, X., Liu, W., Cai, Z., Han, B., Qian, T., Zhao, D., 2016. An overview of preparation and applications of stabilized zero-valent iron nanoparticles for soil and groundwater remediation. Water Res. 100, 245–266.

Zhu, W., Li, Y., Dai, L., Li, J., Li, X., Li, W., Duan, T., Lei, J. and Chen, T., 2018. Bioassembly of fungal hyphae/carbon nanotubes composite as a versatile adsorbent for water pollution control. Chem. Eng. J. 339, 214–222.

Zogorski, J.S., Faust, S.D., Haas, J.H., 1976. The kinetics of adsorption of phenols by granular activated carbon. J. Colloid Interface Sci. 55, 329–341.